

WISSENSCHAFTLICH-TECHNISCHE BERICHTE

**FZR-331**

September 2001

ISSN 1437-322X

**Archiv-Ex.:**

*Stefano Parascandola*

**Nitrogen transport during ion nitriding of  
austenitic stainless steel**

Herausgeber:  
Forschungszentrum Rossendorf e.V.  
Postfach 51 01 19  
D-01314 Dresden  
Telefon +49 351 26 00  
Telefax +49 351 2 69 04 61  
<http://www.fz-rossendorf.de/>

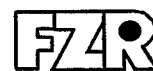
Als Manuskript gedruckt  
Alle Rechte beim Herausgeber

FORSCHUNGSZENTRUM ROSSENDORF

WISSENSCHAFTLICH-TECHNISCHE BERICHTE

**FZR-331**

September 2001



*Stefano Parascandola*

**Nitrogen transport during ion nitriding of  
austenitic stainless steel**

**Dissertation**

# Nitrogen transport during ion nitriding of austenitic stainless steel

## Dissertation

zur Erlangung des akademischen Grades  
Doctor rerum naturalium  
(Dr. rer. nat.)

vorgelegt

der Fakultät Mathematik und Naturwissenschaften  
der Technischen Universität Dresden

von

Dipl.-Phys. STEFANO PARASCANDOLA  
geboren am 27. April 1967 in Lengerich

November 2000

# Contents

<b>1</b>	<b>Introduction</b>	<b>1</b>
<b>2</b>	<b>Fundamentals</b>	<b>5</b>
2.1	Basic considerations on transport . . . . .	5
2.2	Ion-solid interaction . . . . .	7
2.2.1	Basic mechanisms . . . . .	7
2.2.2	Computer simulation programs . . . . .	8
2.3	Diffusion . . . . .	12
2.3.1	"Simple" diffusion . . . . .	12
2.3.2	Trapping . . . . .	13
2.4	Approaches to transport modeling . . . . .	16
2.4.1	The time and depth dependent concentration . . . . .	16
2.4.2	The retention rate . . . . .	16
2.4.3	The evolution of the layer thickness . . . . .	17
<b>3</b>	<b>Material and experimental methods</b>	<b>21</b>
3.1	Material . . . . .	21
3.2	Material modification . . . . .	23
3.2.1	The ion source . . . . .	23
3.2.2	The vacuum system . . . . .	24
3.2.3	The sample mount . . . . .	25
3.2.4	Processing, process control, and coupling to physical parameters . . . . .	25
3.3	Material analysis . . . . .	27
3.3.1	A brief introduction to ion beam analysis . . . . .	27
3.3.2	Elastic recoil detection analysis . . . . .	28
3.3.3	Real-time elastic recoil detection analysis . . . . .	31
3.3.4	Nuclear reaction analysis . . . . .	34
<b>4</b>	<b>Results and discussion</b>	<b>37</b>
4.1	The structural nature of the nitrogen enriched layer . . . . .	37
4.1.1	Introduction . . . . .	37
4.1.2	Experimental results . . . . .	38
4.1.3	Discussion . . . . .	42
4.1.4	Summary . . . . .	44

4.2	The diffusion mechanism of nitrogen . . . . .	46
4.2.1	Introduction . . . . .	46
4.2.2	Experimental results . . . . .	46
4.2.3	Modeling results . . . . .	50
4.2.4	Discussion . . . . .	51
4.2.5	Summary . . . . .	52
4.3	The role of potential incorporation and release mechanisms . . . . .	54
4.3.1	Introduction . . . . .	54
4.3.2	Experimental results . . . . .	54
4.3.3	Modeling results . . . . .	57
4.3.4	Discussion . . . . .	61
4.3.5	Summary . . . . .	62
4.4	The evolution of the thickness of the nitrogen enriched layer . . . . .	63
4.4.1	Introduction . . . . .	63
4.4.2	Experimental results . . . . .	63
4.4.3	Modeling results . . . . .	63
4.4.4	Discussion . . . . .	65
4.4.5	Summary . . . . .	66
4.5	The role of the surface oxide layer . . . . .	67
4.5.1	Introduction . . . . .	67
4.5.2	Basic considerations on oxide removal and oxide growth . . . . .	67
4.5.3	Experimental results . . . . .	69
4.5.4	Modeling results . . . . .	76
4.5.5	Discussion . . . . .	78
4.5.6	Summary . . . . .	78
<b>5</b>	<b>Summary</b>	<b>81</b>
<b>A</b>	<b>Consequences of an oscillating ion energy</b>	<b>85</b>
	<b>List of Figures</b>	<b>88</b>
	<b>List of Tables</b>	<b>90</b>
	<b>Bibliography</b>	<b>91</b>
	<b>Acknowledgements / Danksagung</b>	<b>107</b>

# Chapter 1

## Introduction

### Ion Nitriding

As an excerpt from the definitions given by the American Society for Metals [1] and the DIN Deutsches Institut für Normung e.V. [2] nitriding may be defined as a heat treatment involving diffusion, whereby nitrogen is introduced through the surface into the surface area of a solid substrate. The goal of nitriding is to improve material properties as, for example, surface hardness, wear resistance, and corrosion resistance. Correlative to the medium from which nitrogen is supplied to the solid substrate the terms gas nitriding, liquid nitriding and plasma nitriding are widely spread [1, 2, 3, 4, 5, 6]. Consequently, the term ion nitriding as it is used in this work, is intended to emphasize that nitrogen is mainly supplied to the substrate by nitrogen ions. With this definition, ion nitriding is not necessarily a synonym for plasma nitriding which is sometimes called ion nitriding as well [7, 8, 9, 10, 11, 12]. However, plasma nitriding has features of ion nitriding and vice versa and synergies may be expected by systematical investigations of either of the processes.

### Austenitic stainless steel

Stainless steel is a generic term covering a large group of polycrystalline iron-based alloys that are commonly known for their corrosion resistance [13, 14, 15, 16, 17, 18]. Their quota of the world's total annual steel production is about 15%. Their main alloying elements are chromium and nickel positioned in random solid solution with iron atoms on substitutional sites within each grain. The chromium content of stainless steels normally exceeds 12 wt.%, resulting in the formation of a surface oxide layer that protects the metal matrix from corrosion. The microstructure and properties depend on the composition and the heat treatment. Three major classes that represent distinct types of alloy microstructure can be distinguished. These major classes are austenitic, ferritic, and martensitic stainless steels corresponding to face-centered-cubic, body-centered-cubic, and tetragonal crystal lattice structure, respectively. Owing to a particular good combination of material properties as, for example, corrosion resistance, ductility, strength, and weldability, the austenitic class is the most popular one. The hardness of austenitic stainless steels, however, is fairly low making them inappropriate for wear intensive applications.

### Technological relevance, obstacles, and current status

From their combination of properties and their economical prominence originates the demand for successful surface hardening of austenitic stainless steel. While mere heat treatment processes as induction hardening or flame hardening fail, nitriding is a potential method. It is known from ion implantation [19, 20, 21, 22, 23, 24] and nitrogen alloying [25, 26, 27, 28, 29, 30] that nitrogen may have diverse beneficial effects, among them improving hardness, strength, and corrosion properties.

However, stainless steels are known as difficult candidates for successful nitriding, that is, nitriding resulting in a significant increase of the surface hardness without severely impairing the corrosion properties. Their surface oxide layer is supposed to be a barrier for nitrogen diffusion. Additionally, at typical nitriding temperatures above 500°C, austenitic stainless steels lose their stainless character due to the formation of chromium nitride precipitates and the corresponding depletion of chromium from the metal matrix.

Nonetheless, by now it is established that austenitic stainless steels can be nitrided successfully. At moderate nitriding temperature around 400°C, distinct techniques as, for example, low energy ion implantation, plasma nitriding by means of a conventional glow-discharge, and remote plasma nitriding techniques, that is, techniques uncoupling the generation of a plasma from the substrate as, for example, plasma immersion ion implantation, have been employed successfully [31, 32, 33, 34, 35, 36, 37, 38, 39, 40, 41, 42, 43, 44, 45, 46, 47, 48, 49, 50, 51, 52, 53, 54, 55, 56, 57, 58, 59, 60, 61, 62, 63, 64, 65, 66, 67, 68, 69, 70, 71, 72]. All these techniques have a common feature: They employ energetic nitrogen ions. From a technological point of view, besides economical aspects, the key question is [73]: Is there is a clear advantage of a particular technique or set of processing conditions? The answer to this question is related to the understanding of the induced surface modification. Neither the nitrogen transport nor the structural formation during successful nitriding of austenitic stainless steels is well understood. In particular the lack of understanding of transport phenomena leads to limited reproducibility when successful nitriding of austenitic stainless steel is tried to be performed on an industrial scale<sup>1</sup>.

### Purpose, methods, and outline

The purpose of this work is to improve the understanding of the surface modification induced on austenitic stainless steel during nitriding by techniques that employ energetic nitrogen ions. The focus is on the identification and characterization of transport mechanisms relevant for ion nitriding. Special emphasis is given to the role of the surface oxide layer.

Ion nitriding by low energy ion implantation has been chosen for material modification and has been set up such that the modification process is unequivocally described by a reasonable number of relevant processing parameters. Additionally, the relevant processing parameters are closely coupled to physical parameters and can be varied independently. With these features the premise for a feasible description of the material modification in

---

<sup>1</sup>A reliable reference is difficult since any company offering surface treatment is obviously unwilling to admit that a process does not work satisfactorily.



---

terms of physics is fulfilled. In order to gain experimental data, ion nitrided samples have been analyzed by x-ray diffraction, slow positron implantation spectroscopy, glow discharge optical emission spectroscopy, and the ion beam analysis techniques elastic recoil detection analysis and nuclear reaction analysis. An experiment has been set up that combines ion nitriding by low energy ion implantation with elastic recoil detection analysis. This combined experiment allows for real-time measuring of absolute concentration depth profiles of carbon, nitrogen, and oxygen during the modification process. Thus, it already meets two out of four research needs on process control and material inspection instrumentation identified in the American Society for Metals Heat Treating Technology Roadmap towards its Vision 2020 [74], that is, direct real-time method of measuring carbon (nitrogen) in the heat treated part and sensor to determine whether a part's surface is clean enough to be correctly carburized (nitrided). Furthermore, transport models that allow for quantitative predictions are resumed and refined. Modeling results are compared to experimental data in order in order to characterize relevant transport mechanisms.

The work is structured as follows: In Chapter 2 fundamental transport concepts and phenomena and approaches to transport modeling are introduced. In Chapter 3 details are presented concerning the material under investigation, the material modification process, and the ion beam analytical techniques. In Chapter 4 experimental and modeling results are presented and discussed. Issues that are directly addressed include:

- The structural nature of the nitrogen enriched layer.
- The diffusion mechanism of nitrogen.
- The role of potential incorporation and release mechanisms.
- The evolution of the thickness of the nitrogen enriched layer.
- The role of the surface oxide layer.

Chapter 5 provides a summary.

# Chapter 2

## Fundamentals

### 2.1 Basic considerations on transport

#### Premises and important measures

In ion nitriding, by its definition, nitrogen gets incorporated into the substrate by ion implantation. The system becomes unstable in terms of thermodynamics. New phases may form and a nitrogen enriched layer, with a thickness that can easily exceed the typical implantation depth by orders of magnitude, results from diffusional transport<sup>1</sup>. In this work, the incident nitrogen ion beam can be considered as homogenous over the lateral extension of the substrate. The substrate itself can be considered as flat and its lateral extension as large compared to the modification depth. Grain boundary diffusion<sup>2</sup> as well as lateral inhomogenities<sup>3</sup> are neglected. Thus, the nitrogen transport can be described one-dimensionally, for example, in terms of one-dimensional bulk diffusion in a semi-infinite solid in connection with a source term that represents the flux or, more rigorously, the flux density of implanted nitrogen.

The most important transport measure is the time and depth dependent nitrogen concentration  $N(x, t)$ . Related transport measures are the rate with which nitrogen is retained in the substrate  $j_{\text{ret}}(t)$ , and the amount of retained nitrogen  $N_{\text{ret}}(t)$ . The compositional and structural changes that are induced in the substrate may also be influenced by gas-solid interaction, for example, in case a surface oxide forms on the solid surface due to oxidation from the residual gas. Thus, measures as above, but referring to oxygen, are other important transport measures.

---

<sup>1</sup>The typical implantation depth is in the order of a few nanometers while the thickness of the nitrogen enriched layer may easily exceed a micrometer.

<sup>2</sup>Grain boundary diffusion can be neglected for spatial considerations and since the high nitrogen concentrations are observed within grains and not preferentially near grain boundaries.

<sup>3</sup>Lateral inhomogenities, more precisely a thickness of the nitrogen enriched layer that depends on the grain orientations, are sometimes observed by others [75, 67]. These observation will be considered to a certain extent where experimental and modeling results are discussed.

### Classification in the context of plasma nitriding

The techniques that have been employed successfully for nitriding of austenitic stainless steel have the common feature that they involve nitrogen ions with kinetic energies that significantly exceed thermal energies. Thus, it is evident that the description of transport is not limited to equilibrium thermodynamics. Concepts from ion/plasma physics and the interaction of ions/plasma with the gas phase and the solid phase are of potential relevance as well. As indicated in Figure 2.1, a complicated network of interdependencies will have to be considered if the solid surface is directly exposed to a plasma (as, for example, in plasma nitriding by means of a conventional glow-discharge or in plasma immersion ion implantation). During ion nitriding by means of low energy ion implantation the

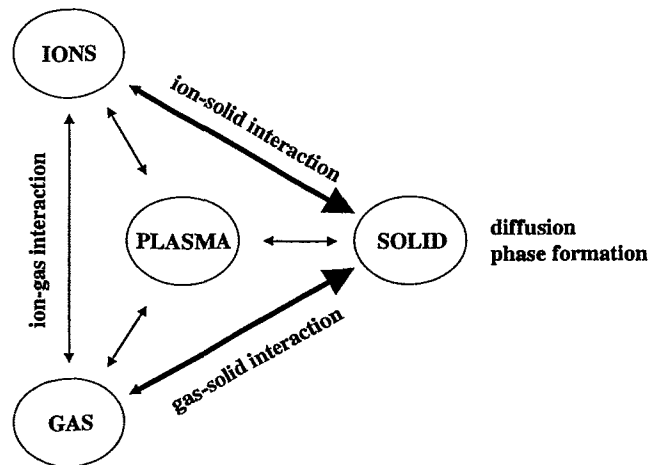


**Figure 2.1:** Media (UPPER CASE) and fields of physics (lower case) involved in plasma nitriding. Not explicitly mentioned are the interactions of the plasma with the neighboring media.

solid surface is *not* directly exposed to a plasma. No interaction of the plasma with the surrounding media has to be considered. Normally, ion-gas interaction can be neglected as well. Owing to the facts that (i) the solid phase is usually not in thermal equilibrium with the gas phase and that (ii) austenitic stainless steel itself is already a metastable material (usually austenitic stainless steel gets quenched from temperatures around 1100°C in order to retain the austenitic phase [14]), concepts from **ion-solid interaction** and **diffusion** do receive more attention in this work than concepts from phase formation and gas-solid interaction. For other materials or nitriding setups it will be interesting to consider the latter concepts as well as aspects of plasma interactions in greater detail. The interested reader is referred, for example, to Refs. [76, 77, 78, 79, 80, 81, 82, 83, 84, 85, 86, 87, 88, 89] and references therein.

## 2.2 Ion-solid interaction

### 2.2.1 Basic mechanisms

Energetic ions impinging on a solid substrate may either be **reflected**, or **implanted**, that is, slowed down to thermal velocities within the substrate. Additionally, they may **displace** substrate atoms from their original lattice sites and **remove** atoms from the substrate. These four mechanisms are of potential relevance for the understanding of the nitrogen transport during ion nitriding.

A qualitative understanding of the above mechanisms can be attained by a purely collisional argumentation considering the interaction of an ion with the sample nuclei. In an amorphous solid this interaction can be described in terms of a series of independent elastic binary collisions between the ion and the substrate atoms<sup>4</sup>. In every collision the ion transfers energy and momentum to a substrate atom and changes its flight path. The resulting stochastic polygonal trajectory of the ion may end inside the solid or it may cross the substrate surface before the ion is slowed down to thermal velocities. Respectively, the ion may either be implanted or reflected. The energy transferred from the ion to the substrate atoms can be sufficient to displace the atoms from their original lattice sites and the displaced atoms themselves can have enough energy to displace other substrate atoms resulting in a collision cascade. If an atom that is located close to the surface experiences a momentum transfer with a momentum component directed towards the surface it may be removed from the substrate. The latter mechanism is usually called physical sputtering or simply sputtering.

For a quantitative description the elastic binary collisions can be described in terms of classical scattering of a charged particle at an effective screened Coulomb-Potential<sup>5</sup>. Cross sections and kinematics of the scattering events are well known. Additional to the interaction of the ion with the substrate nuclei the interaction of the ion with the substrate electrons has to be considered. The latter does not lead to significant changes in the flight path, but contributes to the slowing down of the ion. Analytical results, applying for different energy and mass regimes, exist for the amount of energy lost due to either interactions with the nuclei [91] or electrons [92, 93, 94]. Usually, these results enter into analytical expressions that have been shown to be applicable for a quantitative description of the above four mechanisms [95, 96, 97, 98]. Thus, in principle, analytical expressions for a quantitative description of reflection, implantation, displacements, and sputtering are available. Their applicability, however, often suffers from a complicated structure and a restricted range of validity with respect to the ion-substrate combinations and the energy regime.

---

<sup>4</sup>valid for ion energies above  $\approx 100$  eV [90].

<sup>5</sup>valid for ion energies insufficient to overcome the repulsive Coulomb barrier of the nuclei, that is, ion energies below  $\approx 1$  MeV.

## 2.2.2 Computer simulation programs

For practical purposes it is often more adequate to use computer simulation programs as, for example, SRIM [91, 99], PROFILE [100], TRIMCSR [101, 102], and TRIDYN [103, 104, 105]. In this work, SRIM and TRIDYN are extensively applied to estimate backscattering yields, sputtering yields, and projected ranges.

In both programs, SRIM and TRIDYN, the incoming ions are characterized by their mass, their atomic number, their kinetic energy, and their angle of incidence. The substrate is characterized by its composition, its density<sup>6</sup>, and the binding energies of the target atoms, namely the displacement energy  $E_d$ , the surface binding energy  $E_s$ , and the lattice or bulk binding energy  $E_b$ .  $E_d$  is the energy that a target atom needs to overcome the lattice forces and to form a stable Frenkel pair.  $E_s$  is the energy that a target atom must overcome to leave the surface of the target.  $E_b$  is the energy that every substrate atom loses when it leaves its lattice site and collides with other substrate atoms.

The surface binding energy is a key parameter for sputtering, which plays an important role in ion nitriding. For most elemental substrates SRIM and TRIDYN provide reasonable values of  $E_s$  as defaults. Alternatively, the heat of sublimation is a good estimate for this energy. For multicomponent targets the choice of the surface binding energy is more complicated. Reasonable values can be obtained by considering that the sum of the surface binding energies must be consistent with the thermodynamic balance. For a two component metal-gas compound  $A_mB_n$ , where  $B$  is the gaseous element, it follows [105] that

$$mE_s(A) + nE_s(B) = m\Delta H_s(A) + \frac{1}{2n}\Delta H_m(B) + \Delta H_f(A_mB_n), \quad (2.1)$$

where  $\Delta H_s(A)$  denotes the sublimation enthalpy of  $A$ ,  $\Delta H_m(B)$  the molecular binding energy of  $B$ , and  $\Delta H_f(A_mB_n)$  the compound formation enthalpy of  $A_mB_n$ . Taking  $E_s(A) = \Delta H_s(A)$  for the pure metal,  $E_s(B)$  can be easily calculated.

### SRIM

Figure 2.2 shows selected results of SRIM simulations for nitrogen ions impinging perpendicular on an iron substrate<sup>7</sup> with a density of 7.98 g/cm<sup>3</sup>. The nitrogen depth profile resulting for atomic nitrogen ions with a kinetic energy  $E_{in} = 1$  keV is shown in Figure 2.2a (normalized with respect to the ion fluence). The nitrogen depth profile is gaussian-like, which is generally the case for small fluences of monoenergetic ions. Fluctuations of the nitrogen concentration versus depth are due to the statistical nature of the simulation. The mean value of the nitrogen depth distribution is called the mean projected range  $\overline{R_p}$ . Here,  $\overline{R_p}$  amounts to 2.4 nm. In the energy range of direct interest in this work ( $E_{in} = 0.2-2$  keV)  $\overline{R_p}$  shows an approximately linear dependence of the incident ion energy (Figure 2.2b). The amount of backscattered ions and atoms removed from the substrate surface are expressed

<sup>6</sup>Throughout this work a density assumption has been made in simulating ion-solid interaction as well as in evaluating ion beam analysis data. This has been done in order to arrive at the more descriptive technical unit of nm instead of at./cm<sup>2</sup>.

<sup>7</sup>For the present purpose such a substrate is a good approximation for most austenitic stainless steels.

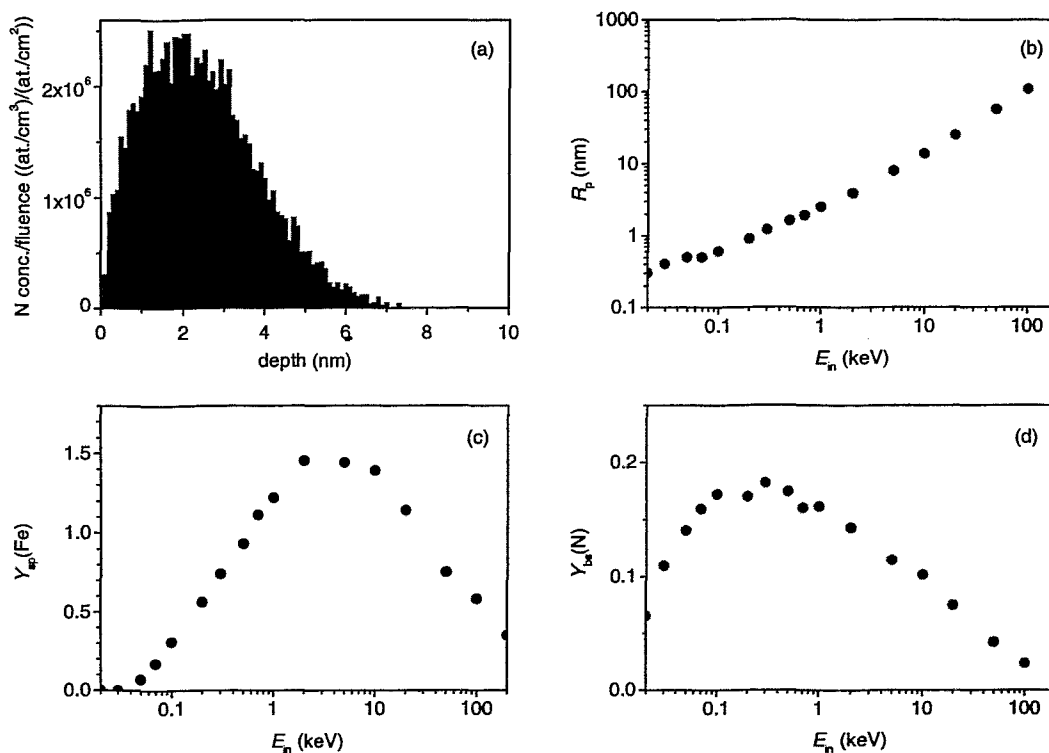


**Figure 2.2:** Selected results of SRIM simulations for atomic nitrogen ions implanted into iron (density  $7.98 \text{ g/cm}^3$  and default values for the binding energies, that is,  $E_d = 25 \text{ eV}$ ,  $E_s = 4.34 \text{ eV}$ ,  $E_b = 3 \text{ eV}$ ). (a) nitrogen depth profile normalized with respect to the ion fluence resulting for  $E_{in} = 1 \text{ keV}$ , (b) mean projected range versus ion energy, (c) sputtering yield of iron versus ion energy, (d) backscattering yield of nitrogen versus ion energy. 5000 projectiles were calculated for each ion energy.

in terms of a mean number per incident particle<sup>8</sup> as the backscattering yield  $Y_{bs}$  and the sputtering yield  $Y_{sp}$ , respectively [90]. These measures show more complex dependences on the incident ion energy as illustrated in Figures 2.2c and Figure 2.2d. The sputtering yield increases almost linear with the logarithm of  $E_{in}$  from zero at a threshold energy  $E_{in} = E_d$  up to a maximum value around a few keV, from where it decreases. The backscattering yield shows a similar dependence at a lower yield level and shifted to lower energies.

Since SRIM, in contrast to TRIDYN, does not consider any kind of dynamic substrate changes that are induced by the ion bombardment, its applicability is limited to cases where these changes are negligible as, for example, at low ion fluences.

<sup>8</sup>For bombardment with monoatomic molecular ions, each incident atom is generally counted separately [90].

## TRIDYN

TRIDYN considers dynamic substrate changes and it is even possible to employ surface binding energies that depend on the near surface composition:

$$\begin{pmatrix} E_s(A) \\ E_s(B) \end{pmatrix} = \begin{pmatrix} E_{AA} & E_{AB} \\ E_{BA} & E_{BB} \end{pmatrix} \begin{pmatrix} A_{ns} \\ B_{ns} \end{pmatrix}, \quad (2.2)$$

where  $A_{ns}$  and  $B_{ns}$  are the near surface concentrations of element  $A$  and element  $B$ , respectively. Taking again  $E_{AA} = \Delta H_s(A)$  and choosing  $E_{BB} = 0$ , neglecting any chemistry between the gas atoms,  $E_{AB}$  can be calculated [105] according to

$$E_{AB} = \frac{1}{2}\Delta H_s(A) + \frac{m+n}{4n}\Delta H_m(B) + \frac{m+n}{2nm}\Delta H_f(A_mB_n). \quad (2.3)$$

Figure 2.3 shows selected results of a TRIDYN simulation, again for atomic nitrogen ions,  $E_{in} = 1$  keV, impinging perpendicular on an iron substrate with a density of  $7.98 \text{ g/cm}^3$ . Since for an interstitial solid solution of nitrogen (refer to Section 4.1) the compound formation enthalpy is not well known,  $E_{FeFe} = \Delta H_s(Fe) = 4.34 \text{ eV}$ ,  $E_{NN} = 0 \text{ eV}$ , and  $E_{FeN} = E_{NFe} = 1 \text{ eV}$  have been assumed. The latter corresponds roughly to the diffusion activation energy of nitrogen (refer to Section 4.2). Figure 2.3a shows nitrogen depth profiles after selected ion fluences. For high fluences the depth profiles tend towards a stationary state. Such a behavior can be considered as a general feature of material modification by ion implantation if the modification parameters are constant. Close to the surface, the stationary state nitrogen depth profile exhibits a concentration that is much smaller than the maximum nitrogen concentration. This feature indicates that nitrogen is sputtered preferentially [106], that is, the ratio of the partial sputtering yield of nitrogen – defined as the average number of nitrogen atoms removed per incident particle – and the near surface concentration of nitrogen, is higher than the corresponding ratio for iron. In other terms, the ejection probability of nitrogen relative to its near surface concentration is higher than the one of iron. Figure 2.3b shows the amount of retained nitrogen versus the ion fluence, Figure 2.3c the near surface concentration<sup>9</sup> of nitrogen and iron versus the ion fluence, and Figure 2.3d the partial sputtering yield of nitrogen and iron versus the ion fluence. Consistent with the fact that the nitrogen depth profile tends towards a stationary state, in all cases the respective measures tend towards a stationary value. As expected for preferential sputtering of nitrogen, the ratio of the stationary partial sputtering yield of nitrogen and the stationary near surface concentration of nitrogen is much higher than the respective ratio for iron.

<sup>9</sup>Here the near surface concentration has been chosen as the mean concentration in the first 0.5 nm corresponding to the depth interval from where sputtered atoms originate, that is, the topmost 2 to 3 atomic layers [90].

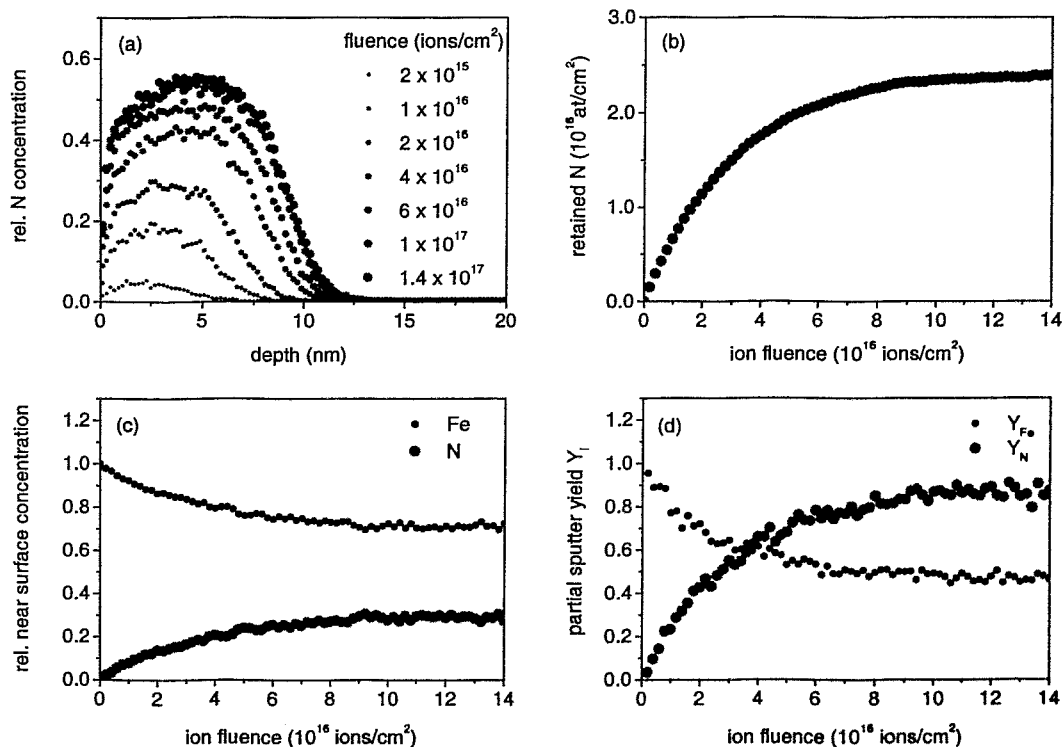


**Figure 2.3:** Selected results of a TRIDYN simulation for atomic nitrogen ions,  $E_{in} = 1$  keV, implanted into iron (density  $7.98$  g/cm<sup>3</sup>). (a) nitrogen depth profiles after selected ion fluences, (b) amount of retained nitrogen vs. ion fluence, (c) near surface concentration of nitrogen and iron vs. ion fluence, (d) partial sputtering yield of nitrogen and iron vs. ion fluence. Surface binding energies of nitrogen ( $E_s(N)$ ) and iron ( $E_s(Fe)$ ) depending on the near surface composition have been employed.



## 2.3 Diffusion

Diffusion can be described by a generalized form of Fick's law<sup>10</sup> [107]

$$j_i(x) = -c_i(x) m_i(x) \frac{d}{dx} G_i(x), \quad (2.4)$$

where  $j_i$  denotes the diffusion flux density in units of atoms/m<sup>2</sup>s,  $c_i$  the concentration in units of atoms/m<sup>3</sup>,  $m_i$  the thermal mobility in units of Nm/s,  $G_i$  the chemical potential of a diffusing element  $i$  in units of Nm, and  $x$  the depth in units of m. Fick's law can only be used in a steady-state regime, that is, when the diffusion flux of element  $i$  at depth  $x$  is independent of time  $t$ .

### 2.3.1 "Simple" diffusion

In ion nitriding one often deals with single-phase substrates with thermal mobilities of substrate atoms that are negligible compared to the thermal mobility of nitrogen. For species that obey a conservation law, Equation 2.4 can be transformed — assuming concentration-independent diffusion — into a second-order partial differential equation often called Fick's second law

$$\frac{\partial}{\partial t} N(x, t) = D \frac{\partial^2}{\partial x^2} N(x, t), \quad (2.5)$$

where  $N(x, t)$  is the time and depth dependent nitrogen concentration and  $D$  is the diffusivity or the diffusion coefficient of nitrogen.  $D$  depends on temperature according to

$$D = D_0 e^{-E_A/kT}, \quad (2.6)$$

where  $D_0$  is the pre-exponential factor of diffusion,  $E_A$  the activation energy,  $k$  the Boltzmann constant, and  $T$  the temperature. In the atomic picture of a diffusion jump  $D_0$  is independent of temperature and can be expressed in terms of the mean jump distance  $\alpha_0$  and the vibration or attempt frequency  $\nu_0$  as  $D_0 = (1/6) \alpha_0^2 \nu_0$ . The term  $e^{-E_A/kT}$  is the probability for a successful attempt and the activation energy  $E_A$  is the height of the potential energy wall that the diffuser has to overcome in a jump event.

Relatively simple analytical solutions of Equation 2.5 are available for a number of different initial and boundary conditions. An idealized case that will be considered in this work is diffusion at constant surface concentration and zero initial concentration ( $N(x, t) = 0$  at  $t = 0$  for  $x > 0$  and  $N(0, t) = \text{constant}$  at  $t > 0$ ). In this case of "simple" diffusion the solution of Equation 2.5 is

$$N(x, t) = N(0, t) \times \left( 1 - \operatorname{erf} \frac{x}{2\sqrt{Dt}} \right), \quad (2.7)$$

where erf is the error function. Figure 2.4 shows depth profiles calculated according to Equation 2.7. The shape of the depth profile is called error functional. It is characteristic

<sup>10</sup>Driving forces other than the gradient in the chemical potential are not considered.

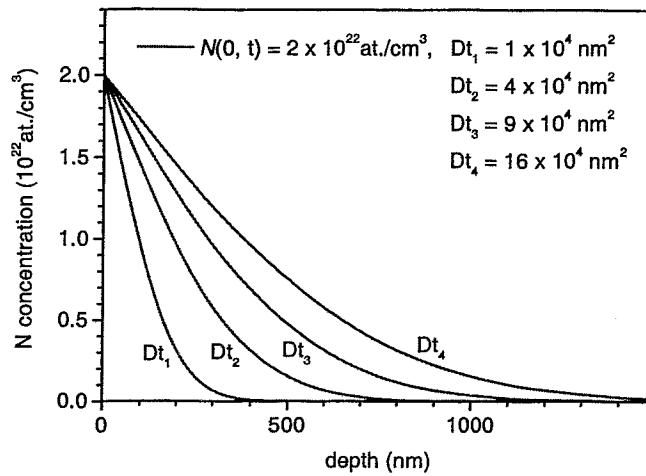


Figure 2.4: A schematic example of the shape of nitrogen depth profiles assuming "simple" nitrogen diffusion.

for "simple" diffusion in a single phase substrate. Other characteristics of "simple" diffusion are (i) the depth at which the concentration remains constant varies with the square root of time and (ii) the amount of the diffuser that is introduced into the substrate per unit area varies with the square root of time [108].

### 2.3.2 Trapping

A mechanism that has not been considered so far, but which is relevant for the diffusional transport in ion nitriding of austenitic stainless steel, is trapping. Trapping is characterized by the fact that the diffusing species exists in different states, that is, it occupies at least two types of lattice sites (compare Figure 2.5). In case of trapping the equation of continuity does apply for the total amount of the diffuser, but not for the amount of the diffuser in either of the different states. Considering nitrogen as a diffuser that can be present either on diffusion sites where it can diffuse or on trap sites where it can not diffuse, Equation 2.5 becomes:

$$\frac{\partial}{\partial t} N(x, t) = \frac{\partial}{\partial t} N_d(x, t) + \frac{\partial}{\partial t} N_t(x, t) = D \frac{\partial^2}{\partial x^2} N_d(x, t), \quad (2.8)$$

where  $N_d(x, t)$  and  $N_t(x, t)$  denote the time and depth dependent concentration of nitrogen on diffusion sites and trap sites, respectively. Assuming further that

- only one type of trap sites exist,
- the concentration of trap sites is constant in time and depth,
- every trap site can only bind one atom,

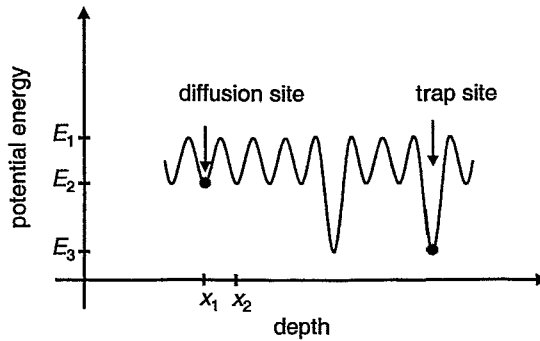


**Figure 2.5:** A schematic diagram enlightening the meaning of a diffusion site and a trap site. Trap sites are sites that expose a higher binding energy than diffusion sites.  $E_1 - E_2$  and  $E_1 - E_3$  are the diffusion activation energy  $E_d$  of nitrogen on diffusion sites and the detrapping activation energy  $E_{t \rightarrow d}$  of nitrogen on trap sites, respectively.  $x_2 - x_1$  is the diffusion jump distance.

- the detrapping energy is independent of the fraction of occupied traps,
- local thermal equilibrium [109] exists between nitrogen on diffusion sites and nitrogen on trap sites,
- trapping and detrapping are diffusion controlled [110] and follow first-order kinetics,

the trap term in Equation 2.8 can be expressed as

$$\frac{\partial}{\partial t} N_t(x, t) = k_{d \rightarrow t} N_d(x, t) \left( 1 - \frac{N_t(x, t)}{H_t(x, t)} \right) - k_{t \rightarrow d} N_t(x, t) \quad (2.9)$$

where  $H_t(x, t)$  denotes the concentration of trap sites in the host matrix,  $k_{d \rightarrow t}$  a rate constant for trapping, that is for the transition of nitrogen from a diffusion site to a trap site, and  $k_{t \rightarrow d}$  a rate constant for detrapping, i.e. for the transition of nitrogen from a trap site to a diffusion site. Thus, in case trapping occurs the diffusion is described by a set of two coupled differential equations (Equation 2.8 and Equation 2.9). Usually, this set of equations cannot be solved analytically. However, assuming again constant surface concentration and zero initial concentration, it can be deduced from analytical considerations [111] that near a total concentration similar to the trap concentration the total depth profile will exhibit a relatively sharp division between an error functional and an exponential dependence if (i) the diffusion sites are well separated in energy from the trap sites and (ii) the surface concentration is much higher than the trap concentration. This feature is illustrated in Figure 2.6. From the surface down to the depth where the concentration is approximately  $H_t(x, t)$  the total depth profile decreases error functional with a concentration offset equal to the trap concentration. Close to the depth where the total concentration equals the trap concentration the shape of the depth profile turns from error functional to a more steeply decreasing exponential.

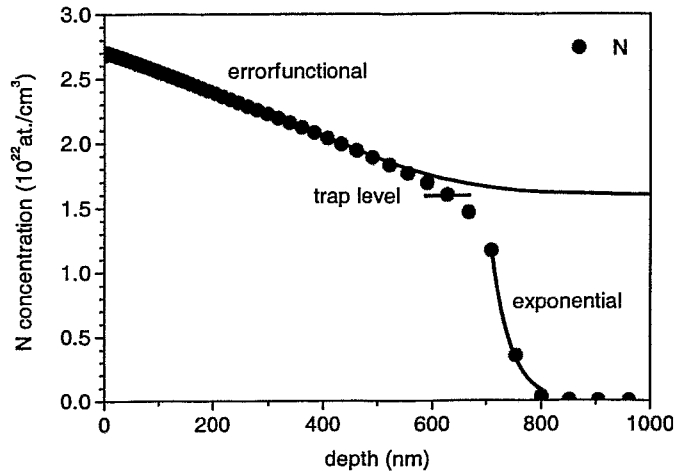


**Figure 2.6:** A schematic example for a depth profile under the influence of traps. The dotted data represent a depth profile that actually has been calculated using the computer code PIDAT (confer to Section 2.4).

If trapping occurs, it is reasonable to define an apparent diffusion coefficient, which is approximately  $D$  if almost all trap sites are occupied ( $N_t(x, t)/H_t(x, t) \simeq 1$ ) and equal to  $D(N_d(x, t)/N_t(x, t))$  if the fraction of occupied trap sites is much less than unity ( $N_t(x, t)/H_t(x, t) \ll 1$ ) [112]. This dependence of the apparent diffusion coefficient is due to the fact that at diffuser concentrations lower than the trap concentration, the diffusional transport is not limited by the jump frequency of the diffuser on diffusion sites, but by the escape frequency from trap sites [112].

## 2.4 Approaches to transport modeling

### 2.4.1 The time and depth dependent concentration

Modeling approaches that describe the full time and depth dependence of the concentration of an implanted element that diffuses under the influence of traps<sup>11</sup> have been developed, for example, by Möller et al. [113] and Myers et al. [109]. In this work the baseline of their formalisms is picked up: The time and depth dependence of the concentration is described by a combined set of diffusion and trapping equations in connection with a source term  $S(x, t) = j_{\text{in}} f_{\text{R}}(x)$ , where  $j_{\text{in}}$  is the flux of incident energetic nitrogen atoms (per unit area and unit time) and  $f_{\text{R}}(x)$  is the projected range distribution of nitrogen. Nitrogen is assumed to be implanted on diffusion sites resulting in the combined set of equations

$$\frac{\partial}{\partial t} N_{\text{d}}(x, t) = D \frac{\partial^2}{\partial x^2} N_{\text{d}}(x, t) + S(x, t) - \frac{\partial}{\partial t} N_{\text{t}}(x, t), \quad (2.10)$$

and

$$\frac{\partial}{\partial t} N_{\text{t}}(x, t) = k_{\text{d} \rightarrow \text{t}} N_{\text{d}}(x, t) \left( 1 - \frac{N_{\text{t}}(x, t)}{H_{\text{t}}(x, t)} \right) - k_{\text{t} \rightarrow \text{d}} N_{\text{t}}(x, t) \quad (2.11)$$

The trapping coefficient  $k_{\text{d} \rightarrow \text{t}}$  and the detrapping coefficient  $k_{\text{t} \rightarrow \text{d}}$  are chosen as  $k_{\text{d} \rightarrow \text{t}} = 4\pi r_{\text{t}} H D_0 e^{-E_{\text{d}}/kT}$  and  $k_{\text{t} \rightarrow \text{d}} = 4\pi r_{\text{t}} H D_0 e^{-E_{\text{t} \rightarrow \text{d}}/kT}$ , respectively, where  $r_{\text{t}}$  denotes a characteristic capture radius of an individual trap site taken as the lattice constant,  $H$  the concentration of host atoms,  $D_0$  the pre-exponential factor of diffusion,  $E_{\text{d}}$  the diffusion activation energy, and  $E_{\text{t} \rightarrow \text{d}}$  the detrapping activation energy. The boundary condition at the surface is of essential influence for the solution of the above set of equations. Only for some idealized boundary conditions and source terms analytical solutions can be given [114, 65], otherwise the solution requires numerical methods. In this work the computer program PIDAT [115] has been employed in connection with the GEAR package [116, 117] to solve the set of equations<sup>12</sup>. An example of a depth profile calculate using PIDAT has already been shown in Figure 2.6. Time and depth dependent modeling of the nitrogen concentration under the influence of traps – extended towards the consideration of two nitrogen isotopes – will be presented in Section 4.1 in order to reveal information on the nitrogen diffusion mechanisms.

### 2.4.2 The retention rate

The nitrogen retention rate  $j_{\text{ret}}(t)$  is given by the difference of the flux of nitrogen incorporated through the surface into the substrate  $j_{\text{inc}}$  and the flux of nitrogen released through the surface  $j_{\text{rel}}$

$$j_{\text{ret}}(t) = j_{\text{inc}}(t) - j_{\text{rel}}(t), \quad (2.12)$$

with  $j_{\text{ret}}(t)$ ,  $j_{\text{inc}}(t)$ , and  $j_{\text{rel}}(t)$  in units of at./cm<sup>2</sup>s. As indicated in Figure 2.7 in ion nitriding, by its definition, the term  $j_{\text{inc}}$  will be dominated by the flux of incident energetic

<sup>11</sup>For the diffusional transport under the influence of traps the assumptions listed in Section 2.3 are made.

<sup>12</sup>Many thanks to Prof. W. Möller for providing the program.

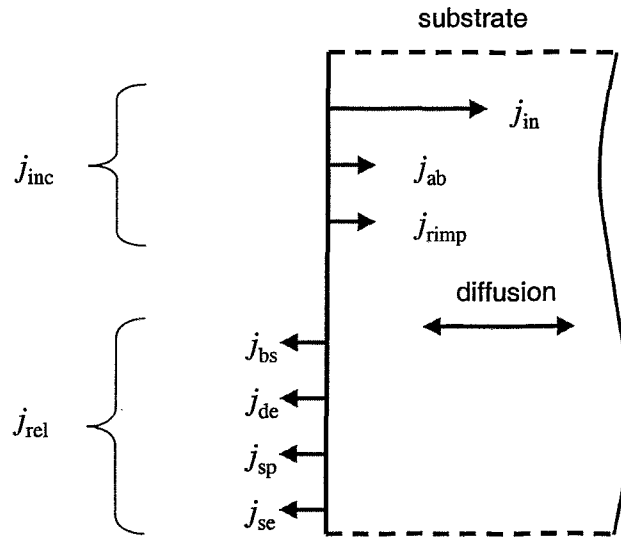


**Figure 2.7:** A scheme showing mechanisms with potential relevance for incorporation and release of nitrogen.  $j_{inc}$  is the incorporated nitrogen flux,  $j_{rel}$  is the released nitrogen flux, and  $j_{in}$  is the energetic nitrogen flux impinging on the surface.  $j_{ab}$ , and  $j_{rimp}$  are the nitrogen fluxes resulting from absorption, and recoil implantation, respectively.  $j_{bs}$ ,  $j_{de}$ ,  $j_{sp}$ , and  $j_{se}$  are the nitrogen fluxes resulting from backscattering, desorption, sputtering, and spontaneous emission, respectively. All fluxes are given in units of nitrogen atoms per unit area and unit time.

nitrogen  $j_{in}$ . On the other hand backscattering, and sputtering are always associated with ion implantation and will contribute to the flux of released nitrogen. Other mechanisms as, for example, absorption from and desorption to the residual gas, recoil implantation of adsorbed nitrogen, and spontaneous emission of nitrogen may, in principle, contribute to the incorporated, respectively released nitrogen flux. The identification and characterization of the relevant incorporation and loss mechanisms will be a subject of Section 4.3.

### 2.4.3 The evolution of the layer thickness

Another modeling approach considers the evolution of the layer thickness during diffusion limited layer growth at (i) constant surface concentration, (ii) a diffusion coefficient  $D$  independent of time, and (iii) a constant surface recession rate. In Equation 2.7,  $x$ -coordinates at which the concentration remains constant with time, evolve according to

$$x = 2\beta\sqrt{Dt}, \quad (2.13)$$

where  $\beta$  is a constant [108]. Defining the layer thickness  $X$  as the distance between the surface and the depth, at which the concentration has dropped to half of the surface

concentration,  $\beta$  is 0.5 [85]<sup>13</sup> and the layer thickness evolves in time according to

$$X = \sqrt{Dt}. \quad (2.14)$$

Taking the derivative of Equation 2.14 with respect to time, the layer growth rate is given by

$$\frac{dX}{dt} = \frac{\sqrt{D}}{2\sqrt{t}}, \quad (2.15)$$

or by (solve Equation 2.14 for  $\sqrt{t}$  and substitute in Equation 2.15)

$$\frac{dX}{dt} = \frac{D}{2X}. \quad (2.16)$$

Equation 2.16 is also known as Wagner's equation [118, 119]. It predicts the evolution of the layer thickness during diffusion limited layer growth at (i) constant surface concentration and (ii)  $D$  independent of time (no phase transformation). During surface modification processes that involve ion bombardment, surface recession due to sputtering takes place. At constant processing parameters and constant surface concentration the surface recession rate  $j_{SR}$  can be considered as constant. The net growth rate of the layer can be expressed by a linear superposition of Equation 2.16 and the surface recession rate:

$$\frac{dX}{dt} = \frac{D}{2X} - j_{SR}. \quad (2.17)$$

Thus, as shown in Figure 2.8, the evolution of the layer thickness during diffusion limited layer growth at (i) constant surface concentration, (ii) a diffusion coefficient  $D$  independent of time, and (iii) a constant surface recession rate, is dominated by a parabolic term for small layer thicknesses. With increasing layer thickness a deviation from the parabolic behavior becomes more and more prominent. At a certain point the growth term and the surface recession term come to equilibrium, that is, the thickness of the layer becomes stationary. Setting  $dX/dt = 0$  the stationary thickness  $X_{stat}$  is given by

$$X_{stat} = \frac{D}{2j_{SR}}. \quad (2.18)$$

It should be noted here that a similar approach – which also accounts for multiple mono-phase layers – has been presented recently by Dimitrov et al. [119, 120, 121, 122]. Dimitrov et al. also suggested to calculate first  $D$  from the parabolic part of the evolution of the layer thickness (relatively short times, respectively small layer thicknesses) using Equation 2.16, and then  $j_{SR}$  by fitting Equation 2.17 to the complete time dependence (including relatively long times respectively large layer thicknesses) of the layer thickness [122]. In this work the approach will be applied following this suggestion (Section 4.4). Additionally, in Section 4.5, a refined approach that distinguishes between rate of supply limited growth and diffusion limited growth will be presented and applied in order to model the evolution of the surface oxide layer thickness during ion nitriding.

<sup>13</sup>note that  $\text{erf}(0.5) \approx 0.5$ .

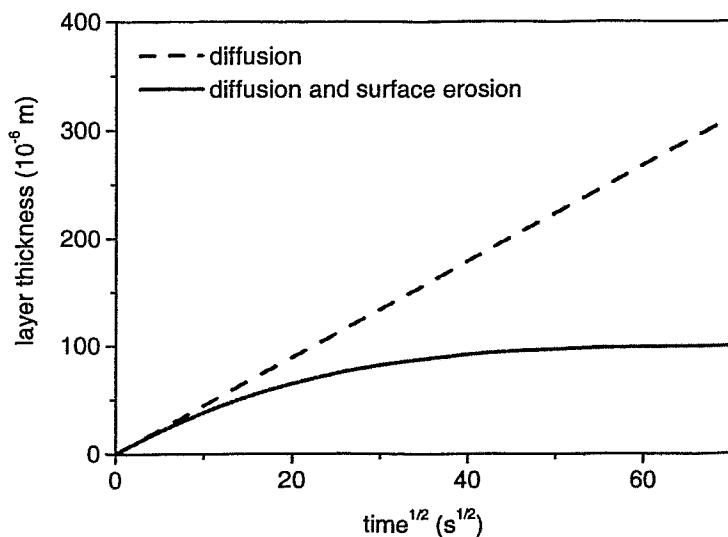


**Figure 2.8:** A schematic example of the evolution of the layer thickness for (i) diffusion limited growth (dashed line, Equation 2.16) and (ii) diffusion limited growth at constant surface recession (solid line, Equation 2.17).  $D = 2 \times 10^{-7} \text{ cm}^2/\text{s}$  and  $j_{\text{SR}} = 1 \times 10^{-5} \text{ cm/s}$  have been assumed.



# Chapter 3

## Material and experimental methods

### 3.1 Material

In this work grade AISI 316 steel has been chosen as a representative of austenitic stainless steels<sup>1</sup>. Solution annealed, drawn rods of about 30 mm diameter were purchased from *Fry Steel Company, Santa Fe Springs, CA*<sup>2</sup>. The composition according to the certificate of test is given in Table 3.1 together with the composition range required according to the AISI 316 specification [123].

Element	Symbol	req. conc. (wt.%)	cert. conc. (wt.%)	cert. conc. (at.%)
Carbon	C	≤ 0.08	0.019	0.09
Manganese	Mn	≤ 2.0	1.79	1.82
Phosphorus	P	≤ 0.045	0.028	0.05
Sulfur	S	≤ 0.03	0.025	0.04
Silicon	Si	≤ 1.0	0.38	0.76
Chromium	Cr	16.0 - 18.0	16.17	17.43
Nickel	Ni	10.0 - 14.0	10.08	9.57
Cobalt	Co	-	0.12	0.11
Copper	Cu	-	0.33	0.29
Molybdenum	Mo	2.0 - 3.0	2.07	1.21
Nitrogen	N	-	0.069	0.28
Iron	Fe	Balance	Balance	Balance

Table 3.1: Required and certified composition of AISI 316

<sup>1</sup>AISI 316 is a material classification of the American Iron and Steel Institute for one of the most prominent austenitic stainless steel grades, corresponding approximately to the European classification EN 1.4401.

<sup>2</sup>Many thanks to Prof. D. Williamson for providing the material.

Specimens with diameters varying from 12 mm to 30 mm and a thickness of approximately 2.5 mm were machined from the rods. A hole of 1 mm diameter, that later served to pick up a thermocouple, was drilled sidewise into the disks. The specimens were mechanically polished to mirror finish and rinsed in organic solvent<sup>3</sup>. Virgin samples were analyzed by different techniques<sup>4</sup>:

- Atomic force microscopy revealed a mean surface roughness of less than 10 nm.
- Scanning auger microscopy showed no evidence for a lateral inhomogeneity of the native surface oxide layer.
- Conversion electron Mössbauer spectroscopy was consistent with a fcc crystal lattice structure and showed no evidence for a near surface phase transformation, as it sometimes is observed on similar types of stainless steel [124].
- X-ray diffraction analysis was also consistent with a fcc crystal lattice structure.
- Optical microscopy identified the microstructure typical for austenitic stainless steels.
- Slow positron implantation spectroscopy revealed that the virgin samples exhibited a damaged surface layer of about 1500 nm thickness.

The formation of the damaged layer can be attributed to the mechanical preparation of the surface. Consistent with a relatively high mobility of defects, Anwand et al. found that the damaged layer disappeared after a short annealing at 400 °C [125]. Therefore, each sample was briefly annealed at the above temperature before the ion nitriding started.

Note that measurements made in the beginning of the work were performed on AISI 316Ti steel. This grade is similar to AISI 316, but showed small amounts of ferrite. In the following we will not distinguish between the two grades.

---

<sup>3</sup>Many thanks to Mr. H. Seifert and Mrs. R. Aniol for mechanical preparation of the samples.

<sup>4</sup>Many thanks to Mrs. K. Fukarek for atomic force microscopy, to Mrs. E. Quaritsch for scanning auger microscopy, to Dr. M. Dobler for conversion electron Mössbauer spectroscopy, to Dr. M. Betzl and Mrs. A. Scholz for x-ray diffraction, to Dr. G. Brauer and Mr. W. Anwand for slow positron implantation spectroscopy, and to Mrs. R. Opitz for optical microscopy.

## 3.2 Material modification

A sketch of the ion nitriding system that has been built up for the present work is shown in Figure 3.1. An ultrahigh vacuum chamber houses a hot filament ion source. The ion source supplies a broad nitrogen ion beam which is directed towards the sample. A rotary and linear motion feedthrough is installed on the ion source flange. It holds a Faraday cup and a filament heater. The Faraday cup serves for the control of the ion current density. The filament heater is employed to minimize discontinuities of the heat flux to the sample that occur when the nitriding treatment is started and stopped by swaying the motion feedthrough.

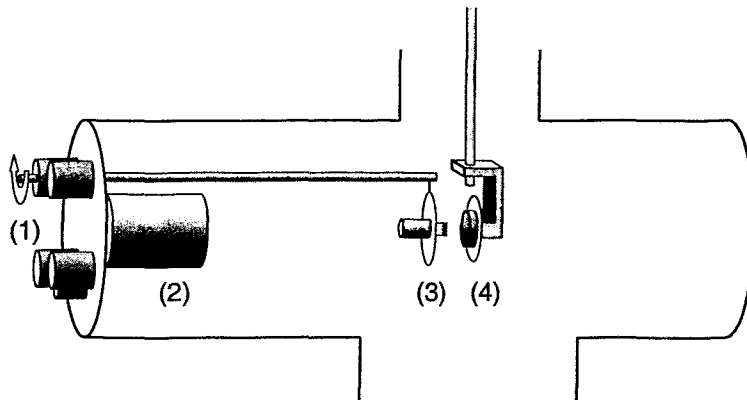


Figure 3.1: A sketch (side view) of the ion nitriding system showing: (1) the ion source flange, (2) the ion source, (3) the shutter mounting the Faraday cup and the filament heater, and (4) the sample.

### 3.2.1 The ion source

The ion source (Figure 3.2) has been developed by the *Institut für Oberflächenmodifizierung, Leipzig, Germany* and is described in detail in Ref. [126]. It is a hot filament, broad beam source that can operate all inert and many reactive gases at low gas fluxes. The inner body of the source is on a positive potential (beam voltage  $U_b$ ). Electrons are emitted from a hot filament (filament voltage  $U_f$ ). They get accelerated towards the anode (discharge voltage  $U_d$ ). On their way to the anode they dissociate and ionize gas molecules. A plasma with uniform distribution is generated. From that plasma a broad beam of positively charged ions is extracted by a planar grid system (acceleration voltage  $U_a$ ). In this work a carbon grid system of 40 mm diameter and a molybdenum grid system of 20 mm diameter have been employed, the latter one when oxygen was fed to the residual gas. The source has been operated at  $U_d = 100$  V and  $U_a = -300$  V. Extrapolation of data presented in Ref. [126] suggests that at these parameters the extracted nitrogen ion beam consists of about equal fractions of  $N_2^+$  and  $N^+$  and that the ion energy has a

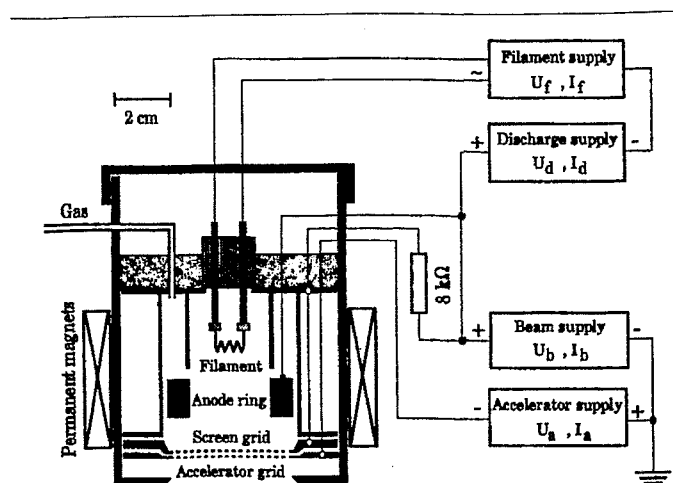


Figure 3.2: A schematic view of the ion source (from Ref. [126]).

relatively sharp distribution around  $U_b$ . Therefore, a sharp ion energy of  $E_{in}$  and a ratio of  $N_2^+ : N^+ \approx 50 : 50$  are assumed throughout this work. The ion energy  $E_{in}$  and the ion current density  $\rho$  have been varied by changing  $U_b$  and  $U_f$ , respectively. The latter one is measured by the Faraday cup that suppresses secondary electrons by a negative voltage of 150 V that is put on a counter electrode close to its entrance. The lateral uniformity of the ion flux density in the plane of the sample surface has been checked to be better than approximately 10% over a diameter of 40 mm using the carbon grid system, respectively over a diameter of 20 mm using the molybdenum grid system.

After finishing this work the nitrogen ion beam extracted from the ion source has been analyzed with a commercial mass spectrometer<sup>5</sup>. As a result of these investigations it has been found that the ion energy was probably subject to a strong oscillation around  $E_{in}$ . Additionally, it appears to be more reasonable to assume a ratio of  $N_2^+ : N^+ \approx 80 : 20$  instead of 50 : 50. A brief investigation on the consequences of these findings is presented in Appendix A, showing that the quality of the results obtained by assuming a sharp energy and  $N_2^+ : N^+ \approx 50 : 50$  is not substantially deteriorated.

### 3.2.2 The vacuum system

The ultrahigh vacuum chamber can be pumped by a turbomolecular pump coupled with a rotary pump, two cryogenic pumps and a triode pump. For total pressure measurement a pirani gauge head and a cold cathode gauge are installed. The gas flux to the source is adjusted by a mass flow controlled gas inlet (*mass flow controller: AFC-260, ASM, Bilthoven, The Netherlands; control unit: Type 247C, MKS, Andover, Massachusetts*). A separate gas inlet that is optionally controlled by a needle valve or mass flow controller

<sup>5</sup>These investigations have been performed by Dr. T. Chevolleau and Miss T. Telbizova.

and a quadrupole mass analyzer *QMG/A/E064*, *Balzers, Liechtenstein* serve to tune the oxygen partial pressure of the residual gas. Normally, the turbomolecular and one cryogenic pump are active resulting in a base pressure of less than  $1 \times 10^{-5}$  Pa. During processing the ion source is supplied with a gas flux of  $\approx 1$  sccm resulting in a processing pressure of approximately  $5 \times 10^{-3}$  Pa. At this pressure molecular gas flow can be assumed and the mean free path length of the nitrogen ions is large compared to the distance between the ion source and the substrate [127]. A simple calculation yields that the effective gas flux directed from the gas inlet towards the pumps has a density that is smaller than the non-directed thermal gas flux density.

### 3.2.3 The sample mount

A sample mount system *STLC*, *Thermionics, Hayward, California* is installed on a manipulator with *xyz* translation and a rotational degree of freedom around the horizontal plane. The system consists of a sample dock that houses a boron nitride heater, a sample platen, a linear-rotary transfer rod, and a load lock. This system has been modified to allow for temperature measurement inside the sample. The sample gets fixed on the sample platen by three clips and a coated isolated Ni/CrNi thermocouple is stuck into a hole which has been drilled sidewise into the sample. On the back side of the sample the thermocouple wires are connected to isolated Ni/CrNi contacts. The sample platen can be exchanged without severely affecting the vacuum conditions via the load lock and the linear-rotary transfer rod along with the sample and the thermocouple. When the sample platen is locked to the sample dock the thermocouple contacts on the back side of the sample platen get connected to respective contacts on the sample dock. From there, thermocouple wires lead to a thermocouple feedthrough. In a stationary temperature regime, that can be assumed for the ion nitriding treatments presented in this work, the difference between the temperature measured in the hole and the temperature close to the sample surface is limited by the heating power of the ion beam and the thermal conductivity of the sample. An upper limit of 2 K can be calculated.

### 3.2.4 Processing, process control, and coupling to physical parameters

Before starting an ion nitriding treatment the shutter is positioned in front of the sample. The source is ignited. The desired ion energy  $E_{in}$  and ion current density  $\rho$  are established. The latter one is measured by the Faraday cup on the shutter. The sample is heated to the desired temperature by the boron nitride heater and the filament heater. The heating power, which is supplied to the sample by the latter, is chosen such that it corresponds to the heating power that the ion beam supplies during ion nitriding. Temperature and ion current density are monitored by a data acquisition unit *Hydra 2625*, *Fluke, Everett, Washington*. The ion nitriding treatment is started by swaying the motion feedthrough. During the treatment the steadiness of the ion current density is monitored by the Faraday cup that is swayed to the side. Slight shifts of the sample temperature are compensated by adjusting the heating power of the boron nitride heater. The treatment is stopped by

processing parameter	corresponding symbol	range of variation
ion energy	$E_{in}$	0.3 – 2.0 keV
ion current density	$\rho$	0.01 – 1.0 mA/cm <sup>2</sup>
sample temperature	$T$	280 – 480 °C
partial pressure of O <sub>2</sub>	$p(O_2)$	$< 3 \times 10^{-5} - 9 \times 10^{-3}$ Pa
time	$t$	2 – 240 min

**Table 3.2:** Processing parameters of ion nitriding and the range over which they have been varied in this work.

swaying the shutter again in front of the sample. The absolute value of the ion current density is checked. Then the ion source and both heaters are switched off and the sample cools down with an initial cooling rate of approximately 50 K/min. Table 3.2 lists the processing parameters that unequivocally describe the ion nitriding treatment. Additionally listed are the ranges over which these parameter have been varied in this work.

The processing parameters are identical or closely coupled to the physical parameters of ion nitriding: From the ion current density  $\rho$  and the ratio of  $N_2^+ : N^+ \approx 50 : 50$  the incident flux of energetic nitrogen atoms results as  $j_{in} = 1.5 \times \rho/e$ , where  $e$  is the elementary charge. The projected range distribution  $f_R(x)$  and the sputtering yield  $SY$  depend on the ion energy. Generally, a  $N_2^+$  ion with the kinetic energy  $E_{in}$  can be considered as two  $N^+$  ions each with kinetic energies  $E_{in}/2$ . Consequently, the mean projected range and the sputtering yield can be estimated by weighted superpositions of SRIM or TRIDYN simulations as  $(\overline{R_p}(E_{in}) + 2\overline{R_p}(E_{in}/2))/3$  and  $(SY(E_{in}) + 2SY(E_{in}/2))/3$ , respectively. Neglecting the non-thermal flux of oxygen, the incident flux of oxygen atoms is given by kinetic gas theory according to  $2p(O_2)/\sqrt{2\pi mkT_G}$ , where  $p(O_2)$  denotes the oxygen partial pressure,  $k$  the Boltzmann constant,  $T_G$  the temperature of the gas (assumed to be room temperature), and  $m$  the mass of an oxygen molecule.

In summary, with the choice of the hot filament ion source, the modification process is designed to be well controlled and flexible. The process can be described by a reasonable number of independent processing parameters that are closely coupled to physical parameters. With these features the premise for a feasible description of the nitrogen transport in terms of physics is fulfilled. The results are not limited to a specific process or setup, but they can be compared or transferred to an arbitrary surface modification process the physical parameters of which are known.

## 3.3 Material analysis

The analytical techniques that have been employed in this work are x-ray diffraction (XRD), slow positron implantation spectroscopy (SPIS), glow discharge optical emission spectroscopy (GDOES), and the ion beam analysis techniques elastic recoil detection analysis (ERDA) and nuclear reaction analysis (NRA). Among these techniques, ERDA and NRA were used most intensively and will therefore be introduced and described in greater detail. The other techniques were performed as analytical services<sup>6</sup> and will be briefly introduced where experimental results obtained by them are presented for the first time.

### 3.3.1 A brief introduction to ion beam analysis

Ion beam analysis techniques require particle accelerators, vacuum conditions, and nuclear pulse processing setup. Their strength resides in the ability to obtain absolute elemental depth profiles, the speed of the analyses, and their non-destructive character. Typically, a beam of monoelemental and monoenergetic ions with ion energies and ion currents in the range of  $\approx 1$  MeV/amu and  $\approx 1$  nA, respectively, is directed towards the sample under investigation. The number and energy distribution of particles ejected into a fixed solid angle is measured by a detector.

The spectra can be transformed into absolute elemental depth profiles by applying only two physical concepts: (i) the slowing down of swift charged particles in matter, and (ii) the kinematics of a single binary scattering event. In the energy range of interest the former is dominated by the interaction of the swift particles with the sample electrons. The stopping power, which is the measure for the amount of energy lost after travelling through a certain amount of material, can generally be considered as well known by applying semi-empirical data [99] and Bragg's-rule [128]. While the interaction with the sample electrons does not lead to considerable scattering, the interaction with the sample nuclei does. The latter can be described in terms of binary scattering events. A measure of the probability for a scattering product to be detected by the detector is the differential cross section.

The scattering process is called elastic if (i) the total kinetic energy is conserved in the scattering event itself and (ii) the internal energy of the particles does not play a role. At sufficiently high energies screening by the atomic electrons can be neglected and the differential cross section is given by the well known Rutherford-Formula [129]. This is the case for ERDA where recoiled sample atoms are detected as well as for the related technique Rutherford backscattering spectroscopy where backscattered projectiles are detected. If both kinetic and internal energy are involved in the interaction and atomic or nuclear excitations occur, the scattering process is called inelastic. New particles are eventually formed during the scattering process and the differential cross section is a measure that usually has to be determined experimentally. This is the case for NRA.

While Rutherford backscattering spectroscopy is the predominant technique for depth profiling of heavy elements, ERDA and NRA are particular suited for depth profiling of

---

<sup>6</sup>Many thanks to Dr. M. Betzl and Mrs. A. Scholz for XRD measurements and to Dr. G. Brauer and Mr. W. Anwand for SPIS measurements. GDOES was performed at *TAZ GmbH, Seefeld, Germany*.

light elements. More detailed introductions to ion beam analysis are given, for example, in Refs. [130, 131].

### 3.3.2 Elastic recoil detection analysis

Elastic recoil detection analysis (ERDA) is the analytical technique that is used most extensively in this work. It has been performed using a 35 MeV  $^{35}\text{Cl}^{7+}$  ion beam, supplied from the Rossendorf 5 MV Tandem accelerator. The beam incidences onto the substrate at  $17.5^\circ$  with respect to the substrate surface. Recoiling substrate atoms are detected around a scattering angle of  $35^\circ$  (Fig. 3.3). Through a thin entrance window the recoils enter

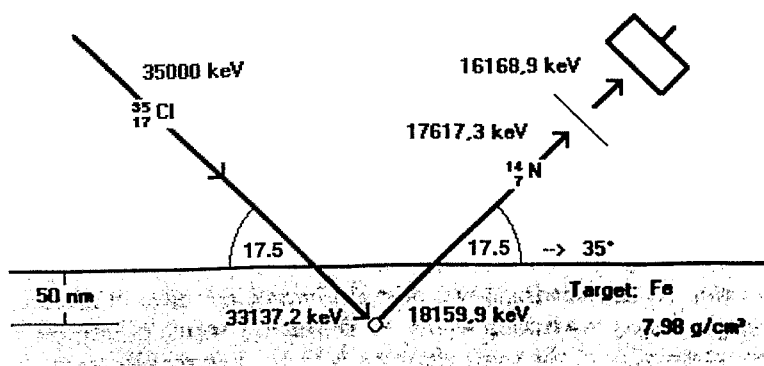


Figure 3.3: A sketch, visualizing the principle and the geometry of ERDA as it is performed in this work. The sample normal is in the scattering plane.

a position resolving transversal field ionization chamber that has been cloned from the Munich ERDA-Group of Dr. W. Assmann. A schematic view of this ionization chamber is shown in Figure 3.4. It has a Frisch-grid and an anode electrode that is subdivided into a  $\Delta E$  and an  $E_{\text{rest}}$  part. The atomic number of the recoiled particle is deduced from the  $\Delta E$  signal and the total energy of the recoils is obtained from the sum of the anode signals. The cathode electrode is divided into two insulated halves with "backgammon" shape. By this construction the trajectory of the recoils in the chamber can be resolved with a lateral accuracy of better than 5 mm. Thus, the chamber allows for the use of a large solid angle — which increases the speed of the analyses — without a severe deterioration of the depth resolution. A more detailed description of the chamber is given in Refs. [133, 132].

A typical spectrum of an ion-nitrided stainless steel sample is shown in Figure 3.5. Such spectra can be transformed into absolute elemental depth profiles. The yield  $Y_i$ , for the recoil atoms  $i$  detected in the energy channel  $E_k$  with a channel width of  $\delta E_k$ , is given by

$$Y_i(E_k) = \frac{Q \Omega N_i(x) \sigma_i(E'_0, \phi) \delta E_k}{\sin \Theta dE_k/dx}, \quad (3.1)$$



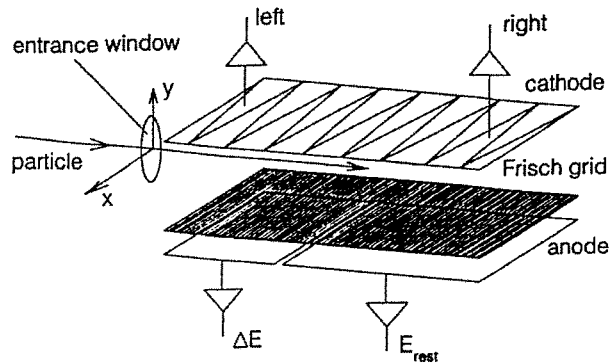


Figure 3.4: A schematic view of the layout of the ionization chamber (from Ref. [132]).

where  $Q$  is the incident projectile fluence,  $\Omega$  is the detector solid angle,  $N_i(x)$  is the atomic number density of the recoiled atom  $i$  at depth  $x$ ,  $\sigma_i(E'_0, \phi)$  is the recoil differential scattering cross section at the recoil angle  $\phi$  and the projectile energy  $E'_0$  just prior to scattering,  $\Theta$  is the incident angle of the projectile taken with respect to the surface normal, and  $dx$  is the increment of depth at the depth  $x$ , corresponding to an increment of energy  $dE_k$  [134]. By solving Equation 3.1 for  $N_i(x)$ , absolute depth profiles of atoms  $i$  can be calculated from the spectra. This can be done fully consistent using computer programs that consider the change in composition and the stopping power in an iterative manner [135, 136]. Owing to the large number of spectra that had to be evaluated and since the

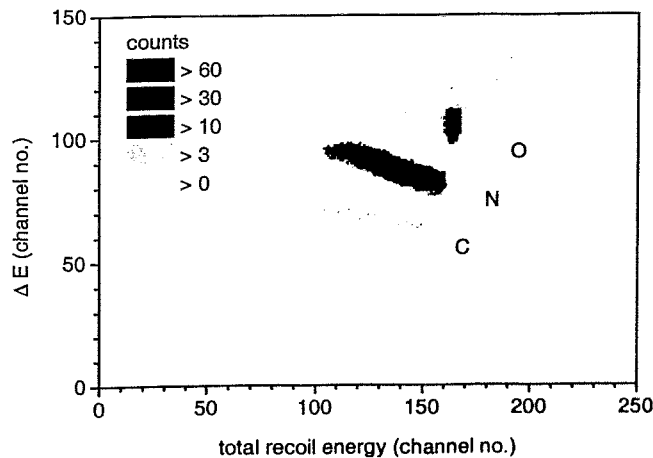


Figure 3.5: An example of an ERDA spectrum obtained from an ion-nitrided (and reoxidized) austenitic stainless steel sample.

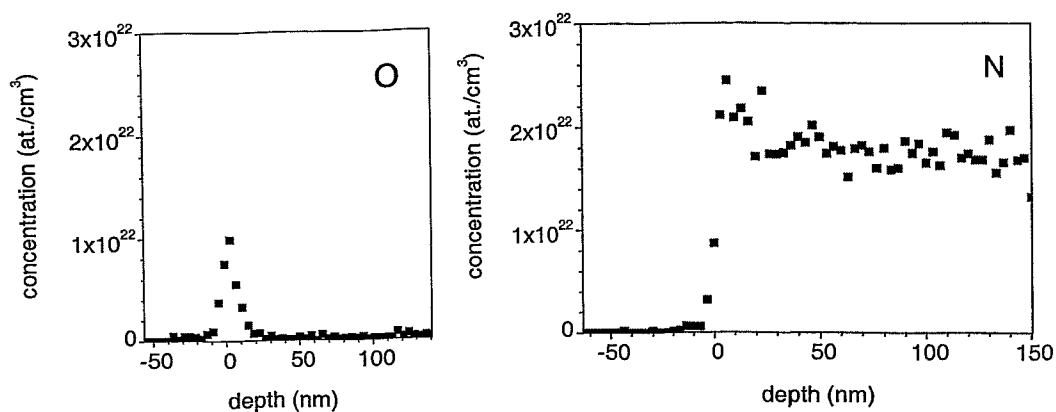


Figure 3.6: Oxygen (left) and nitrogen (right) depth profiles obtained from an ERDA spectrum.

depth unit nm was preferred, a stopping power assumption (in units of keV/nm) is made throughout this work: In order to calculate nitrogen and oxygen depth profiles from the ERDA spectra, stopping powers are assumed, as given by the Ion Stopping Subroutine Stop95 [137] for Fe with a density of 7.98 g/cm<sup>3</sup> and Cr<sub>2</sub>O<sub>3</sub> with a density of 5.21 g/cm<sup>3</sup>, respectively. Resulting depth profiles of oxygen and nitrogen, calculated from the spectrum in Figure 3.5, are shown in Figure 3.6. Table 3.3 provides further information on relevant experimental parameters related to ERDA.

Parameter	Value
projectile	Cl <sup>7+</sup>
incident energy	35 MeV
incident angle	17.5°
detection angle	35°
ion flux	≈ 5 nA
spot size	≈ 1.5 × 1.5 mm
entrance foil	1.5 μm Mylar
ionization chamber gas	isobutane
ionization chamber pressure	3800 Pa

Table 3.3: Standard experimental parameters of ERDA

### 3.3.3 Real-time elastic recoil detection analysis

Taking advantage of the speed and the non-destructive character of the analysis, time-resolved multi-elemental depth profiling becomes feasible with the setup described above. In analogy to the recently developed real-time RBS [138], the analytical technique has been named real-time ERDA. The real-time ERDA setup has been combined with the ion nitriding setup described in Section 3.2. A photograph and a sketch of the combined setup is shown in Figure 3.7. This setup allows for time-resolved depth profiling during defined static or dynamic conditions, including substrate temperature, partial pressures, and ion bombardment.

In this work the combined setup has been mainly used for time-resolved depth profiling of oxygen and nitrogen before, during, and after nitriding. With a few exceptions the analyses have been performed at static conditions, that is, constant sample temperature  $T$ , constant oxygen partial pressure  $p(O_2)$ , constant ion energy  $E_{in}$ , and constant current density  $\rho$ , with the ion bombardment starting during the analysis (the time at which the ion bombardment started is usually set as  $t = 0$ ). Generally, the time- and depth resolution as well as the maximum detection depth of real-time ERDA depend on the substrate material. At the expense of depth resolution, which is limited for systematic reasons to approximately 10 nm, in this work time-resolved depth profiles of oxygen  $O(x, t)$

$$O(x, t) \quad \text{for } x \leq 120\text{nm}, \quad (3.2)$$

and time-resolved depth profiles of nitrogen  $N(x, t)$

$$N(x, t) \quad \text{for } x \leq 150\text{nm}, \quad (3.3)$$

will be shown with a time resolution of 30 s. Examples are shown in Figure 3.8.

As long as the front of the depth profiles does not exceed the maximum detection depth, time-resolved areal densities of oxygen  $O_{ret}(t)$  and nitrogen  $N_{ret}(t)$ , that is, the amount of retained oxygen and nitrogen, respectively, can be extracted from the respective time-resolved depth profiles:

$$O_{ret}(t) = \int_0^{120\text{nm}} O(x, t) dx, \quad (3.4)$$

$$N_{ret}(t) = \int_0^{150\text{nm}} N(x, t) dx. \quad (3.5)$$

Additionally, time-resolved near surface concentrations of nitrogen  $N_{ns}(t)$ :

$$N_{ns}(t) = \overline{N(x, t)}, \quad \text{with } 10 \text{ nm} \leq x \leq 50 \text{ nm}, \quad (3.6)$$

are obtained by averaging over a reasonable depth interval of the nitrogen depth profiles, chosen here from  $\approx 10$  nm to  $\approx 50$  nm. Examples are shown in Figure 3.9.

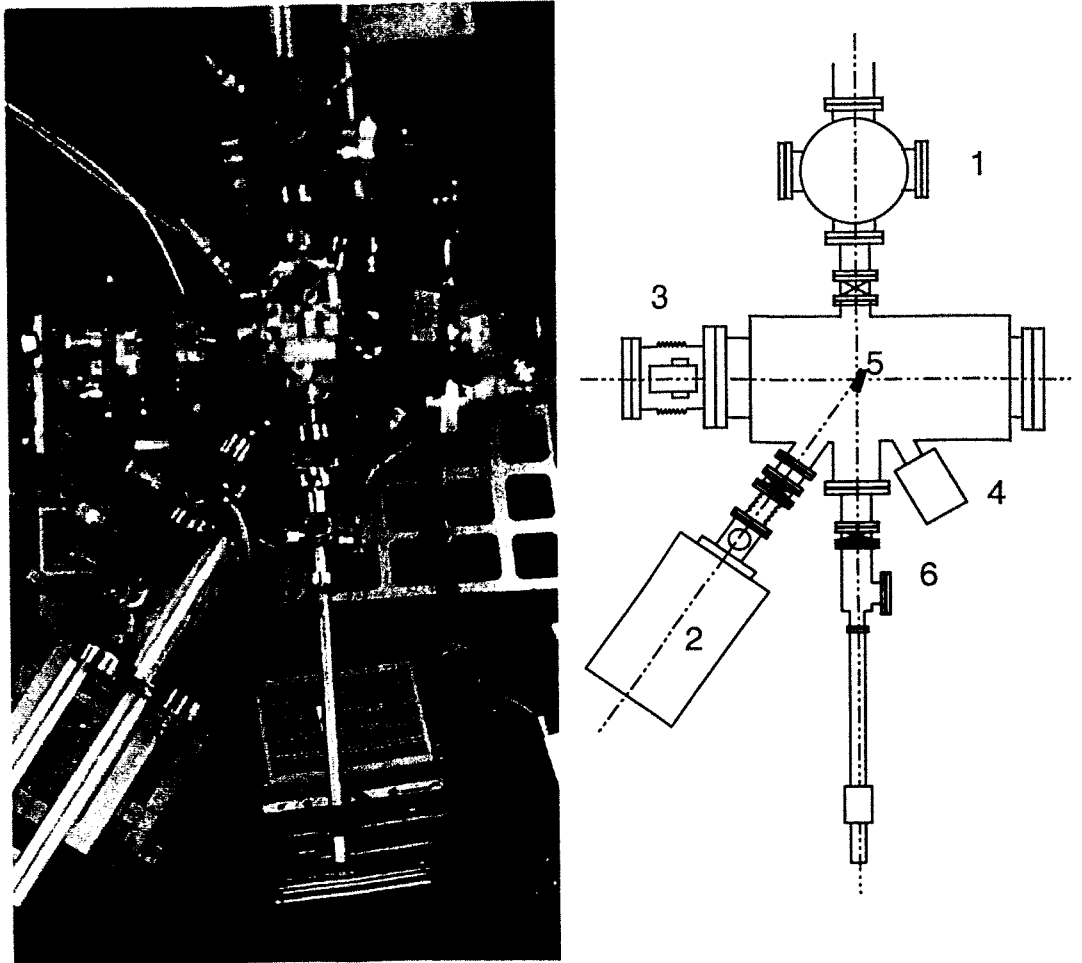


**Figure 3.7:** A photograph and sketch (both top view) of the experimental setup combining ERDA and low energy ion implantation for simultaneous depth profiling of oxygen and nitrogen during ion nitriding showing (1) the high-energy ion current monitor, (2) the ionization chamber, (3) the low energy ion source, (4) the quadrupole mass spectrometer, (5) the sample holder, (6) the load lock.

It should be noted here in the context of real-time ERDA that the non-destructive character of ion beam analysis techniques bases on the fact that the number of ions necessary to obtain depth profiles is small compared to the number of atoms in the layer under investigation. However, care has to be taken as significant beam induced compositional and structural changes can occur already at relatively low ion fluences. These could lead to artefacts as, for example, beam induced nitrogen release or oxygen incorporation. Thus, we

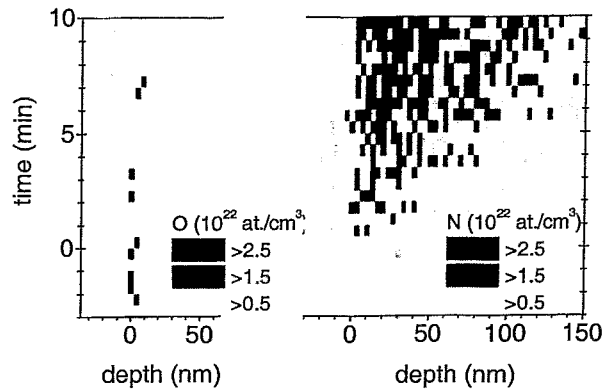


**Figure 3.8:** Examples of time-resolved depth profiles of oxygen (left) and nitrogen (right) obtained by real-time ERDA before and during ion nitriding. Ion bombardment starts at time  $t = 0$ . The color scale represents the respective concentration in units of  $10^{22}$  at./ $\text{cm}^3$ .

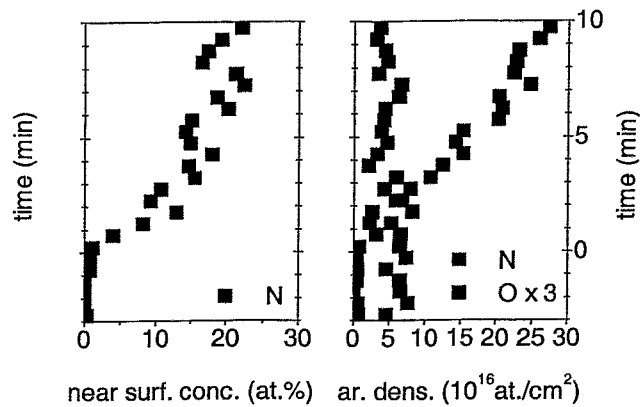


**Figure 3.9:** Examples of time-resolved areal densities of oxygen and nitrogen and time-resolved surface concentrations of nitrogen as obtained by real-time ERDA before and during ion nitriding starting at time  $t = 0$ . Note that the dependent variable time is plotted along the ordinate for better comparison with the time-resolved depth profiles.

checked experimentally if such artefacts occur, with the result that the nitrogen transport is unaffected by the chlorine ion bombardment, while evidence of beam induced oxygen incorporation has been found at elevated oxygen partial pressures. In order to minimize the latter effect, the samples were moved up and down under the analyzing chlorine beam, whenever real-time ERDA was performed at elevated oxygen partial pressures. Finally, it

should be noted that the measurement of oxygen depth profiles is influenced by background due to pulse pile up. For the presented real-time ERDA data, subtraction of the background is difficult. An upper limit for the contribution of pulse pile up to the measured areal density of oxygen has been estimated as  $1.5 \times 10^{15}$  at./cm<sup>2</sup>, corresponding to about one monolayer of stoichiometric Cr<sub>2</sub>O<sub>3</sub>.

### 3.3.4 Nuclear reaction analysis

Nuclear reaction analysis (NRA) has been applied for many years in the measurement of nitrogen depth profiles and nitrogen areal densities [139, 140]. In this work the  $^{14}\text{N}(d, \alpha)^{12}\text{C}$  and the  $^{15}\text{N}(d, \alpha)^{13}\text{C}$  reactions are used to determine  $^{14}\text{N}$  depth profiles up to a depth of 2500 nm (at an incident deuteron energy 1.4 MeV) and to determine  $^{14}\text{N}$  and  $^{15}\text{N}$  depth profiles up to a depth of 1000 nm (at an incident deuteron energy 1.2 MeV). The fortuitous combination of Q-values and cross sections of these reactions make them the ideal choice for simultaneous depth profiling of  $^{14}\text{N}$  and  $^{15}\text{N}$  [139]. The deuteron beam, supplied by the Rossendorf 3 MV Tandetron accelerator, incides perpendicular onto the samples. At a scattering angle of 170° an ion implanted silicon detector of 100 μm nominal thickness is operated at a reduced voltage of 15 V in order to suppress proton induced signals in the interesting range of energy. The nominal energy resolution of the detector is about 15 keV.

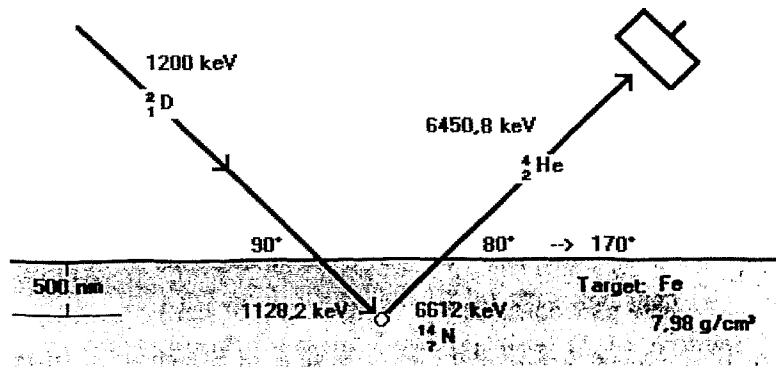


**Figure 3.10:** A sketch visualizing the principle and the geometry of NRA as it is performed in this work. The sample normal is in the scattering plane.

Owing to this energy resolution of the detector the depth resolution is limited to about 50 nm at the surface and increases, primarily due to energy straggling, up to about 170 nm at a depth of 2500 nm. Figure 3.10 visualizes the geometry and the involved particles.

Generally, the use of nuclear reactions for the determination of depth profiles requires detailed knowledge of their cross sections. The two reactions used in this work were explored in earlier works [141, 142, 143, 144]. In the energy range of interest and at similar detection angles they exhibit plateau-type differential cross sections. While the energy dependencies were assumed to be valid, the absolute values of the differential cross sections

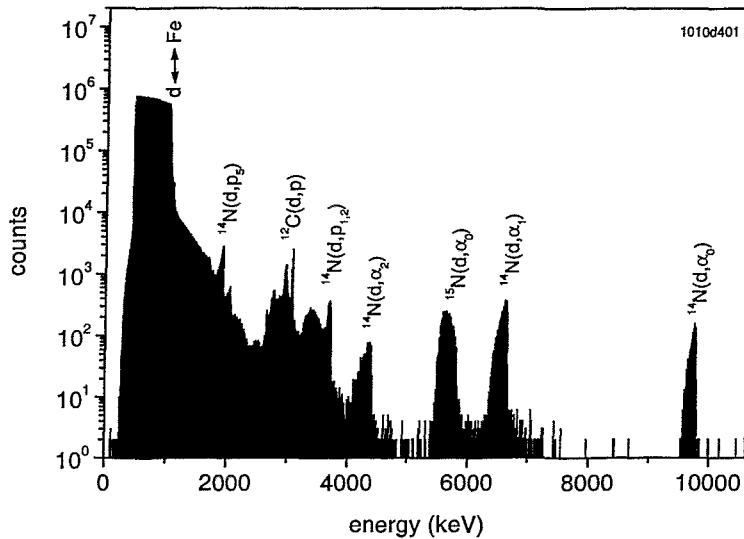


**Figure 3.11:** An example of a NRA spectrum obtained from a stainless steel sample that has been ion nitrided subsequently with  $^{15}\text{N}$  and  $^{14}\text{N}$ . The incident deuteron energy was 1.2 MeV. The deuterium current was  $\approx 5\text{ nA}$  in order to keep dead-time corrections below 5%. The spectrum has been collected at a scattering angle of  $170^\circ$  by an ion implanted silicon detector of  $100\ \mu\text{m}$  nominal thickness that was operated at a reduced voltage of 15 V in order to suppress proton induced signals in the energy range of the  $\alpha$ -particles originating from the  $^{14}\text{N}(d, \alpha_1)^{12}\text{C}$  and  $^{15}\text{N}(d, \alpha_0)^{13}\text{C}$  reactions. Prominent peaks are attributed to their respective nuclear reactions.

were checked by an overall near-surface content approach [130]. Suitable calibration targets were prepared by implanting defined doses of  $^{14}\text{N}$  and  $^{15}\text{N}$ , respectively, into stainless steel substrates<sup>7</sup>. The obtained differential cross section values were  $d\sigma/d\Omega = 1.94\ \text{mb/sr}$  and  $d\sigma/d\Omega = 2.34\ \text{mb/sr}$  for the  $^{14}\text{N}(d, \alpha_1)^{12}\text{C}$  and the  $^{15}\text{N}(d, \alpha_0)^{13}\text{C}$ , respectively. These values are in good agreement with the values reported in Refs. [141, 142] and Refs. [143, 144], respectively, and were used to transform the spectra to depth profiles. An example of a spectrum is shown in Figure 3.11. The spectrum is dominated by deuterium that is elastically backscattered from Fe, Cr, and Ni. Peaks at higher energy can be attributed to protons and  $\alpha$ -particles resulting from deuteron induced nuclear reactions with nitrogen and carbon. As mentioned above, the signals stemming from the  $^{14}\text{N}(d, \alpha_1)^{12}\text{C}$  and  $^{15}\text{N}(d, \alpha_0)^{13}\text{C}$  reactions were used to calculate nitrogen depth profiles. The calculations were performed using a computer program<sup>8</sup>, assuming the checked differential cross sections. Additionally, analogous to the calculation of nitrogen depth profiles from the real-time ERDA data, a

<sup>7</sup>Many thanks to Dr. J. Schöneich for the careful implantation.

<sup>8</sup>Many thanks to Dr. S. Grigull for providing the program and Dr. N.P. Barradas for valuable suggestions.

stopping power assumption has been made. It should be mentioned here that nitrogen depth profiles obtained from real-time ERDA and NRA have been cross checked with each other, with nitrogen depth profiles obtained from time-of-flight ERDA [145, 146] and also with nitrogen depth profiles obtained from glow discharge optical emission spectroscopy, yielding reasonable agreement in all cases.



# Chapter 4

## Results and discussion

### 4.1 The structural nature of the nitrogen enriched layer

#### 4.1.1 Introduction

Successful nitriding of austenitic stainless steels comes along with a structural modification of the nitrogen enriched layer that – compared to the virgin material – is characterized by a broadening of the x-ray diffraction peaks and a systematic shift of the peak positions towards smaller angles. In spite of numerous investigations [32, 31, 35, 147, 75, 148, 149, 68, 150, 151, 152, 153, 154, 155, 156], the nature of the microstructural changes induced in the nitrogen enriched layer is not well understood. Key questions still awaiting clear answers are:

- Does the nitrogen enriched layer consist of a single phase or rather a mixture of phases?
- May the (predominating) phase be interpreted as nitrogen in interstitial solid solution?

As nitrogen on interstitial sites is known to expand and distort the fcc crystal lattice [157, 85, 28], both the shift and the broadening of the x-ray diffraction peaks are qualitatively consistent with nitrogen in interstitial solid solution. Quantitatively, however, the observed peak shifts are sometimes larger [35, 68] than it is expected on the basis of lattice expansions measured for smaller nitrogen contents [158, 159, 160]. Additionally, an anisotropy of the lattice expansion with respect to the crystal lattice orientation has been observed [75, 68, 156]. These and other findings discussed below, led some authors to interpret the induced structural modification as a new phase or a mixture of phases [35, 67, 161, 162, 149, 63].

In this section, an investigation comparing lattice expansions to nitrogen near surface concentrations is presented and discussed. Lattice expansions and nitrogen near surface concentrations have been obtained from x-ray diffraction analysis (XRD) and from nuclear reaction analysis (NRA). Two series of samples that were ion nitrided at different

temperatures, respectively at different oxygen partial pressures, were analyzed. Based on Végard's law [107, 158], a relation between the lattice expansion and the nitrogen content is given. Arguments are provided that the structural modification induced in the nitrogen enriched layer can be interpreted in terms of a single phase with nitrogen in interstitial solid solution.

### 4.1.2 Experimental results

X-ray diffraction analysis has been performed at room temperature in glancing angle geometry using Cu- $K_{\alpha}$  radiation with a mean wavelength  $\lambda = 0.15406$  nm at an incident angle of  $2^{\circ}$ . A scintillation detector has been moved in the plane of the incident radiation and the surface normal from  $2\Theta = 37^{\circ}$  to  $2\Theta = 78^{\circ}$ . For steel about 65% of the detected signal stems from the topmost 150 nm and the information depth is limited to about 500 nm.

Figure 4.1 shows a diffraction pattern of a virgin sample. Peak positions have been

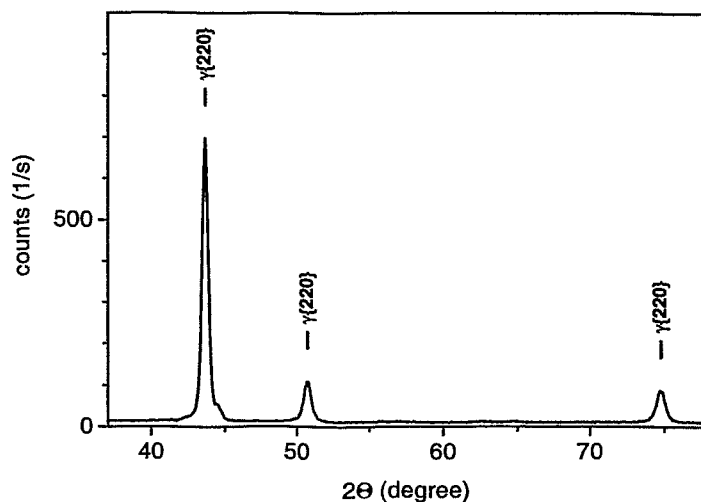


**Figure 4.1:** X-ray diffraction pattern of a virgin sample. The peaks are labeled  $\gamma\{111\}$ ,  $\gamma\{220\}$ , and  $\gamma\{200\}$ . The vertical bars mark the peak positions (here at  $43.67^{\circ}$ ,  $50.74^{\circ}$ , and  $74.76^{\circ}$ , respectively).

determined by taking the center of gaussian fits to the intensity maxima. The peaks are labeled  $\gamma\{111\}$ ,  $\gamma\{220\}$ , and  $\gamma\{200\}$ . From every peak position a corresponding lattice constant has been calculated by applying Bragg's law. Peak positions  $2\Theta$ , corresponding lattice constants  $a$ , the mean lattice constant  $\bar{a}$  calculated by averaging over the lattice constants, and the corresponding mean volume per host atom  $\bar{V} = \bar{a}^3/4$  are listed in Table 4.1. Mean lattice constant and corresponding mean volume per host atom agree well with what is expected from the density and the mean atomic mass of austenitic stainless steel and also with experimental values reported elsewhere [159].

$\gamma\{111\}$		$\gamma\{200\}$		$\gamma\{220\}$		mean values	
$2\Theta$	$a$	$2\Theta$	$a$	$2\Theta$	$a$	$\bar{a}$	$\bar{V}$
(deg.)	(nm)	(deg.)	(nm)	(deg.)	(nm)	(nm)	(nm <sup>3</sup> )
43.67	0.3587	50.74	0.3596	74.76	0.3589	0.3591	0.01158

**Table 4.1:** Peak positions resulting from different crystal lattice planes and corresponding lattice constants obtained from x-ray diffraction analysis of a virgin sample. Additionally given are the mean lattice constant  $\bar{a}$  and the mean atomic volume per host atom  $\bar{V}$ .

Figure 4.2 and Figure 4.3 show x-ray diffraction patterns and corresponding nitrogen depth profiles of samples ion nitrided at different temperatures, respectively different oxygen partial pressures. The thickness of the nitrogen enriched layer increases with increasing temperature and decreasing oxygen partial pressure, respectively. With the exception of the sample treated at the lowest temperature, all samples show new peaks labeled  $\gamma_N\{111\}$ ,  $\gamma_N\{200\}$ , and  $\gamma_N\{220\}$ . Lattice constants, the mean lattice constants, and the mean volume per host atom were calculated from the  $\gamma_N$ -peaks, analogous as for the  $\gamma$ -peaks in case of the virgin sample. Values are listed in Table 4.2 together with the nitrogen near surface concentration  $N_{ns}$ , estimated by averaging over a depth interval from 80 – 160 nm. Additionally listed are the relative variation of the mean lattice constant with respect to the mean lattice constant of the virgin sample

$$\Delta a/\bar{a} = (\bar{a}_N - \bar{a})/\bar{a}, \quad (4.1)$$

and the relative variation of the mean volume per host atom with respect to the mean volume per host atom of the virgin sample

$$\Delta V/\bar{V} = (\bar{V}_N - \bar{V})/\bar{V}. \quad (4.2)$$

As expected for successful nitriding the  $\gamma_N$ -peaks are broader and appear at smaller angles than the  $\gamma$ -peaks. Qualitatively, (i) the intensities of the  $\gamma_N$ -peaks increase with the nitriding depth, (ii) with increasing intensity of the  $\gamma_N$ -peaks the intensity of the  $\gamma$ -peaks decreases, and (iii) the relative variation of the lattice constant, respectively the volume per host atom, increases with increasing nitrogen near surface concentration. While the first two observations can be attributed to the layered structure (a  $\gamma_N$ -layer on  $\gamma$ ), the third one contains information on the structure of the nitrogen enriched layer: For nitrogen in interstitial solid solution a linear dependence between the variation of the mean volume per host atom and the ratio of nitrogen to host atoms is expected according to Vegard's law [107, 158]. Figure 4.4 shows the corresponding plot, which is in good agreement with this expected behavior. A least square fit, forced through zero, yields

$$\Delta V/\bar{V}(\%) = 47.1 \times \frac{N_{ns}}{1/V_N}. \quad (4.3)$$

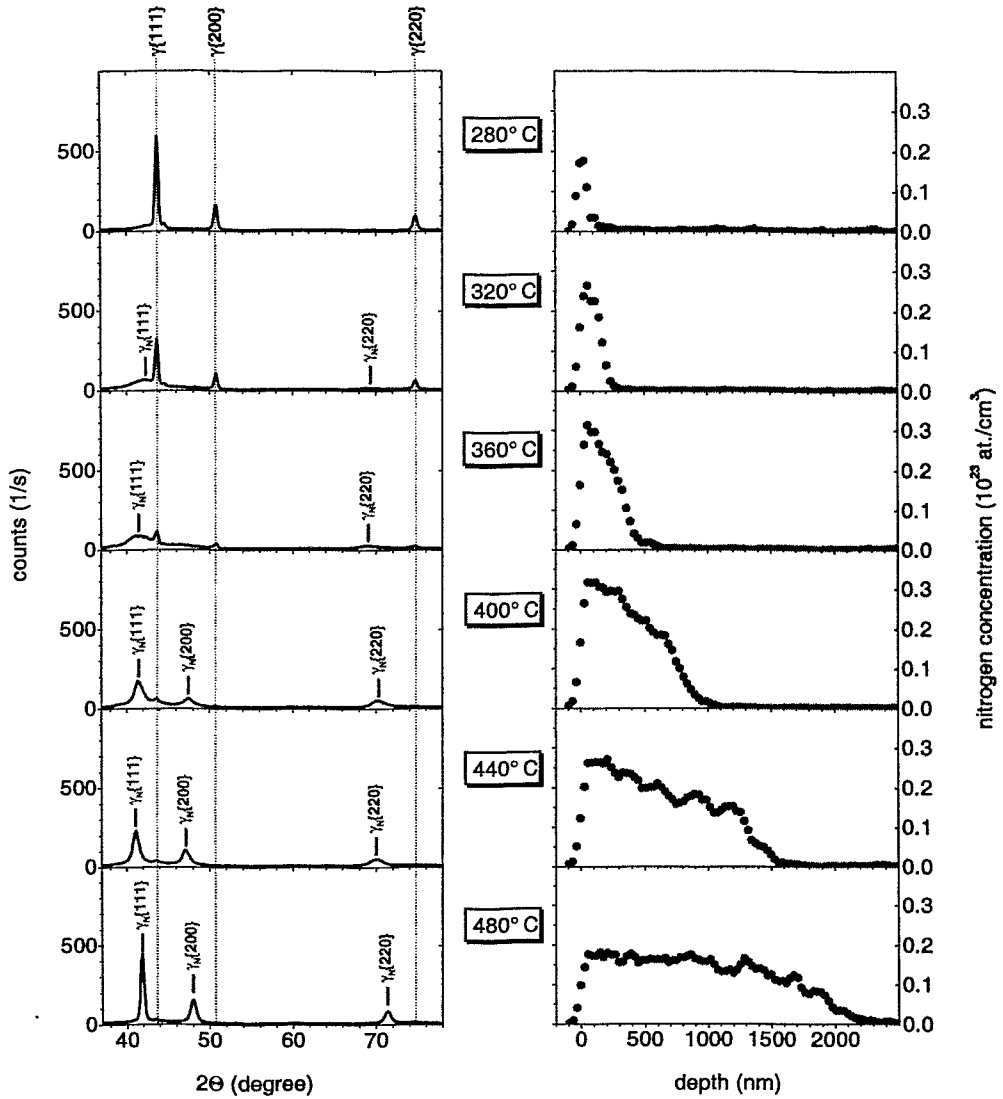


**Figure 4.2:** X-ray diffraction patterns and nitrogen depth profiles of samples ion nitrided at temperatures ranging from 280°C to 480°C. Ion nitriding has been performed for 20 min, at 1 keV, 0.5 mA/cm<sup>2</sup>, and an oxygen partial pressures  $p(O_2) < 3 \times 10^{-5}$  Pa. The lines labeled  $\gamma\{111\}$ ,  $\gamma\{200\}$ , and  $\gamma\{220\}$  mark the positions of the peaks of the virgin sample. The additional peaks are labeled  $\gamma_N\{111\}$ ,  $\gamma_N\{200\}$ , and  $\gamma_N\{220\}$ . The vertical bars mark the positions of the new peaks.

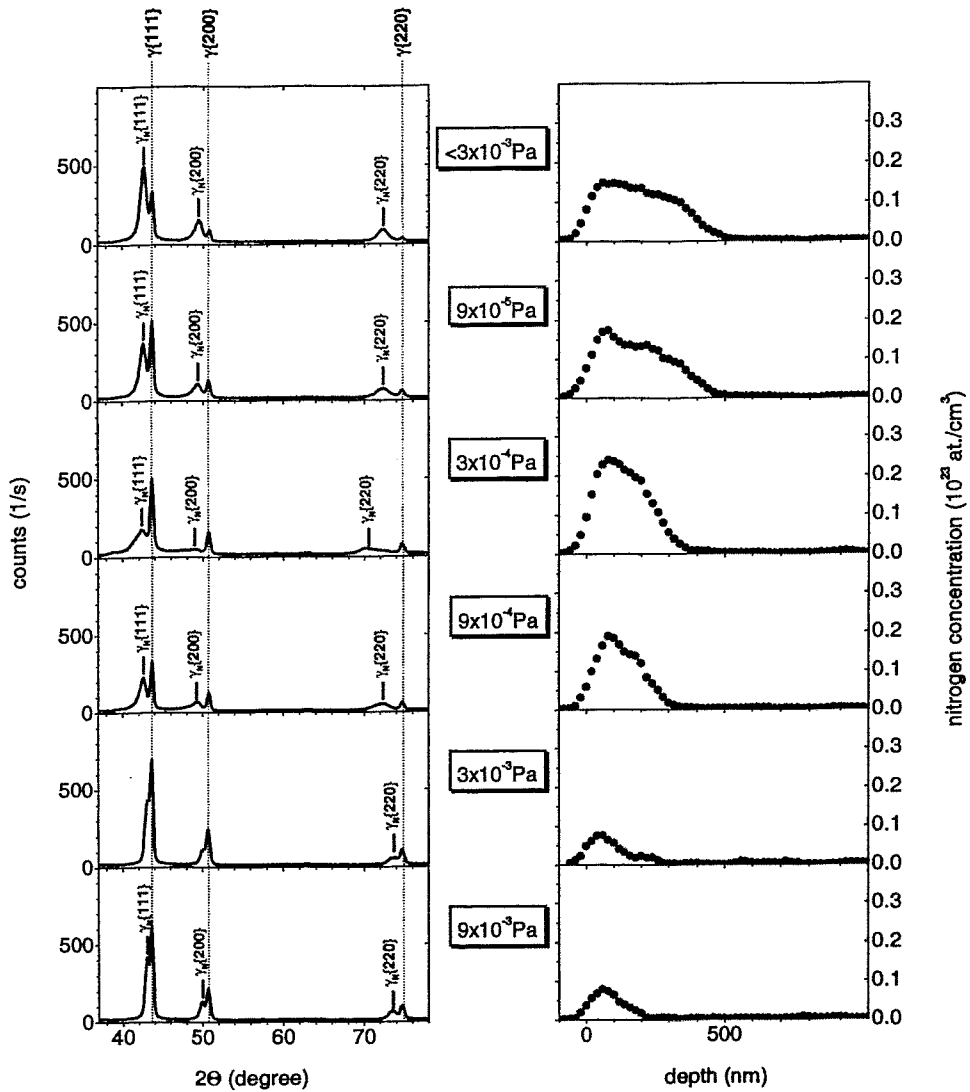


**Figure 4.3:** X-ray diffraction patterns and nitrogen depth profiles of samples ion nitrided at different oxygen partial pressures ranging from  $p(O_2) < 3 \times 10^{-5}$  Pa to  $p(O_2) = 9 \times 10^{-3}$  Pa. Ion nitriding has been performed for 10 min, at 2 keV, 0.2 mA/cm<sup>2</sup>, and a temperature of 320°C. The lines labeled  $\gamma\{111\}$ ,  $\gamma\{200\}$ , and  $\gamma\{220\}$  mark the positions of the peaks of the virgin sample. The additional peaks are labeled  $\gamma_N\{111\}$ ,  $\gamma_N\{200\}$ , and  $\gamma_N\{220\}$ . The vertical bars mark the positions of the new peaks.

sample T (°C)	$\gamma_N\{111\}$	$\gamma_N\{200\}$	$\gamma_N\{220\}$	mean values				$N_{ns}$ ( $10^{21}$ at./ $\text{cm}^3$ )
	$a_N$ (nm)	$a_N$ (nm)	$a_N$ (nm)	$\bar{a}_N$ (nm)	$\Delta a/\bar{a}$ (%)	$\bar{V}_N$ ( $\text{nm}^3$ )	$\Delta V/\bar{V}$ (%)	
280°C	-	-	-	-	-	-	-	5.9
320°C	0.3702	-	0.3829	0.3766	4.9	0.01335	15.3	23.7
360°C	0.3773	-	0.3843	0.3808	6.1	0.01380	19.2	30.1
400°C	0.3774	0.3830	0.3783	0.3796	5.8	0.01367	18.0	31.6
440°C	0.3804	0.3854	0.3796	0.3818	6.4	0.01391	20.1	26.2
480°C	0.3735	0.3788	0.3734	0.3752	4.5	0.01320	14.0	17.3
sample p (Pa)	$\gamma_N\{111\}$	$\gamma_N\{200\}$	$\gamma_N\{220\}$	mean values				$N_{ns}$ ( $10^{21}$ at./ $\text{cm}^3$ )
	$a_N$ (nm)	$a_N$ (nm)	$a_N$ (nm)	$\bar{a}_N$ (nm)	$\Delta a/\bar{a}$ (%)	$\bar{V}_N$ ( $\text{nm}^3$ )	$\Delta V/\bar{V}$ (%)	
$3 \times 10^{-5}$	0.3680	0.3688	0.3692	0.3687	2.7	0.01253	8.2	14.2
$9 \times 10^{-5}$	0.3681	0.3695	0.3692	0.3689	2.8	0.01255	8.4	14.9
$3 \times 10^{-4}$	0.3693	0.3720	0.3771	0.3728	3.9	0.01295	11.8	22.4
$9 \times 10^{-4}$	0.3678	0.3699	0.3699	0.3692	2.9	0.01258	8.6	16.6
$3 \times 10^{-3}$	(*)	(*)	0.3632	0.3632	1.2	0.01198	3.5	4.3
$9 \times 10^{-3}$	0.3634	0.3646	0.3640	0.3640	1.4	0.01206	4.2	5.1

**Table 4.2:** Peak positions of  $\gamma_N$ -peaks, corresponding lattice constants  $a_N$ , mean lattice constant  $\bar{a}_N$ , and mean atomic volume per host atom  $\bar{V}_N$  obtained from x-ray diffraction analysis of samples ion nitrided at different temperatures and different oxygen partial pressures. Additionally listed are the relative variation of the mean lattice constant with respect to the mean lattice constant of the virgin sample  $\Delta a/\bar{a}$  (Equation 4.1), the relative variation of the mean volume per host atom with respect to the mean volume per host atom of the virgin sample  $\Delta V/\bar{V}$  (Equation 4.2), and the nitrogen near surface concentration  $N_{ns}$ ; (-) no  $\gamma_N$ -peaks were detected; (\*) peak positions were not determined as the  $\gamma_N$ -peaks appear on the left shoulder of the corresponding  $\gamma$ -peaks.

### 4.1.3 Discussion

A linear dependence over a wide range of ratios of nitrogen to host atoms, as observed here, is a strong evidence that nitrogen is present in interstitial solid solution. Similar linear dependencies, but with varying coefficients, have also been found by others [158, 160, 159]. As discussed in greater detail further below, the variation of the coefficients can be attributed to stress relaxation.

Does the nitrogen enriched layer consist of a single phase or rather a mixture of phases? Although the x-ray diffraction patterns do not show other peaks than the  $\gamma_N$ -peaks and

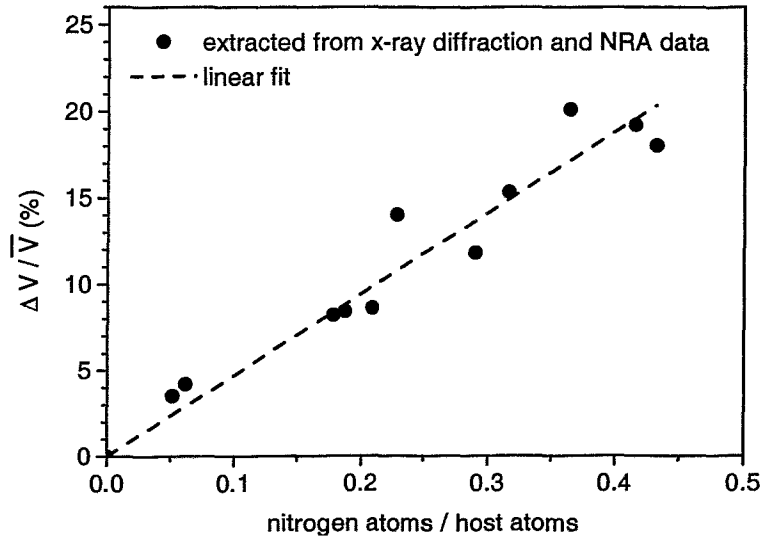


**Figure 4.4:** The relative expansion of the mean volume per host atom  $\Delta V / \bar{V}$  given in % vs. the ratio of nitrogen and host atoms. Every data point corresponds to one sample (refer to Figure 4.2 and Figure 4.3, respectively to Table 4.2). The dashed line represents the linear least square fit given in Equation 4.3.

the  $\gamma$ -peaks, the data do not provide a clear answer to this question. This is due to the fact that x-ray diffraction analysis is sensitive neither to phases with total volume fractions of less than  $\approx 10\%$  nor to small size precipitates [163], as, for example, chromium nitride precipitates which have been observed by many others after nitriding at longer times or higher temperatures [151, 164, 41, 48, 67, 69, 165, 44, 147, 66, 152]. However, from diffusion data of substitutional atoms in austenitic stainless steel [166], it can be estimated that at the temperature and time-regimes applied in the present work chromium nitride precipitation is hindered for kinetic reasons. This estimate is consistent with preliminary isothermal transformation diagrams that have been measured recently by Li et al. [151]. Therefore, we tend to interpret the structural modification induced in the samples in terms of a single austenitic (fcc) phase with nitrogen in interstitial solid solution.

The plausibility of this interpretation is also supported by considering that (i) on the basis of Hägg's rule [167] nitrogen is expected to occupy interstitial (octahedral) sites, (ii) in similar systems it has been found experimentally that nitrogen occupies interstitial (octahedral) sites [168, 169], (iii) extrapolation of higher temperature solubility data [170] to temperatures around  $400^\circ\text{C}$  suggests that austenitic stainless steel is capable to assimilate nitrogen contents exceeding 30 at.%, and (iv) evidences for dual layer structures obtained by x-ray diffraction analysis [148] and conversion electron Mössbauer spectroscopy [75] may be attributed to a carbon enriched layer between the  $\gamma_N$ -layer and the  $\gamma$ -substrate, which was observed already in Ref. [76], respectively to the nitrogen sensitivity of the Néel temperature [171]. As, additional to chromium nitride precipitation at longer nitriding

times or higher temperatures, there are numerous evidences for an attractive interaction between chromium and nitrogen [73, 172, 173, 174], it appears reasonable to assume a single austenitic phase with nitrogen in interstitial solid solution, where nitrogen preferentially occupies interstitial octahedral sites neighboring to chromium atoms.

Finally, the role of stress shall be discussed briefly. A strong biaxial compressive stress is certainly expected for the nitrogen enriched layer as a result of the relatively large lattice mismatch at the interface of the  $\gamma_N$ -layer and the  $\gamma$ -substrate. Recent measurements have shown that the lattice expansion is not only anisotropic with respect to the crystal lattice orientation (an observation – also made by others [35, 75, 68] – for which x-ray elastic constants that differ with the lattice orientation and increase with nitrogen enrichment [171] provide some explanation), but also anisotropic in space, that is, parallel to the layer-substrate interface the lattice expansion is smaller than perpendicular to the layer-substrate interphase [156]. Apparently, stress relaxation preferentially occurs by a lattice expansion perpendicular to the layer interface. The fcc crystal lattice becomes anisotropically distorted which might have caused others [161, 162, 149] to interpret it as a tetragonal phase. Further, there is experimental evidence for an increase of the lattice expansion with the thickness of the nitrogen enriched layer. The two data in Figure 4.4, which most significantly deviate from the linear fit towards higher values of  $\Delta V/\bar{V}$ , have been obtained from the samples with the thickest nitrogen enriched layers (440°C and 480°C). The relatively large lattice expansions [35, 68] have also been observed at thicker layers. Stress relaxation that increases with the distance from the layer interface would qualitatively explain this observation and thus the scattering in the coefficients determined on the basis of Végard's law. The observations made in Ref. [156] are also indicative of stress relaxation by plastic deformation in the nitrogen enriched layer. Such plastic deformation – for the atomic mechanisms by which it occurs Refs. [175, 176, 152] may provide some clues – may be the reason for lamellar structures observed elsewhere [67].

#### 4.1.4 Summary

The structural nature of the nitrogen enriched layer has been investigated comparing lattice expansions (obtained from x-ray diffraction analysis) to nitrogen near surface concentrations (obtained from nuclear reaction analysis). A linear dependence between the variation of the mean volume per host atom  $\Delta V/\bar{V}$ (%) and the ratio of nitrogen to host atoms  $N_{ns}/\bar{V}_N$  according to  $\Delta V/\bar{V}$ (%) =  $47.1 \times N_{ns}/\bar{V}_N$  has been found for a wide range of ratios  $N_{ns}/\bar{V}_N$ . Such a linear dependence is expected according to Végard's law and is a strong evidence that nitrogen is present in interstitial solid solution. Differing coefficients found elsewhere as well as interpretations of the induced modification as a new phase are possibly related to (anisotropic) stress relaxation in the nitrogen enriched layer. From diffusion data of substitutional atoms and from preliminary isothermal transformation diagrams it can be inferred that for the temperature and time-regimes applied in the present work chromium nitride precipitation is hindered for kinetic reasons. Therefore, we interpret the structural modification induced in the samples in terms of a single austenitic phase with an anisotropically distorted fcc crystal lattice that hosts nitrogen in interstitial solid solution. The plausibility of this interpretation is supported and further specified considering that according to



Hägg's rule nitrogen is expected to occupy interstitial octahedral sites and that there are numerous evidences for an attractive interaction between chromium and nitrogen. It thus appears reasonable to assume that nitrogen preferentially occupies interstitial octahedral sites adjacent to chromium atoms.

## 4.2 The diffusion mechanism of nitrogen

### 4.2.1 Introduction

The nitrogen depth profiles typically observed after successful nitriding of austenitic stainless steels have plateau-type shapes, that is, the depth profiles slowly decrease from the surface towards the bulk and exhibit a rather sharp leading edge. Such profiles are not consistent with "simple" diffusion (Equation 2.7). Additionally, estimated nitrogen diffusivities [34, 73, 125] exceed nitrogen diffusivities obtained elsewhere [177, 178] by up to five orders of magnitude. Two diffusion mechanisms have been proposed in order to explain these peculiarities.

- A trapping mechanism has been suggested by Williamson et al. [179, 73].
- Szasz et al. [36] and Melitis et al. [180] proposed a defect-mediated mechanism.

In this section, experiments that test for the proposed mechanisms are presented and discussed. Comparison of nitrogen depth profiles obtained from nuclear reaction analysis and slow positron implantation spectroscopy data provide information on the role of defect-mediated diffusion. In order to reveal information on trapping, a set of samples has been subsequently ion nitrided with  $^{14}\text{N}$  and  $^{15}\text{N}$ . Nitrogen depth profiles obtained from nuclear reaction analysis are presented and qualitatively discussed. The qualitative trapping model presented in Ref. [179, 73] is refined and put on a more quantitative basis. Quantitative model results are compared to the experimental nitrogen depth profiles.

### 4.2.2 Experimental results

#### A defect-mediated mechanism

Szasz et al. [36] and Melitis et al. [180] suggested that the nitrogen diffusion is promoted by a vacancy-nitrogen pair diffusion mechanism with the vacancies generated by the ion bombardment. In order to get information about the influence of defects as, for example, vacancies on the diffusional transport, a series of samples has been ion nitrided at the same ion energy, current density and temperature, but different times. The samples were analyzed by nuclear reaction analysis (NRA) using the  $^{14}\text{N}(d, \alpha_1)^{12}\text{C}$  reaction at an incident deuterium energy of 1.4 MeV (refer to Section 3.3) and by slow positron implantation spectroscopy (SPIS), also known as positron annihilation spectroscopy<sup>1</sup>. SPIS is based on the motion of positron-electron pairs prior to annihilation, which causes a Doppler broadening of the photopeak in the measured energy spectrum of the annihilation photons. This Doppler broadening is characterized by the lineshape parameter  $S$ , being the ratio of counts in the central region of the photopeak to the total number of counts in the peak. The  $S$ -parameter is sensitive to changes of the defect structure and the defect concentration. Depth resolved information has been obtained by implanting positrons of

<sup>1</sup>SPIS has been carried out at the University of East Anglia in Norwich, GB. Thanks to Dr. G. Brauer and W. Anwand for performing the measurements and evaluating the data, and to Prof. P.G. Coleman for making his SPIS setup available.

predetermined energies stepwise from 200 eV up to a maximum energy of 33 keV. The latter energy corresponds to a positron implantation depth (maximum detection depth) of about 1500 nm.

Figure 4.5 shows the nitrogen depth profiles obtained by NRA, and the  $S$ -parameter versus the mean positron penetration depth obtained by SPIS. The thickness of the nitrated layer increases with nitriding time, the nitrogen depth profiles exhibit the typical leading edge, and the nitrogen near surface concentration saturates at about  $0.35 \times 10^{23}$  at./cm<sup>3</sup>. The corresponding SPIS data show that close to the surface the  $S$ -parameter decreases fast, which is typical for metals [125]. With increasing depth, the  $S$ -parameter exhibits a kind of a plateau before it tends towards the bulk value (dashed lines). This plateau broadens with increasing nitriding time.

Layer thicknesses of the nitrogen enriched layers and the defect enriched layers, evaluated from these NRA and SPIS data, respectively, are shown in Figure 4.6. The nitrogen enriched layer thicknesses were taken from the surface to the depth at which the nitrogen concentration amounts to  $0.1 \times 10^{23}$  at./cm<sup>2</sup>. The defect enriched layer thicknesses have been determined by applying the fitting routine VEPFIT [181] to the SPIS data (fits are also shown in Figure 4.5). The resulting thicknesses of the defect layer are smaller than those of the nitrated layers. This finding, which indicates that defects do not accelerate the nitrogen diffusion, is in agreement with another investigation by Williamson et al. in which samples have been ion nitrated at constant temperature, current density, ion energy, and time, but at different N<sub>2</sub>/Ar gas mixtures [73]. If the diffusion would be accelerated by defects, the combined N<sub>2</sub>/Ar bombardment should lead to thicker layers compared to pure nitrogen treatment, since argon bombardment is expected to create more defects than nitrogen bombardment. In all cases, Williamson found the  $\gamma_N$  layer, but contradictory to a defect-mediated diffusion mechanism, the layer thickness was largest when pure nitrogen was used. Therefore, we conclude that a defect-mediated diffusion mechanism can not be sustained.

### A trapping mechanism

Williamson et al. [179, 73] proposed a qualitative diffusion model. According to this model, nitrogen gets trapped at chromium sites resulting in the generation of the highly nitrogen enriched layer with a nitrogen concentration comparable to or even higher than the chromium concentration. When all the trap sites become occupied, additional incoming nitrogen diffuses quickly through the saturated highly nitrogen enriched layer to reach the leading edge of the nitrogen depth profile, where unoccupied trap sites are available. This mechanism indeed predicts nitrogen profiles with a plateau and a relative sharp leading edge.

In order to test this qualitative model, samples have been ion nitrated first with the <sup>15</sup>N isotope and subsequently with the <sup>14</sup>N isotope and vice versa. The resulting <sup>14</sup>N and <sup>15</sup>N depth profiles were measured by NRA at an incident deuteron energy of 1.2 MeV using the reactions <sup>14</sup>N(d,  $\alpha_1$ )<sup>12</sup>C and <sup>15</sup>N(d,  $\alpha_0$ )<sup>13</sup>C, respectively (refer to Section 3.3). An example, showing typical depth profiles, is given in Figure 4.7. According to the qualitative model of Williamson et al. [179, 73] the post-implanted isotope would be expected to be

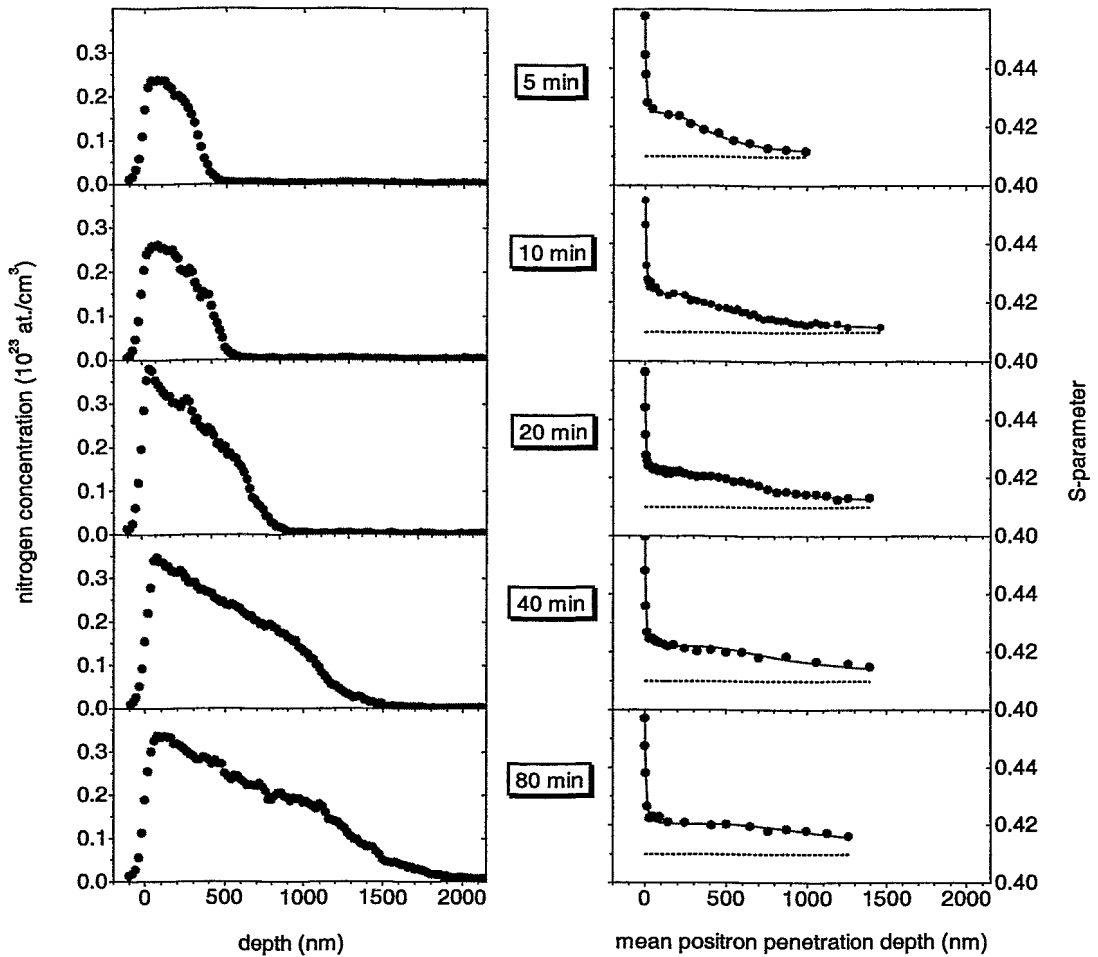


**Figure 4.5:** Nitrogen depth profiles (left column) and the  $S$ -parameter versus mean positron penetration depth (right column) of samples that have been ion nitrided for different times ranging from 5 min to 80 min. Ion nitriding has been performed at  $E_{\text{in}} = 1.2$  keV,  $\rho = 0.5$  mA/cm<sup>2</sup>, and  $T = 400^\circ\text{C}$ . In the right column, the full circles represent the experimental data, the full lines represent the fit results obtained using the VEPFIT routine [181], and the dashed lines represent the bulk value of the  $S$ -parameter.

located closer to the leading edge than the pre-implanted isotope. This feature is *not* observed experimentally. Thus, the model can not be sustained. However, the profiles exhibit intriguing similarities to what would be expected from trapping, if the trap is shallow enough to allow for detrapping [111]: (i) the postimplanted isotope shows an error functional depth profile, (ii) the total nitrogen depth profile exhibits a leading edge at

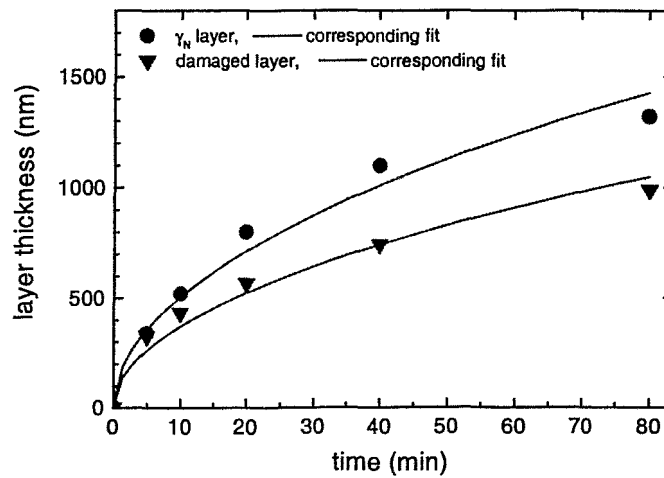


Figure 4.6: Layer thickness versus time as measured by NRA (nitrogen enriched layer) and as measured by SPIS (damaged layer). The evolution of the layer thicknesses is fitted assuming a  $\sqrt{t}$ -dependence.

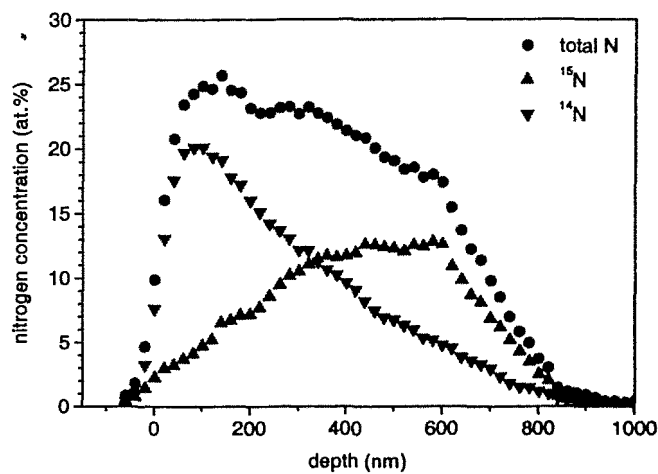


Figure 4.7:  $^{14}\text{N}$  and  $^{15}\text{N}$  depth profiles measured by NRA after ion nitriding a sample for  $t = 5$  min with  $^{15}\text{N}$  and subsequently for  $t = 5$  min with  $^{14}\text{N}$  at  $T = 400^\circ\text{C}$   $E_{\text{in}} = 1.2$  keV, and  $\rho = 1.0$  mA/cm $^2$ .

the depth where its concentration amounts approximately to the concentration of the trap sites, (iii) from the surface to that leading edge the total nitrogen depth profile decreases error functionally with a concentration offset equal to the trap site concentration.

### 4.2.3 Modeling results

Encouraged by the above qualitative analogies, the qualitative trapping model [179, 73] is refined by including detrapping of nitrogen and put on a more quantitative basis in order to allow for quantitative predictions. The baseline of the modeling approach developed by Möller et al. [113] and Myers et al. [109] is picked up (refer to Section 2.4). It is assumed that nitrogen diffuses via diffusion sites under the influence of one kind of immobile trap sites. Diffusional transport of substitutional elements is neglected, based on low diffusivities of Fe, Cr, and Ni at 400 °C [166] and lack of evidence of nitride precipitation (refer to Section 4.2). The trap sites are represented by chromium atoms in the static fcc lattice formed by the host elements of the austenitic stainless steel. The assumptions listed in Section 2.3 are made. Additionally, it is assumed that nitrogen gets implanted on diffusion sites.  $^{14}\text{N}$  and  $^{15}\text{N}$  compete for the same trap sites where they get trapped following first order kinetics, that is, their individual trapping rate is proportional to the product of their respective concentration and the concentration of free trap sites. Both,  $^{14}\text{N}$  and  $^{15}\text{N}$ , can be thermally detrapped from trap sites to diffusion sites following identical kinetics. Then, the transport of the two isotopes can be described by the following set of four coupled diffusion and trapping/detrapping equations in connection with a source term  $S(x, t)$ :

$$\frac{\partial}{\partial t} {}^{14}\text{N}_d(x, t) = D \frac{\partial^2}{\partial x^2} {}^{14}\text{N}_d(x, t) + {}^{14}\text{S}(x, t) - \frac{\partial}{\partial t} {}^{14}\text{N}_t(x, t) \quad (4.4)$$

$$\frac{\partial}{\partial t} {}^{14}\text{N}_t(x, t) = k_{d \rightarrow t} {}^{14}\text{N}_d(x, t) \times \left( 1 - \frac{{}^{14}\text{N}_t(x, t)}{H_t(x, t)} - \frac{{}^{15}\text{N}_t(x, t)}{H_t(x, t)} \right) - k_{t \rightarrow d} {}^{14}\text{N}_t(x, t) \quad (4.5)$$

and two similar equations where  $^{14}\text{N}_d$ ,  $^{14}\text{N}_t$ ,  $^{14}\text{S}$ , and  $^{15}\text{N}_t$  are replaced by  $^{15}\text{N}_d$ ,  $^{15}\text{N}_t$ ,  $^{15}\text{S}$ , and  $^{14}\text{N}_t$ , respectively. Symbols in this set of equations have the following meaning:  $x$  is the depth,  $t$  the time,  $D$  the diffusion coefficient of nitrogen (on diffusion sites);  $^{14}\text{N}_d$  is the concentration of  $^{14}\text{N}$  on diffusion sites,  $^{14}\text{N}_t$  the concentration of  $^{14}\text{N}$  on trap sites. Analogously,  $^{15}\text{N}_d$  is the concentration of  $^{15}\text{N}$  on diffusion sites and  $^{15}\text{N}_t$  the concentration of  $^{15}\text{N}$  on trap sites.  $^{14}\text{S}$  and  $^{15}\text{S}$  are the individual source terms of the respective isotopes.  $H_t$  is the concentration of trap sites in the matrix, and  $k_{t \rightarrow d}$  and  $k_{d \rightarrow t}$  are trapping and detrapping coefficients, respectively. For diffusion-controlled trapping and detrapping [110]  $k_{d \rightarrow t}$  is proportional to  $D = D_0 \exp(-E_d/kT)$  and  $k_{t \rightarrow d}$  is proportional to  $D_0 \exp(-E_{t \rightarrow d}/kT)$ , where  $D_0$  is the pre-exponential factor of diffusion,  $k$  is the Boltzmann constant, and  $E_d$  and  $E_{t \rightarrow d}$  are the diffusion and detrapping activation energies, that is, the difference in potential energy between the diffusion saddle point and a diffusion site, respectively a trap site (refer to Section 2.3).

The solution of this set of diffusion and trapping/detrapping equations that includes source terms requires the use of numerical methods. For the given problem the computer program PIDAT, which is described in more detail in Ref. [115], has been employed. The program has been slightly modified to account for different isotopes<sup>2</sup>. The initial  $^{14}\text{N}$  and  $^{15}\text{N}$  concentrations were assumed to be zero throughout the sample. The boundary conditions assumed were (i) an outgoing nitrogen flux that is proportional to the square of

<sup>2</sup>Many thanks to Prof. W. Möller for the modification and an introduction to the program.

the surface nitrogen concentration and (ii) zero nitrogen concentration at the back surface ( $x = \infty$ ). The source terms for the two nitrogen isotopes have been set as  $S(x, t) = j_{in}(t) f_R(x)$ , where  $j_{in}(t)$  is the incoming nitrogen flux density and  $f_R(x)$  is the projected range distribution of nitrogen<sup>3</sup>, according to the experimental conditions of the  $^{14}\text{N}/^{15}\text{N}$  treatment that are given in the caption of Figure 4.7. Prefactors of  $k_{d \rightarrow t}$  and  $k_{t \rightarrow d}$  have little influence and were chosen according to the definitions given in Ref. [109]. Calculated depth profiles, assuming a diffusion pre-exponential factor  $D_0 = 10^{-3} \text{ cm}^2/\text{s}$ , a diffusion activation energy of  $E_d = 1.1 \text{ eV}$ , and a detrapping activation energy  $E_{t \rightarrow d} = 1.45 \text{ eV}$ , are shown in Figure 4.8 together with the experimental  $^{14}\text{N}/^{15}\text{N}$  depth profiles. Calculated and experimental depth profiles show good agreement suggesting that trapping and detrapping occurs<sup>4</sup>.

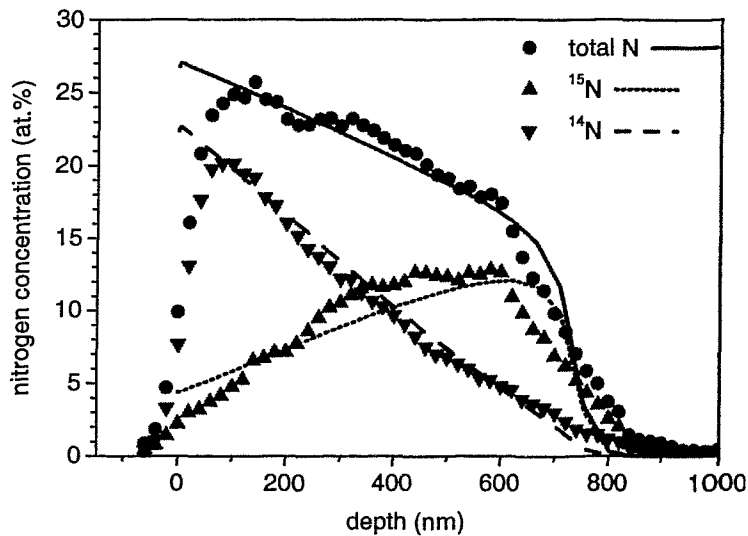


**Figure 4.8:**  $^{14}\text{N}$ ,  $^{15}\text{N}$ , and total N depth profiles as measured by NRA (dots) and  $^{14}\text{N}$ ,  $^{15}\text{N}$ , and total N depth profiles as calculated by means of PIDAT (lines). For modification parameters refer to Section 2.4.

#### 4.2.4 Discussion

The primary purpose of the above comparison of experimental results and modeling results is to demonstrate that both the total nitrogen depth profiles and the  $^{14}\text{N}/^{15}\text{N}$  depth profiles are consistent with a diffusion model that considers trapping and detrapping of nitrogen

<sup>3</sup>the range distribution has been approximated by a gaussian distribution, resembling the projected range distribution estimated by SRIM simulations.

<sup>4</sup>Deviations close to the surface and near the leading edge are influenced by the depth resolution of NRA (refer to Section 3.3).

at, respectively from, trap sites that are represented by chromium atoms. Additionally, the model provides an explanation for the large scatter of nitrogen diffusion data. The relatively low diffusion coefficients in Ref. [177, 178] have been extracted from nitrogen depth profiles with maximum nitrogen concentrations lower than the trap concentration. At such concentrations the extracted apparent diffusion coefficient is dominated by the escape frequency from trap sites and, thus, by the detrapping activation energy rather than by the diffusion activation energy [112]. The model is thus also qualitatively consistent with an annealing experiment [182], which indicated a decreasing diffusion coefficient as the nitrogen concentration decreased.

The presented model assumes that chromium atoms represent trap sites for nitrogen. This assumption is consistent with our interpretation of the structural nature of the nitrogen enriched layer and plausible both from a thermodynamical and from a phenomenological point of view, since chromium-nitrides have higher stability versus either the iron-nitrides or nickel-nitrides [73] and since at higher nitriding temperatures and thus higher chromium mobilities the formation of chromium-nitride precipitates is observed. Additionally, extended x-ray absorption fine structure spectroscopy indicated that interstitial sites adjacent to chromium are favorable hosts for nitrogen atoms [172]. Furthermore, a strong Cr-N interaction has been shown by neutron spectroscopy [173] and by internal friction [174] in similar systems (refer to Section 4.1.3).

It should be mentioned, however, that the results of the calculation can be fitted quite closely to the experimental data, assuming various combinations of reasonable diffusion, trapping, and loss parameters. Thus, the above values have to be considered as preliminary. Limits may be given already for the detrapping activation energy.  $E_{t \rightarrow d}$  is sensitive to the steepness of the depth profiles at the leading edge [111]. From other depth profiling techniques, such as Auger electron depth profiling [62] and secondary ion mass spectroscopy [183], there is evidence of significantly sharper leading edge profiles than measured here by means of nuclear reaction analysis<sup>5</sup>. Thus, the value of 1.45 eV may be considered as a lower limit. An upper limit can be estimated from the assumption that local thermal equilibrium [109] exists between nitrogen on diffusion sites and nitrogen on trap sites. Considering reasonable pre-exponential factors, at 400°C this assumption is not fulfilled at detrapping activation energies above 2.5 eV. However, if exchange [184] between nitrogen on diffusional sites and nitrogen on trap sites without fully breaking the Cr-N bond occurs, the detrapping activation energy may even be higher than 2.5 eV.

#### 4.2.5 Summary

The diffusion mechanism of nitrogen has been investigated by experiments that test for a defect-mediated mechanism and a trapping mechanism, respectively. The experiments did not provide evidence for a defect-mediated diffusion mechanism. While at first glance, a trapping mechanism is also not sustained, closer qualitative considerations, as well as quantitative modeling results, indicate that trapping occurs. The trapping mechanism is

<sup>5</sup>Again, it should be noted that the depth resolution of NRA increases significantly with increasing depth (refer to Section 3.3). Further, lateral inhomogeneities, as observed by others [75, 67], would make the leading edge seem less sharp than it actually is.



consistent with our interpretation of the structural nature of the nitrogen enriched layer and plausible both from a thermodynamical and from a phenomenological point of view. Calculated depth profiles, assuming a diffusion pre-exponential factor  $D_0 = 10^{-3} \text{ cm}^2/\text{s}$ , a diffusion activation energy of  $E_d = 1.1 \text{ eV}$ , and a detrapping activation energy  $E_{t \rightarrow d} = 1.45 \text{ eV}$  show good agreement with experimental depth profiles.

## 4.3 The role of potential incorporation and release mechanisms

### 4.3.1 Introduction

The identification and characterization of the relevant incorporation and release mechanisms is a precondition for the qualitative understanding and for the quantitative description of the nitrogen transport. While gas nitriding proceeds by thermochemical mechanisms [2, 4, 86, 89], ballistic mechanisms that are associated with ion bombardment, for example, ion implantation and sputtering, apparently become more and more important via plasma nitriding and remote plasma nitriding towards ion nitriding [84, 185, 88].

In this section, experiments utilizing real-time elastic recoil detection analysis are presented and discussed. These experiments are suited to test for the role of potentially relevant incorporation and release mechanisms (refer to Section 2.4), in particular for the role of absorption, recoil implantation, and desorption. Normally, they have been performed at a low oxygen partial pressure such that any reoxidation from the residual gas can be neglected. Furthermore, an approach to model the nitrogen retention during ion nitriding in terms of implantation and sputtering is presented. Modeling results are compared with additional experimental results obtained from a combined analysis using real-time elastic recoil detection analysis and nuclear reaction analysis.

### 4.3.2 Experimental results

#### Absorption and recoil implantation

Absorption is a transport mechanism that proceeds via a chain of mechanisms including arrival and adsorption at the surface, dissociation, chemisorption, and diffusion [78]. Recoil implantation is a transport mechanism that proceeds via momentum transfer between incident energetic ions and atoms located close to the surface, where the latter get implanted (recoiled) deeper into the substrate. In ion nitriding, by its definition (refer to Chapter 1), neither absorption nor recoil implantation is the predominant incorporation mechanism. However, due to the significant nitrogen partial pressure that is usually present in the ion nitriding chamber, relatively large amounts of thermal molecular nitrogen arrive at the surface and nitrogen may be adsorbed on the surface. In order to explore if part of the thermal nitrogen flux gets absorbed or adsorbed nitrogen gets recoiled into the substrate the following experiment has been performed. A preoxidised sample has been exposed to argon ion bombardment ( $E_{in} = 1 \text{ keV}$ ,  $\rho = 0.1 \text{ mA/cm}^2$ ) while an elevated nitrogen partial pressure ( $p(N_2) = 1 \times 10^{-2} \text{ Pa}$ ) was present in the ion nitriding chamber. After 40 min the argon ion bombardment has been stopped. During this treatment the sample temperature was ramped from  $T = 380^\circ\text{C}$  to  $T = 440^\circ\text{C}$ . After stopping the argon ion bombardment the sample has been held at  $T = 440^\circ\text{C}$ . 50 min after the argon ion bombardment has been started, the oxygen partial pressure has been elevated from initially  $p(O_2) < 3 \times 10^{-5} \text{ Pa}$  to  $p(O_2) > 1 \times 10^{-2} \text{ Pa}$ .

Figure 4.9 shows the time resolved depth profiles of oxygen and nitrogen and the corresponding areal densities measured by real-time ERDA during this treatment. Let us first

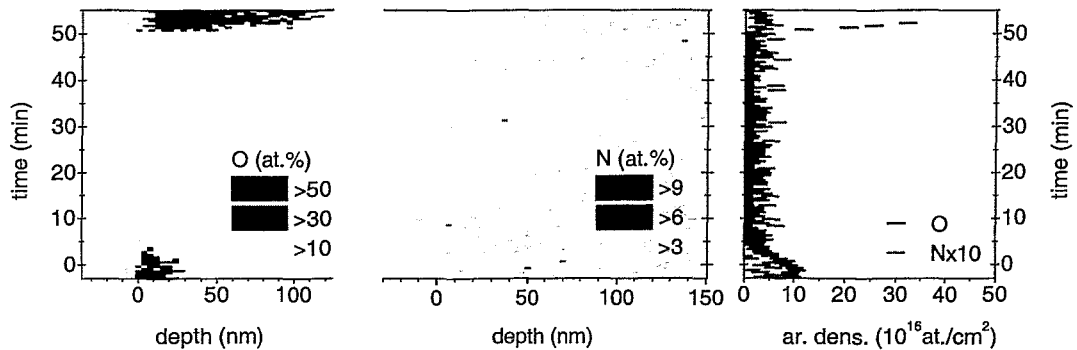


**Figure 4.9:** Time resolved depth profiles of oxygen (left) and nitrogen (center) and the corresponding evolutions of oxygen and nitrogen areal densities (right), as obtained from real-time ERDA before, during, and after argon ion bombardment of a preoxidised austenitic stainless steel sample. Argon ion bombardment ( $E_{in} = 1.0$  keV,  $\rho = 0.1$  mA/cm<sup>2</sup>) starts at time  $t = 0$  min and stops at time  $t = 40$  min. The sample temperature was ramped from  $T = 380^\circ\text{C}$  at time  $t = 0$  min to  $T = 440^\circ\text{C}$  at time  $t = 55$  min. Throughout the treatment the partial pressure of nitrogen was held at  $p(N_2) = 1 \times 10^{-2}$  Pa. At time  $t = 50$  min the oxygen partial pressure has been elevated from initially  $p(O_2) < 3 \times 10^{-5}$  Pa to  $p(O_2) > 1 \times 10^{-2}$  Pa.

consider the evolution of the oxygen areal density and the evolution of the corresponding time resolved depth profile of oxygen. The initial oxygen areal density amounts to  $O_{ret} \approx 10 \times 10^{16}$  at./cm<sup>2</sup> corresponding to a stoichiometric Cr<sub>2</sub>O<sub>3</sub>-layer of  $\approx 16$  nm thickness<sup>6</sup>. It takes about 5 min of argon ion bombardment to remove this layer, corresponding to an oxygen removal rate of approximately  $3.3 \times 10^{14}$  at./cm<sup>2</sup>s. This oxygen removal rate corresponds to a partial sputtering yield of oxygen of about 0.53 oxygen atoms per argon atom. This experimental partial sputtering yield is in good agreement with the yield estimated by a SRIM simulation (0.57 oxygen atoms per argon atom assuming a reasonable surface binding energy  $E_s(O) = 6.52$  eV; refer to Chapter 4.5). Further, the experiment reveals that the oxidation kinetics depend dramatically on the oxygen partial pressure. While at the low oxygen partial pressure no significant oxidation is observed even after the argon ion bombardment is stopped ( $t = 40 - 50$  min), at the high oxygen partial pressure introduced at  $t = 50$  min, oxidation to an oxygen areal density  $O_{ret} > 30 \times 10^{16}$  at./cm<sup>2</sup> is observed within less than 3 min.

<sup>6</sup>We assume all oxygen to be present near the surface in form of a stoichiometric and lateral homogenous Cr<sub>2</sub>O<sub>3</sub>-layer with a density of 5.21 g/cm<sup>3</sup>. With this assumption  $1 \times 10^{16}$  at./cm<sup>2</sup> correspond to 1.615 nm or 6.39 ML Cr<sub>2</sub>O<sub>3</sub> (refer to Chapter 4.5).

Now, let us consider the evolution of the nitrogen areal density  $N_{\text{ret}}$  and the time resolved depth profile of nitrogen  $N(x, t)$ . Throughout the entire treatment, neither  $N_{\text{ret}}$  nor  $N(x, t)$  show any significant change. Both stay constant at a low level that corresponds to the natural abundance of nitrogen in AISI 316. This is a strong evidence that neither absorption nor recoil implantation are a relevant mechanism for the incorporation of nitrogen.

### Desorption

Desorption of nitrogen from the bulk into the gas atmosphere is a transport mechanism that, in principle, may contribute to the release of nitrogen during ion nitriding. In order to explore if it actually contributes, a virgin sample has been ion nitrided for a short time at a low oxygen partial pressure, such that the leading edge of the nitrogen depth profile did not exceed the maximum detection depth of real-time ERDA. After stopping the nitrogen ion bombardment the sample was held at the same temperature for a couple of minutes (for processing parameters refer to the caption of Figure 4.10).

Figure 4.10 shows the time resolved depth profiles of oxygen and nitrogen and the corresponding areal densities during this treatment. The surface oxide layer is essentially

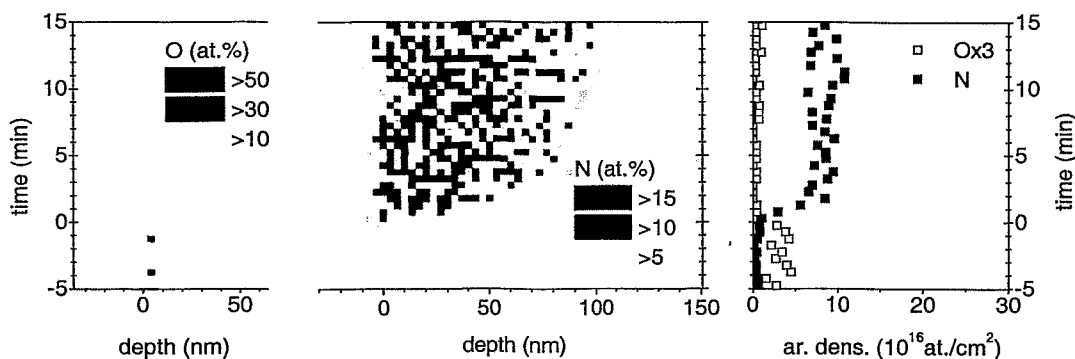


**Figure 4.10:** Time resolved depth profiles of oxygen (left) and nitrogen (center) and corresponding evolutions of oxygen and nitrogen areal densities (right), as obtained from real-time ERDA before and during ion nitriding at  $E_{\text{in}} = 1.0$  keV,  $\rho = 0.2$  mA/cm<sup>2</sup>,  $T = 320^\circ\text{C}$ , and  $p(\text{O}_2) < 3 \times 10^{-5}$  Pa. Nitrogen ion bombardment starts at  $t = 0$  min and stops at  $t = 2$  min.

removed after about 30 s of nitrogen ion bombardment. After two minutes of nitrogen ion bombardment, the amount of retained nitrogen amount to  $N_{\text{ret}} \approx 8 \times 10^{16}$  at./cm<sup>2</sup>. During the subsequent period of time in which the sample is held at the processing temperature and the low oxygen partial pressure without any ion bombardment, the oxygen areal density shows no significant increase. A slight broadening of the nitrogen depth profile, but no significant reduction of the nitrogen areal density is observed. This is a strong evidence that desorption is not a relevant mechanism for the release of nitrogen.

### 4.3.3 Modeling results

From the results presented above, there is no evidence for incorporation of nitrogen by absorption nor for release of nitrogen by desorption. Thus, an approach to model the incorporation and loss of nitrogen in terms of purely collisional mechanisms is presented and compared to experimental data. It is assumed that no surface oxide layer is present and that spontaneous emission does not occur. For simplicity, backscattering is neglected. Then, the nitrogen retention rate  $j_{\text{ret}}$  is given by the difference of the incident flux of energetic nitrogen  $j_{\text{in}}$  and the flux of sputtered nitrogen  $j_{\text{sp}}$  (refer to Section 2.4)

$$j_{\text{ret}}(t) = j_{\text{in}}(t) - j_{\text{sp}}(t). \quad (4.6)$$

In general, the term  $j_{\text{sp}}(t)$  depends on  $j_{\text{in}}(t)$  according to

$$j_{\text{sp}}(t) = j_{\text{in}}(t) \int_{E_{\text{min}}}^{E_{\text{max}}} f(E, t) SY_{\text{N}}(N_{\text{ns}}(t), E(t)) dE, \quad (4.7)$$

where  $f(E, t)$  denotes the ion energy distribution with the minimum ion energy  $E_{\text{min}}$  and the maximum ion energy  $E_{\text{max}}$ , and  $SY_{\text{N}}(N_{\text{ns}}(t), E(t))$  denotes the partial sputtering yield of nitrogen that depends on the nitrogen near surface concentration  $N_{\text{ns}}(t)$ . It follows

$$j_{\text{ret}}(t) = j_{\text{in}}(t) - j_{\text{in}}(t) \int_{E_{\text{min}}}^{E_{\text{max}}} f(E, t) SY_{\text{N}}(N_{\text{ns}}(t), E(t)) dE, \quad (4.8)$$

and

$$N_{\text{ret}}(t) = \int_0^t j_{\text{in}}(t) dt - \int_0^t j_{\text{in}}(t) \int_{E_{\text{min}}}^{E_{\text{max}}} f(E, t) SY_{\text{N}}(N_{\text{ns}}(t), E(t)) dE dt. \quad (4.9)$$

for the nitrogen retention rate and the amount of retained nitrogen, respectively.

For all experiments, the incident flux of energetic nitrogen  $j_{\text{in}}(t)$  has been constant in time. By extracting  $j_{\text{in}}$  from the processing parameters (ion current density and the ratio of  $\text{N}_2^+ : \text{N}^+$ ; refer to Section 3.2) and estimating  $SY_{\text{N}}(N_{\text{ns}}(t), E(t))$  by a TRIDYN simulation<sup>7</sup> our approach results in

$$j_{\text{ret}}(t) = j_{\text{in}}(1 - 2.8N_{\text{ns}}(t)) \quad (4.10)$$

and

$$N_{\text{ret}}(t) = j_{\text{in}} t \left( 1 - 2.8 \int_0^t N_{\text{ns}}(t) dt \right) \quad (4.11)$$

for the nitrogen retention rate and the amount of retained nitrogen, respectively.

In order to test this prediction, a series of samples has been ion nitrided at identical processing parameters with exception of the current density, which has been changed systematically from  $\rho = 0.01 \text{ mA/cm}^2$  up to  $\rho = 0.8 \text{ mA/cm}^2$ . Before starting the nitrogen

<sup>7</sup> $SY_{\text{N}}(N_{\text{ns}}(t), E(t))$  has been estimated by plotting the partial sputtering yield of nitrogen (Figure 2.2c) versus the near surface concentration of nitrogen (Figure 2.2d). The results of two simulations, one for the full ion energy and one for the half energy, were superposed by their respective weights (refer to Section 3.2) and resulted in an almost linear dependence  $SY_{\text{N}}(N_{\text{ns}}(t), E(t)) = 2.8N_{\text{ns}}$ .

ion bombardment all samples were exposed to argon ion bombardment in order to remove the native surface oxide layer. Then, ion nitriding was performed for 15 min at an ion energy  $E_{in} = 1$  keV, a substrate temperature  $T = 400^\circ\text{C}$ , and an oxygen partial pressure  $p(O_2) < 3 \times 10^{-5}$  Pa. Real-time ERDA has been started 3 min before starting the nitrogen ion bombardment.

For the lowest and the highest current density, Figure 4.11 shows the time resolved

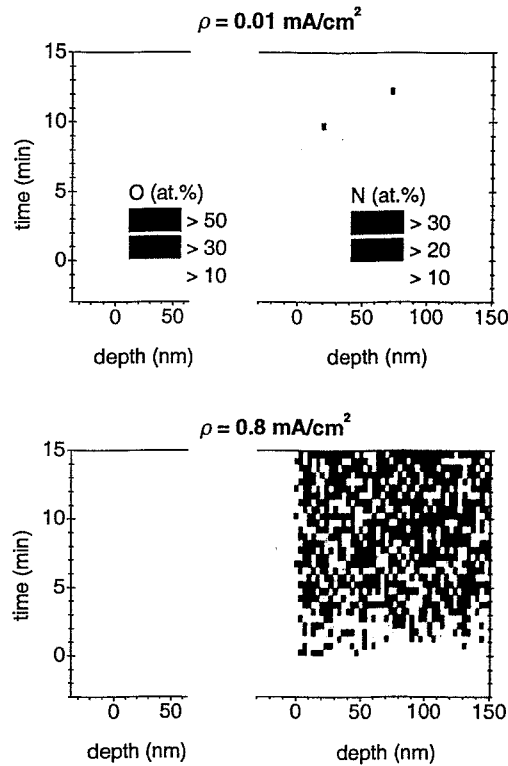


**Figure 4.11:** Time resolved depth profiles of oxygen (left) and nitrogen (right), as obtained from real-time ERDA during ion nitriding of austenitic stainless steel at a low current densities ( $\rho = 0.01 \text{ mA/cm}^2$ ) and a high current density ( $\rho = 0.8 \text{ mA/cm}^2$ ). Ion nitriding at  $E_{in} = 1.0$  keV,  $T = 400^\circ\text{C}$ , and  $p(O_2) < 3 \times 10^{-5}$  Pa starts at time  $t = 0$  min.

depth profiles of oxygen and nitrogen measured by real-time ERDA during this treatment. At  $\rho = 0.01 \text{ mA/cm}^2$  the nitrogen depth profile does not arrive at the maximum detection depth throughout the 15 min lasting treatment while it does at  $0.8 \text{ mA/cm}^2$  – already after one minute – and at all intermediate current densities that are not shown. Note that at all current densities  $\rho$ , no significant amount of oxygen has been detected either immediately before or during the nitrogen ion bombardment. Figure 4.12 shows the evolution of the

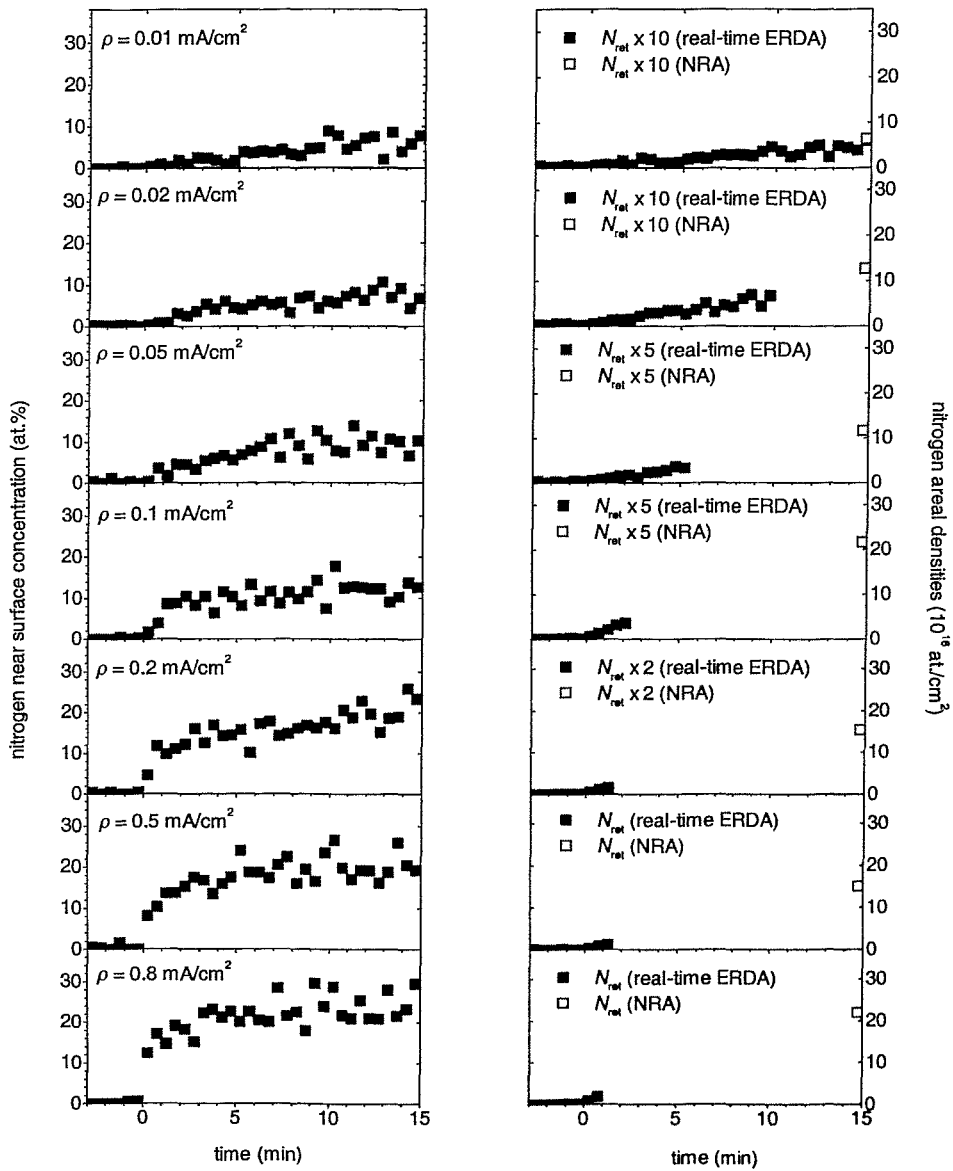


**Figure 4.12:** Evolution of the nitrogen near surface concentrations and the nitrogen areal densities at the given different current densities  $\rho$  obtained from real-time ERDA (solid squares) during ion nitriding of austenitic stainless steel and from NRA (open squares) after ion nitriding. Ion nitriding at  $E_{in} = 1.0$  keV,  $T = 400^\circ\text{C}$ , and  $p(O_2) < 3 \times 10^{-5}$  Pa starts at time  $t = 0$  min.

nitrogen near surface concentrations  $N_{ns}(t)$  and the evolution of the nitrogen areal densities  $N_{ret}(t)$ . For most of the current densities the latter could only be measured for a short interval of time due to the finite detection depth of real-time ERDA. Additionally shown are nitrogen areal densities  $N_{ret}$  measured ex situ by NRA. Since we have found that there is no significant nitrogen loss after stopping the ion nitriding treatment, it can be assumed that the latter correspond to the amount of retained nitrogen immediately before stopping the ion nitriding treatment. Due to relatively poor counting statistics, the measured nitrogen near surface concentration  $N_{ns}(t)$  is subject to significant errors. Thus, the experimental check will be restricted to the amount of nitrogen that is predicted to be retained after 15 min. Equation 4.11 then simplifies to

$$N_{ret}(t) = j_{in} t (1 - 2.8\overline{N_{ns}}), \quad (4.12)$$

where  $\overline{N_{ns}}$  denotes the mean nitrogen near surface concentration measured during the 15 min lasting ion nitriding treatment. The values that result for the different current densities are listed in Table 4.3. The predicted amount of retained nitrogen is in average

$\rho$ (mA/cm <sup>2</sup> )	$j_{in}$ (10 <sup>15</sup> at./cm <sup>2</sup> s)	$\overline{N_{ns}}$ (at.%)	predicted $N_{ret}$ (10 <sup>16</sup> at./cm <sup>2</sup> )	measured $N_{ret}$ (10 <sup>16</sup> at./cm <sup>2</sup> )
0.01	0.09	4.0	7.5	6.4
0.02	0.19	5.3	14.4	12.8
0.05	0.47	7.5	33.3	23.4
0.1	0.94	10.0	60.7	43.5
0.2	1.87	15.2	96.8	76.8
0.5	4.68	18.1	207.8	151.0
0.8	7.49	21.9	260.7	219.8

**Table 4.3:** Values related to the modeling approach for incorporation and release.  $\rho$  denotes the current density,  $j_{in}$  the incident flux of energetic nitrogen atoms,  $\overline{N_{ns}}$  the mean nitrogen near surface concentration measured by real-time ERDA, and  $N_{ret}$  the amount of retained nitrogen as it is predicted from the modeling approach with  $SY_N = 2.8\overline{N_{ns}}$ , respectively as it has been measured by NRA after 15 min of ion nitriding.

a factor of 1.28 larger than the measured one. Possible reasons for this deviation may be related to the choice of the surface binding energy used for the TRIDYN simulation (refer to Section 2.2). Recalling that TRIDYN is used to *estimate* sputtering yields the deviation between predicted and measured results is still reasonable.



#### 4.3.4 Discussion

Together with findings on the role of absorption, recoil implantation, and desorption, the experimental test of the presented modeling approach suggests that the incorporation and release of nitrogen is controlled by ion implantation and sputtering, respectively. The modeling approach predicts that the nitrogen near surface concentration  $N_{ns}$  tends towards a stationary value at which the partial sputtering yield of nitrogen  $SY_N$  becomes one. The fluxes  $j_{in}$  and  $j_{rel}$  balance and the amount of retained nitrogen  $N_{ret}$  becomes stationary as well. According to the TRIDYN simulation the stationary value of  $N_{ns}$  amounts to 36 at.%. This value and the qualitative feature of a nitrogen near surface concentration that tends towards a stationary value are in reasonable agreement with nitrogen depth profiles observed after longer nitriding time [23, 57, 165, 186] (and refer to Section 4.4).

What is the role of the temperature within the presented modeling approach? The presumption that nitrogen incorporation and release are controlled by ion implantation and sputtering, respectively, that is by ballistic mechanisms, does *not* imply that the evolution of  $N_{ns}$  and  $N_{ret}$  is independent of temperature. A higher temperature results in faster diffusional nitrogen transport in the bulk and will cause the nitrogen near surface concentration to increase slower (at other processing parameters unchanged). Consequently, the stationary value of  $N_{ns}$  will be reached at the same value but after longer nitriding time. These features of  $N_{ns}$  are opposed to stationary values of  $N_{ns}$  that depend on temperature and that are reached after the same time at different temperatures as observed by Renevier et al. [165] Renevier et al. concluded that a temperature dependent phenomenon must occur at the surface and suggested a desorption-like release mechanism. However, in contrast to what would be expected for a desorption-like release mechanism (which should become faster with increasing temperature), Renevier et al. found the higher stationary nitrogen near surface concentration at the higher temperature.

A possible explanation for a stationary nitrogen near surface concentrations that increases with temperature is a temperature dependent (super)saturation limit of nitrogen in austenitic stainless steel. Such a phenomenon, which results in the release of nitrogen if the nitrogen concentration exceeds the limit, for example, by a spontaneous emission-like mechanism, would also explain why at a stationary nitrogen near surface concentration the amount of retained nitrogen does still increase (as observed, for example, in Section 4.4). In this context it should be mentioned that such a mechanism, respectively phenomenon, is necessary to link the modeling approach presented in this Section to the modeling approach presented in the next Section. The approach presented here implies that throughout the treatment the nitrogen retention rate is limited by the rate of nitrogen supply ( $j_{in} - j_{rel}$ ), while the modeling approach presented in the next Section implies that the nitrogen retention rate is limited by the diffusional transport of nitrogen. From a formal viewpoint the two approaches are incompatible, but they can be easily linked by introducing a nitrogen near surface concentration at which the nitrogen retention rate changes from rate of supply limited to diffusion limited.

Finally, it should be mentioned that we can not exclude that desorption occurs although the experiment (refer to Section 4.3.2) indicates that desorption does not occur. The reason is that desorption may start at a threshold value exceeding the maximum nitrogen

near surface concentration in that experiment. Furthermore, the experimental test is not sensitive to a desorption mechanism that is linked to chemical reactions under the nitrogen ion beam (refer to Ref. [187]).

#### 4.3.5 Summary

The role of potentially relevant nitrogen incorporation and release mechanisms has been tested by suited experiments utilizing real-time elastic recoil detection analysis. The experiments provide evidence that absorption and desorption do not significantly contribute to nitrogen incorporation and release, respectively. An approach to model the nitrogen retention during ion nitriding in terms of purely collisional mechanisms is presented and compared to experimental data obtained from a combined analysis using real-time elastic recoil detection analysis and nuclear reaction analysis. Modeling results and experimental results show reasonable agreement indicating that nitrogen incorporation and release are dominated by ion implantation and sputtering, respectively. Moreover, the role of a nitrogen (super)saturation limit and a possible additional release mechanism related to it is discussed.

## 4.4 The evolution of the thickness of the nitrogen enriched layer

### 4.4.1 Introduction

In this section, nitrogen and chromium depth profiles measured by glow discharge optical emission spectroscopy on samples that have been ion nitrided for relatively long times, are presented and discussed. After a definition of the layer thickness appropriate to trapping and detrapping, the modeling approach on the evolution of the layer thickness is applied (refer to Section 2.4). A nitrogen diffusion coefficient and a surface recession rate are determined.

### 4.4.2 Experimental results

A series of samples has been ion nitrided for different times, ranging from  $t = 15$  min to  $t = 240$  min. Sample temperature, ion energy, and current density were  $T = 400^\circ\text{C}$ ,  $E_{\text{in}} = 0.7$  keV, and  $\rho = 2.5$  mA/cm<sup>2</sup>, respectively<sup>8</sup>. Before starting the ion nitriding treatment, the samples were exposed to argon ion bombardment in order to remove the native surface oxide layer and to establish the nitriding temperature.

The ion nitrided samples have been analyzed by means of glow discharge optical emission spectroscopy (GDOES)<sup>9</sup>. Figure 4.13 shows nitrogen and chromium depth profiles obtained from GDOES. Neglecting slight deviations close to the surface, which can be attributed to a measurement artifact and to surface roughness, for all samples the nitrogen near surface concentration amounts to about 30 at.%. Additionally, the nitrogen depth profiles exhibit features that are consistent with trapping of nitrogen at chromium: (i) a leading edge at the depth where the nitrogen concentration is equal to the chromium concentration<sup>10</sup>, and (ii) an error functional decreases from the surface to that leading edge with a concentration offset equal to the chromium concentration (refer to Section 2.3 and Section 4.1).

### 4.4.3 Modeling results

In order to apply the modeling approach of the evolution of the layer thickness at constant surface concentration introduced in Section 2.4, we need to choose an appropriate definition of the layer thickness  $X$ . According to trapping theory the difference between the nitrogen

<sup>8</sup>These samples have been ion nitrided in the group of Prof. P.J. Wilbur, Department of Mechanical Engineering, Colorado State University, CO, USA. The used ion nitriding setup is similar to the one presented in Section 3.2 and is described in greater detail in Ref. [47]. A ratio  $\text{N}_2^+ : \text{N}^+ \approx 80 : 20$  and an oxygen partial pressure sufficiently low to prevent reoxidation (refer to Section 4.5) are assumed. Many thanks to Prof. D.L. Williamson, Department of Physics, Colorado School of Mines, CO, USA for providing the samples.

<sup>9</sup>GDOES has been performed at *TAZ GmbH, Seefeld, Germany*. For the principle and for details of the analytical technique refer to Ref. [188] and references therein.

<sup>10</sup>The leading edge is smeared out, which can be attributed to the relatively poor depth resolution of the GDOES technique.

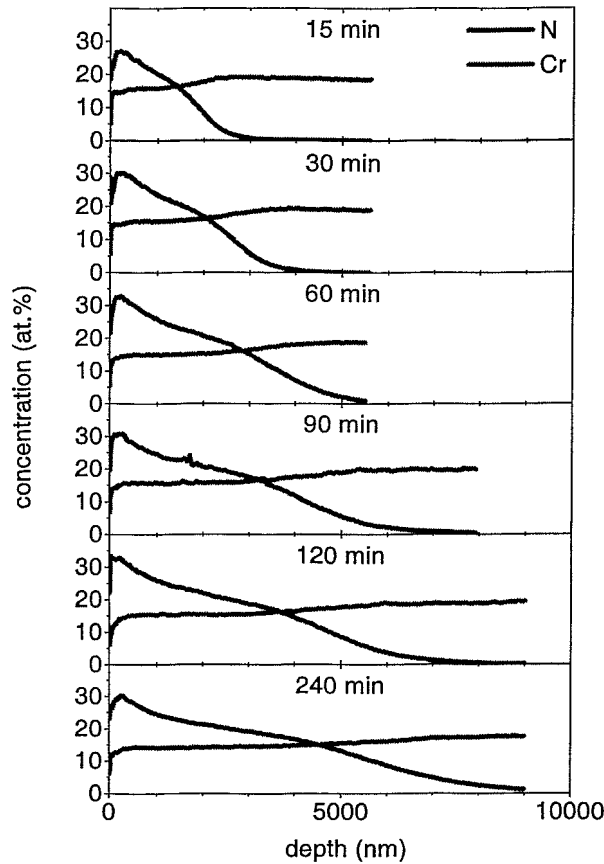


**Figure 4.13:** Nitrogen and chromium depth profiles obtained from GDOES after ion nitriding for different times at  $T = 400^{\circ}\text{C}$ ,  $E_{\text{in}} = 0.7\text{ keV}$ , and  $\rho = 2.5\text{ mA/cm}^2$ .

depth profiles and the chromium depth profiles can be considered as the depth profile of nitrogen on diffusion sites. Bearing a trapping mechanism in mind, it is appropriate to define the layer thickness as half of the depth at which the nitrogen concentration is equal to the chromium concentration. With this definition, the diffusion coefficient  $D$  in Equation 2.16 can be considered as the diffusion coefficient of nitrogen on diffusion sites (refer to Section 2.3 and Section 4.1). The evolution of the layer thickness, extracted from Figure 4.13 using the above definition of the layer thickness, is shown in Figure 4.14 (dots). For relatively short times the evolution of the layer thickness obeys a parabolic law. Following the suggestion of Dimitrov et al. [122], we determine the diffusion coefficient by fitting Equation 2.16 to relatively small layer thicknesses, respectively short nitriding times, chosen here from zero to 60 min (dashed line). The fit yields a diffusion coefficient

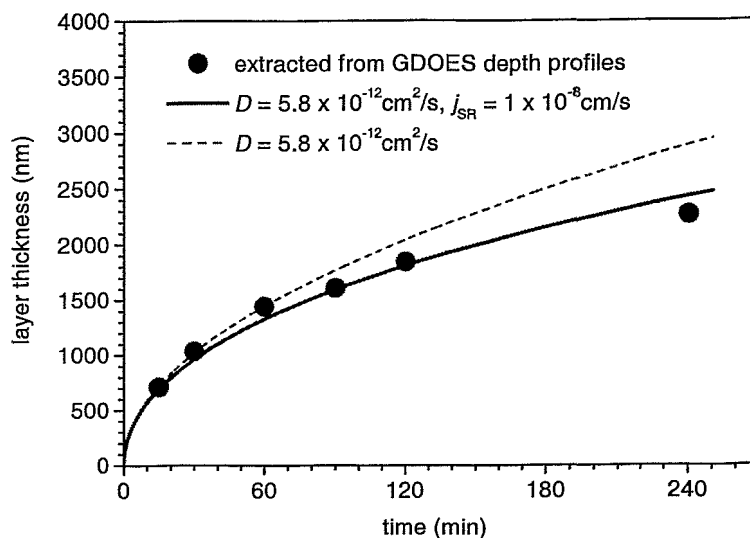


**Figure 4.14:** The evolution of the thickness of the nitrogen enriched layer. Dots: Thickness of the nitrogen enriched layer extracted from GDOES depth profiles (Figure 4.13), defining the layer thickness as the distance from the surface to the half of the depth at which the nitrogen concentration is equal to the chromium concentration. Dashed line: Fitted evolution of the layer thickness according to Equation 2.16. The time interval from zero to 60 min has been fitted, resulting in  $D = 5.8 \times 10^{-12} \text{ cm}^2/\text{s}$ . Solid line: Fitted evolution of the layer thickness according to Equation 2.17. The complete time interval has been fitted with  $D = 5.8 \times 10^{-12} \text{ cm}^2/\text{s}$ , resulting in  $j_{\text{SR}} = 1 \times 10^{-8} \text{ cm/s}$ .

$D = 5.8 \times 10^{-12} \text{ cm}^2/\text{s}$ , which is in very good agreement with the activation energy and the pre-exponential factor of diffusion of nitrogen on diffusion sites used in Section 4.1. As it is expected due to surface recession, a deviation from the parabolic behavior becomes more and more prominent with increasing layer thickness. Fitting Equation 2.17 with the same  $D$  as above to the complete time interval (straight line), yields a surface recession rate  $j_{\text{SR}} = 1 \times 10^{-8} \text{ cm/s}$ . This surface recession rate is in reasonable agreement with a TRIDYN simulation. On the basis of the obtained values for  $D$  and  $j_{\text{SR}}$ , the layer thickness is expected to become stationary at 2900 nm<sup>11</sup>.

#### 4.4.4 Discussion

It should be mentioned that a proper definition of the layer thickness (in combination with the choice of  $\beta$  in Equation 2.13) is a crucial point for the determination of the

<sup>11</sup>With the above definition of the layer thickness, a layer thickness of 2900 nm corresponds to a leading edge at a depth of approximately 8000 nm.

diffusion coefficients and surface recession rates. For example, if we would define the layer thickness as the depth at which the nitrogen concentration is equal to the chromium concentration, instead of *half* of this depth, the modeling approach would yield a four times larger diffusion coefficient, which, in turn, would also lead to a smaller surface recession rate. Thus, besides inaccurate determinations of substrate temperatures, possible reasons for the scatter of diffusion data ([73] and references therein) are (i) non-consideration of the role of the surface oxide layer (refer to Section 4.5), (ii) determination of nitrogen diffusion coefficients from depth profiles with nitrogen concentrations lower than the trap concentration (refer to Section 4.1), (iii) different definitions of the layer thickness, and (iii) neglect of surface recession.

Apparently, the modeling approach is useful to understand basic features of the layer growth kinetics. In particular if applied in combination with SRIM or TRIDYN simulations, the approach provides quantitative insight into the role of the processing parameters, including ion energy  $E_{in}$  and current density  $\rho$ . For example, the approach explains why at relatively low ion energies (in combination with good vacuum conditions and  $E_{in}$  still high enough to remove the surface oxide, respectively to prevent reoxidation) relatively thick layers can be produced, as it has been observed in Ref. [56], and why high current densities  $\rho$  may be detrimental with respect to the goal of thick layers, as it has been observed in Ref. [47, 73].

Finally, it should be stated that ion nitriding of austenitic stainless steel is not an ideal case for the application of the above modeling approach on the evolution of the layer thickness. This is due to the fact that for relatively short times the nitrogen near surface concentration is actually not constant (compare to Section 4.3). Nevertheless, as long as time and temperature regimes are considered for which the conditions (i) constant surface concentration and (ii)  $D$  independent of time (no phase transformation) are reasonably fulfilled, the approach is very useful, not only for ion nitriding of austenitic stainless steels, but for transport during ion implantation and deep diffusion in general. This applies for the determination of diffusion coefficients and surface recession rates, as well as with respect to process optimization towards thick layers.

#### 4.4.5 Summary

Nitrogen and chromium depth profiles measured by glow discharge optical emission spectroscopy on samples that have been ion nitrided at 400°C for different relatively long times are presented and discussed. The depth profiles reveal that a stationary nitrogen near surface concentration of about 30 at.% establishes. A definition of the layer thickness appropriate to trapping and detrapping is given and the modeling approach for the evolution of the layer thickness is applied (refer to Section 2.4). A diffusion coefficient of nitrogen on diffusion sites of  $D = 5.8 \times 10^{-12}$  cm<sup>2</sup>/s and a surface recession rate  $j_{SR} = 1 \times 10^{-8}$  cm/s are determined from the evolution of the layer thickness. Both values are in reasonable agreement with nitrogen diffusion data used in Section 4.1 and a surface recession rate estimated by TRIDYN, respectively.

## 4.5 The role of the surface oxide layer

### 4.5.1 Introduction

Austenitic stainless steels exhibit a native surface oxide layer that protects the metal matrix from corrosion. The oxide layer is believed to inhibit nitrogen diffusion or, actually, to act as a barrier for diffusional nitrogen transport [1, 33, 56, 51]. Therefore, in view of process optimization towards efficient nitriding, a pre-cleaning procedure, which is supposed to remove the oxide layer, is generally recommended [1, 33]. It is evident, however, that it is not sufficient to remove the native surface oxide layer prior to nitriding, but that the surface needs to be prevented from reoxidation throughout the nitriding treatment. With a few exceptions [77, 56], this fact, although it may be considered as a major obstacle for successful nitriding of metals that form dense and stable native surface oxide layers [189, 190], received little attention so far.

In this Section, we will start with some basic considerations on the surface oxide layer and the oxygen transport during ion nitriding. Then, time resolved depth profiles obtained from real-time elastic recoil detection analysis during ion nitriding at different processing parameters are presented and discussed. The experimental data are compared to semi-quantitative considerations on the oxide removal and oxide growth and to modeling results. These comparisons provide insight into the role of the surface oxide layer during ion nitriding of austenitic stainless steel. The key questions addressed are:

- How do the processing parameters affect the thickness of the surface oxide layer?
- How does the thickness of the surface oxide layer affect the ion nitriding kinetics?

### 4.5.2 Basic considerations on oxide removal and oxide growth

In spite of a rather complex chemistry and composition of the surface oxide layer (refer, for example, to Refs. [191, 192, 193, 194, 195]), for the present purpose it is reasonable to assume that all oxygen is present near the surface in form of a stoichiometric and lateral homogenous  $\text{Cr}_2\text{O}_3$ -layer with a density of  $5.21 \text{ g/cm}^3$  [196]. With this assumption, an oxygen areal density  $O_{\text{ret}} = 1 \times 10^{16} \text{ at./cm}^2$  corresponds to  $1.615 \text{ nm}$  or  $6.39 \text{ ML}^{12}$ . During ion nitriding, sputtering contributes to the removal of the surface oxide layer. On the other hand the surface oxide layer may grow due to oxidation from the residual gas. Let us consider the oxygen transport with the following assumptions:

- The evolution of the surface oxide layer thickness is completely controlled by the interplay of sputtering and oxidation.
- For small oxide layer thicknesses, the oxide growth rate is limited by the flux of oxygen atoms from the residual gas onto the surface of the substrate.

---

<sup>12</sup>Alternatively a  $\text{Fe}_2\text{O}_3$ -layer with a density of  $5.24 \text{ g/cm}^3$  (hematite) [196] may be assumed.

- With increasing oxide layer thickness, the oxide growth rate becomes limited by the diffusion of one or both species (oxygen or chromium) across the layer. The diffusion limited oxide growth follows a parabolic law.
- The oxygen removal rate due to sputtering is constant during ion nitriding (if a surface oxide layer is present).

With these assumptions the evolution of the oxide layer thickness during ion nitriding is described by the following differential equations

$$\frac{dX}{dt} = j_{IG} - j_{OR}, \text{ for } X > 0 \text{ and } j_{IG} \leq \frac{k_O}{2X}, \quad (4.13)$$

and

$$\frac{dX}{dt} = \frac{k_O}{2X} - j_{OR}, \text{ for } X > 0 \text{ and } j_{IG} \geq \frac{k_O}{2X}, \quad (4.14)$$

where  $X$  denotes the oxide layer thickness,  $t$  the time,  $j_{IG}$  the initial growth rate limited by the rate of supply of oxygen from the residual gas,  $j_{OR}$  the oxide removal rate due to sputtering, and  $k_O$  a rate constant of the diffusion limited oxide growth.

Equation 4.14 is formally similar to Equation 2.17, but for the description of the evolution of the layer thickness we now discriminate between rate of supply limited layer growth and diffusion limited layer growth (refer to Section 4.3.4). Qualitatively, Equation 4.13 and Equation 4.14 predict that the surface oxide layer will be removed in case of  $j_{IG} < j_{OR}$ , while in case of  $j_{IG} > j_{OR}$  the diffusion limited oxide growth rate and the oxide removal rate compete and an oxide layer with a stationary thickness  $X_{stat} = k_O/2j_{OR}$  will establish.

For quantitative estimates we assume that the initial oxide growth is given by kinetic gas theory according to

$$j_{IG} = 2p(O_2)/\sqrt{2\pi mkT_g}, \quad (4.15)$$

where  $p(O_2)$  denotes the oxygen partial pressure,  $k$  the Boltzmann constant,  $T_g$  the temperature of the gas (taken as room temperature) and  $m$  the mass of an oxygen molecule<sup>13</sup>. The oxide removal rate  $j_{OR}$  is estimated according to

$$j_{OR} = j_{in} \times \int f(E) SY_0(E) dE, \quad (4.16)$$

where  $j_{in}$  denotes the incoming flux of energetic nitrogen atoms,  $f(E)$  the nitrogen energy distribution and  $SY_0(E)$  the oxygen sputtering yield simulated by SRIM. The surface binding energy of oxygen  $E_s(O)$ , which is an important input parameter for SRIM, has been calculated considering that the sum of the surface binding energies of chromium and oxygen must be consistent with the thermodynamic balance (refer to Section 2.2, Equation 2.1) Taking  $E_s(Cr) = \Delta H_s(Cr) = 4.12$  eV for the pure metal [99],  $\Delta H_m(O) = 5.17$  eV [196], and  $\Delta H_f(Cr_2O_3) = 11.81$  eV [196] results in  $E_s(O) = 6.52$  eV.

<sup>13</sup>For simplicity, a sticking coefficient of one is assumed and oxygen carrying molecules other than molecular oxygen are not considered.



### 4.5.3 Experimental results

#### Real-time ERDA during ion nitriding at different combinations of ion energy and oxygen partial pressure

In order to corroborate these considerations, three samples have been ion nitrided at identical temperature and current density ( $T = 320^\circ\text{C}$ ,  $\rho = 0.2\text{ mA/cm}^2$ ), but different combinations of ion energy  $E_{\text{in}}$  and oxygen partial pressure  $p(O_2)$ . A first sample has been ion nitrided at a low ion energy and a high oxygen partial pressure ( $E_{\text{in}} = 0.3\text{ keV}$ ,  $p(O_2) = 5 \times 10^{-3}\text{ Pa}$ ), a second sample has been ion nitrided at a high ion energy and a high oxygen partial pressure ( $E_{\text{in}} = 1.0\text{ keV}$ ,  $p(O_2) = 5 \times 10^{-3}\text{ Pa}$ ), and a third sample has been ion nitrided at a high ion energy and a low oxygen partial pressure ( $E_{\text{in}} = 1.0\text{ keV}$ ,  $p(O_2) = 1 \times 10^{-4}\text{ Pa}$ ).

Table 4.4 shows initial oxide growth rates and oxide removal rates estimated on the basis of the above considerations. For the first two samples the initial oxide growth rates

processing parameters		estimated rates	
$E$ (keV)	$p(O_2)$ (Pa)	$j_{\text{IG}}$ (at./cm <sup>2</sup> s)	$j_{\text{OR}}$ (at./cm <sup>2</sup> s)
0.3	$5 \times 10^{-3}$	$2.67 \times 10^{16}$	$3.6 \times 10^{14}$
1.0	$5 \times 10^{-3}$	$2.67 \times 10^{16}$	$1.3 \times 10^{15}$
1.0	$1 \times 10^{-4}$	$5.33 \times 10^{14}$	$1.3 \times 10^{15}$

**Table 4.4:** Estimated rates (initial oxide growth rate due to reoxidation  $j_{\text{IG}}$  and oxide removal rate due to sputtering  $j_{\text{OR}}$  for different combinations of ion energy  $E_{\text{in}}$  and oxygen partial pressure  $p(O_2)$ ).

are larger than the oxide removal rates ( $j_{\text{IG}} > j_{\text{OR}}$ ). The opposite holds for the third sample ( $j_{\text{IG}} < j_{\text{OR}}$ ).

For all three samples, time resolved depth profiles have been obtained from real-time ERDA during ion nitriding. Before starting the nitrogen ion bombardment, the samples were exposed to the processing temperature and the respective oxygen partial pressures for about 20 min. Nitrogen ion bombardment starts at time  $t = 0$  and was limited by the time at which the nitrogen depth profile approached the maximum detection depth of real-time ERDA.

Figure 4.15 shows time resolved depth profiles of oxygen and nitrogen and the corresponding evolution of areal densities for the sample ion nitrided at the low ion energy and the high oxygen partial pressure ( $E_{\text{in}} = 0.3\text{ keV}$ ,  $p(O_2) = 5 \times 10^{-3}\text{ Pa}$ ). Right before the nitrogen ion bombardment starts, the oxygen areal density amounts to  $O_{\text{ret}} = 15.5 \times 10^{16}\text{ at./cm}^2$  (averaged from the time interval between  $t = -5\text{ min}$  and  $t = 0\text{ min}$ ), corresponding to a 26.1 nm thick oxide layer. Upon starting the nitrogen ion bombardment, oxygen gets removed at an initial rate of  $1.9 \times 10^{14}\text{ at./cm}^2\text{s}$  (estimated from a linear fit to the oxygen areal density in the time interval between  $t = -30\text{ s}$  and  $t = 150\text{ s}$ ).

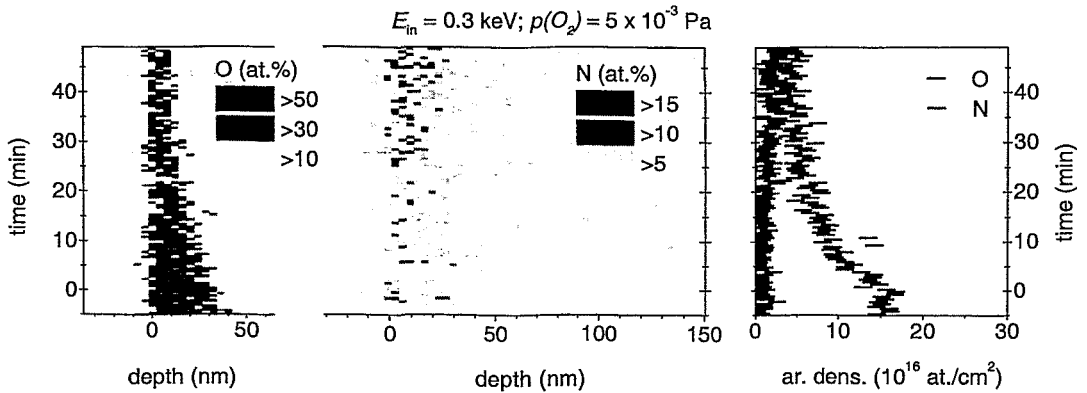


**Figure 4.15:** Time resolved depth profiles of oxygen (left) and nitrogen (center) and corresponding evolution of oxygen and nitrogen areal densities (right) obtained from real-time ERDA. Ion nitriding at an ion energy  $E_{in} = 0.3$  keV, a current density  $\rho = 0.2$  mA/cm<sup>2</sup>, a sample temperature  $T = 320^\circ\text{C}$ , and an oxygen partial pressure  $p(O_2) = 5 \times 10^{-3}$  Pa starts at time  $t = 0$  min.

Within the statistics of real-time ERDA, the oxygen areal density decreases continuously and finally tends towards a stationary value of  $4.3 \times 10^{16}$  at./cm<sup>2</sup> (averaged from the oxygen areal density during the last 10 minutes of the treatment) corresponding to a 7.2 nm thick oxide layer. The evolution of the nitrogen depth profile and areal density shows only little nitrogen enrichment near the surface.

Figure 4.16 shows time resolved depth profiles of oxygen and nitrogen and the corresponding evolution of areal densities for the sample ion nitrided at the high ion energy and the high oxygen partial pressure ( $E_{in} = 1.0$  keV,  $p(O_2) = 5 \times 10^{-3}$  Pa). Right before the nitrogen ion bombardment starts, the oxygen areal density amounts to  $O_{ret} = 11.7 \times 10^{16}$  at./cm<sup>2</sup> (averaged from the time interval between  $t = -5$  min and  $t = 0$  min), corresponding to a 19.7 nm thick oxide layer. Upon starting the nitrogen ion bombardment, oxygen gets removed at an initial rate of  $2.3 \times 10^{14}$  at./cm<sup>2</sup>s (estimated from a linear fit to the oxygen areal density in the time interval between  $t = -30$  s and  $t = 90$  s). Again the oxide removal rate slows down continuously. Already after about 5 minutes, a stationary oxygen areal density of  $1.3 \times 10^{16}$  at./cm<sup>2</sup> (averaged from the oxygen areal density between  $t = 10$  min and  $t = 20$  min) establishes, corresponding to a 2.2 nm thick oxide layer. The evolution of the depth profile and areal density of nitrogen shows that, with a delay corresponding to a significant reduction of the oxygen areal density, nitrogen concentrations exceeding a few atomic percent are established in the subsurface. With increasing ion nitriding time the nitrogen depth profile spreads out towards depth at a rate of approximately 5 nm/min. The corresponding nitrogen retention rate (estimated from a linear fit to the nitrogen areal density in the time interval between  $t = 10$  min and  $t = 20$  min) amounts to  $4.9 \times 10^{13}$  at./cm<sup>2</sup>s. After an ion nitriding time of 23.5 min the nitrogen depth profile approaches the maximum detection depth of real-time ERDA and the nitrogen ion

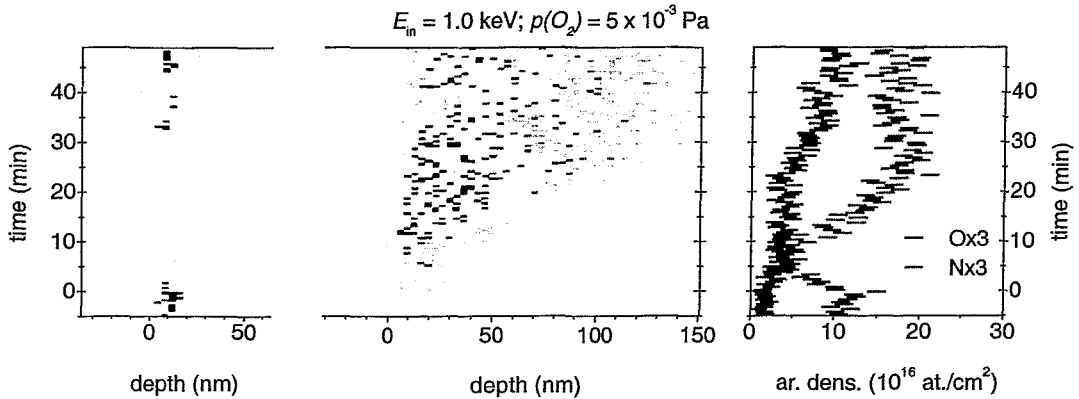


**Figure 4.16:** Time resolved depth profiles of oxygen (left) and nitrogen (center) and corresponding evolution of oxygen and nitrogen areal densities (right) obtained from real-time ERDA. For the units of the color scale refer to Figure 4.15. Ion nitriding at an ion energy  $E_{in} = 1.0$  keV, a current density  $\rho = 0.2$  mA/cm<sup>2</sup>, a sample temperature  $T = 320^\circ\text{C}$ , and an oxygen partial pressure  $p(O_2) = 5 \times 10^{-3}$  Pa starts at time  $t = 0$  min and stops at time  $t = 23.5$  min.

bombardment is stopped. Subsequently, the oxygen areal density increases at an initial rate of  $1.55 \times 10^{14}$  at./cm<sup>2</sup> (estimated from a linear fit to the oxygen areal density in the time interval between  $t = 23.5$  min and  $t = 25$  min). During the 25 minutes following the stop of the nitriding ion bombardment, the oxygen areal density tends towards its initial value.

Figure 4.17 shows time resolved depth profiles of oxygen and nitrogen and the corresponding evolution of areal densities for the sample ion nitrided at the high ion energy and the low oxygen partial pressure ( $E_{in} = 1.0$  keV,  $p(O_2) = 1 \times 10^{-4}$  Pa). Right before the nitrogen ion bombardment starts, the oxygen areal density amounts to  $O_{ret} = 7.4 \times 10^{16}$  at./cm<sup>2</sup> (averaged from the time interval between  $t = -5$  min and  $t = 0$  min), corresponding to a 12.5 nm thick oxide layer. Upon starting the nitriding ion bombardment, oxygen gets removed at an initial rate of  $3.1 \times 10^{14}$  at./cm<sup>2</sup>s (estimated from a linear fit to the oxygen areal density in the time interval between  $t = -30$  s and  $t = 30$  s). Quickly, the oxygen areal density amounts to less than  $2 \times 10^{15}$  at./cm<sup>2</sup> (averaged from the oxygen areal density between 2 min and 4 min), which is in the range of the possible background (refer to Section 3.3.3). The evolution of the depth profile and areal density of nitrogen show that, quickly after nitrogen ion bombardment starts, high concentrations of nitrogen are established in the subsurface. The nitrogen depth profile spreads out towards depth at a rate of approximately 30 nm/min. The corresponding nitrogen retention rate (estimated from a linear fit to the oxygen areal density in the time interval between  $t = 0.5$  min and  $t = 3.5$  min) amounts to  $4.3 \times 10^{14}$  at./cm<sup>2</sup>s. Already after 4 min the nitrogen depth profile approaches the maximum detection depth of real-time ERDA and the nitrogen ion bombardment is stopped. Subsequently, the nitrogen depth profile broadens

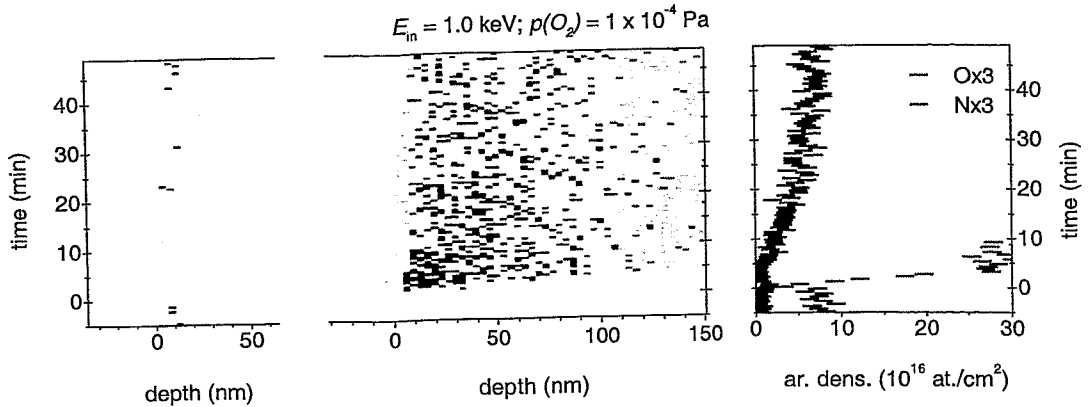


**Figure 4.17:** Time resolved depth profiles of oxygen (left) and nitrogen (center) and corresponding evolution of oxygen and nitrogen areal densities (right) obtained from real-time ERDA. For the units of the color scale refer to Figure 4.15. Ion nitriding at an ion energy  $E_{in} = 1.0$  keV, a current density  $\rho = 0.2$  mA/cm<sup>2</sup>, a sample temperature  $T = 320^\circ\text{C}$ , and an oxygen partial pressure  $p(O_2) = 1 \times 10^{-4}$  Pa starts at time  $t = 0$  min and stops at time  $t = 4$  min.

with no evidence of nitrogen release (the nitrogen areal density remains almost constant) and the oxygen areal density increases up to its initial thickness at an initial growth rate of  $3.2 \times 10^{13}$  at./cm<sup>2</sup>s (estimated from a linear fit to the oxygen areal density in the time interval between  $t = 4$  min and  $t = 10$  min).

Apparently the above data sustain our considerations on the oxygen transport. As expected, a surface oxide layer with stationary non-zero thickness establishes at the two high oxygen partial pressures where  $j_{IG} > j_{OR}$ , while the surface oxide layer is essentially removed at the low oxygen partial pressure where  $j_{IG} < j_{OR}$ . Additionally, at  $E_{in} = 1.0$  keV,  $p(O_2) = 5 \times 10^{-3}$  Pa the stationary oxide thickness is significantly smaller than at  $E_{in} = 0.3$  keV,  $p(O_2) = 5 \times 10^{-3}$  Pa, which is consistent with a lower oxide removal rate at the lower ion energy. Further, the nitrogen retention rate at  $E_{in} = 0.3$  keV is negligible compared to respective rates at the higher ion energy. At this ion energy the mean projected range of nitrogen is much smaller than the stationary oxide layer thickness and, apparently, the nitrogen implanted into the surface oxide layer gets reemitted to the residual gas rather than contributing to in-depth diffusion. This is a strong evidence that the surface oxide layer actually acts as a barrier for diffusional transport of nitrogen.

#### Real-time ERDA during ion nitriding at different oxygen partial pressure

In a more systematical investigation focussing on the role of the oxygen partial pressure a series of samples has been ion nitrided at identical ion energy, current density, and temperature ( $E_{in} = 2$  keV,  $\rho = 0.2$  mA/cm<sup>2</sup>, and  $T = 320^\circ\text{C}$ ), but different oxygen partial pressures (varied from  $p(O_2) = 9 \times 10^{-3}$  Pa down to  $p(O_2) < 3 \times 10^{-5}$  Pa). Before

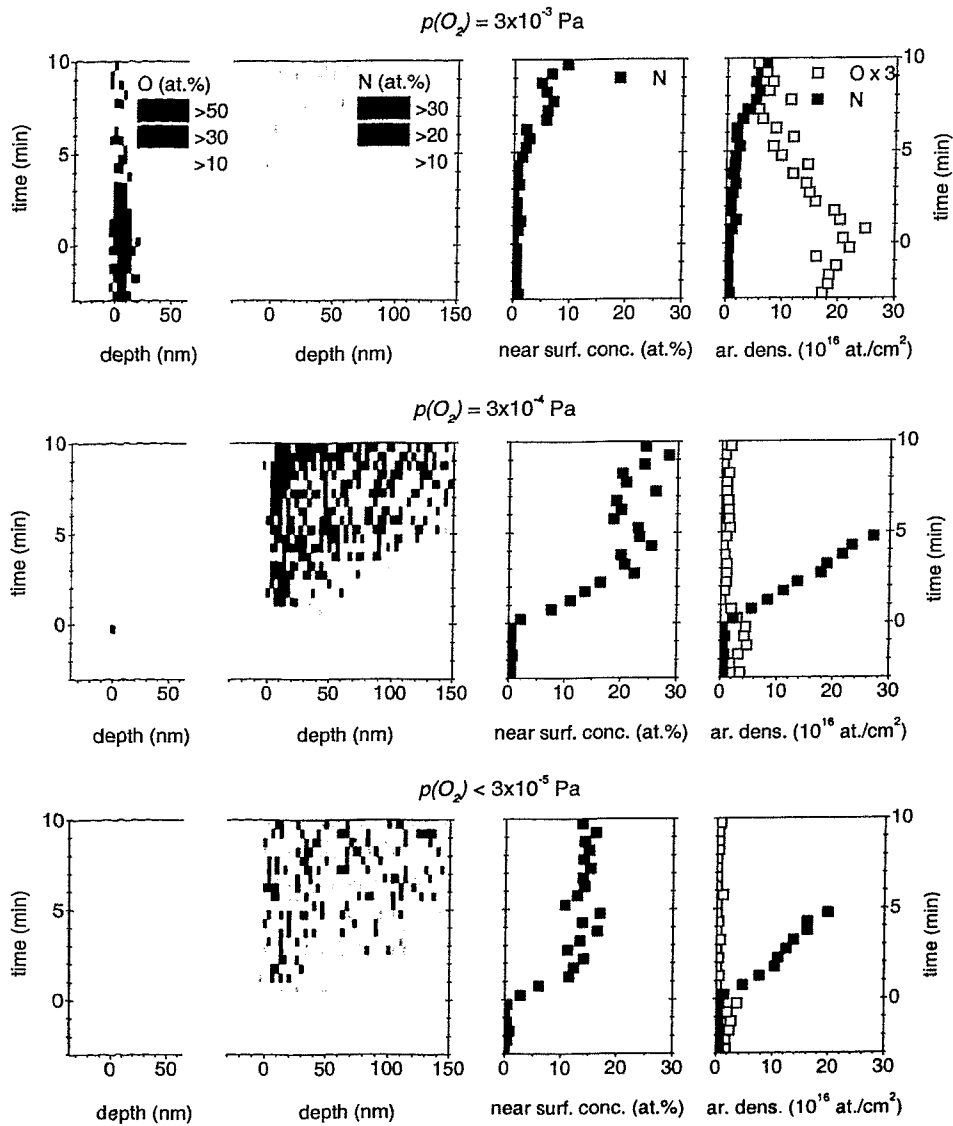


**Figure 4.18:** Time resolved depth profiles of oxygen (left) and nitrogen (center) and corresponding evolution of oxygen and nitrogen areal densities (right) obtained from real-time ERDA. Ion nitriding at an ion energy  $E_{in} = 2.0 \text{ keV}$ , a current density  $\rho = 0.2 \text{ mA/cm}^2$ , a sample temperature  $T = 320^\circ\text{C}$ , and different oxygen partial pressure  $p(O_2)$  starts at time  $t = 0 \text{ min}$  and stops at time  $t = 10 \text{ min}$ .

starting the nitrogen ion bombardment that lasted 10 min, the samples were exposed to the processing temperature and the respective oxygen partial pressures for about 20 min.

Figure 4.18 shows time resolved depth profiles of oxygen and nitrogen and the corresponding evolution of areal densities at three selected oxygen partial pressures. As expected from the above considerations on the oxide growth and the oxide removal, at all oxygen partial pressures the thickness of the oxide tends towards a stationary value. The stationary thickness becomes smaller with decreasing oxygen partial pressure and is essentially zero at the lowest oxygen partial pressure, where  $j_{IG} < j_{OR}$  (compare to Table 4.5). At the highest oxygen partial pressure only relatively small amounts of nitrogen are retained after 10 min, while at the two other oxygen partial pressures the leading edges of the nitrogen profiles exceed the detection limit of real-time ERDA already after about 5 min. Apparently, the oxygen partial pressure is a key parameter for successful ion nitriding of austenitic stainless steel.

Comparing the dynamic nitrogen depth profiles measured at the two lower oxygen partial pressures, it appears that at  $p(O_2) = 3 \times 10^{-4}$  Pa a higher nitrogen concentration level builds up than at  $p(O_2) < 3 \times 10^{-5}$  Pa. This observation is confirmed by comparing the evolution of the nitrogen near surface concentrations and the evolution of the nitrogen areal densities, respectively. Indeed at  $p(O_2) = 3 \times 10^{-4}$  Pa both the nitrogen near surface concentration (more than 20 at.% compared to about 15 at.%) as well as the nitrogen retention rate (about  $8.5 \times 10^{14}$  at./cm<sup>2</sup>s compared to about  $6.5 \times 10^{14}$  at./cm<sup>2</sup>s) are significantly larger than at the low oxygen partial pressure. This suggests that a thin surface oxide layer improves the ion nitriding kinetics. Such a feature is consistent with the surface oxide layer acting as a barrier for diffusional nitrogen transport and the picture that only nitrogen which gets implanted behind the surface oxide is retained in the sample. If the nitrogen ion energy is high, respectively the thickness of the surface oxide layer is small but not zero, most of the nitrogen gets implanted behind the surface oxide. Concurrently the nitrogen release rate will be reduced compared to a completely removed surface oxide layer, since the partial sputtering yield of nitrogen decreases<sup>14</sup>. Thus, higher nitrogen retention rates resulting in higher concentration gradients and faster nitrogen influxes can be expected.

### Real-time ERDA during ion nitriding at different ion energies

To corroborate this picture, which is also consistent with the data obtained for the sample ion nitrided at  $E_{in} = 1.0$  keV and  $p(O_2) = 5 \times 10^{-3}$  Pa (Figure 4.16), we tried to ion nitride two samples at the same oxygen areal densities, but different ion energies. Figure 4.19 shows time resolved depth profiles of oxygen and nitrogen and the corresponding evolution of areal densities for these two samples. At both ion energies the oxygen areal density that is present before the nitrogen ion bombardment starts, amounts to about  $O_{ret} = 6 \times 10^{16}$  O/cm<sup>2</sup>, corresponding to an oxide layer thickness of approximately 10 nm. It takes about 10 min to establish a desired oxygen areal density of approximately  $2 \times 10^{16}$  O/cm<sup>2</sup> corresponding to an oxide layer thickness of approximately 3.2 nm. Although the mean value of the oxygen areal density between  $t = 10$  min and  $t = 20$  min is slightly lower at  $E_{in} = 0.4$  keV

<sup>14</sup>Recall that sputtered atoms originate from the topmost 2 to 3 atomic layers [90].

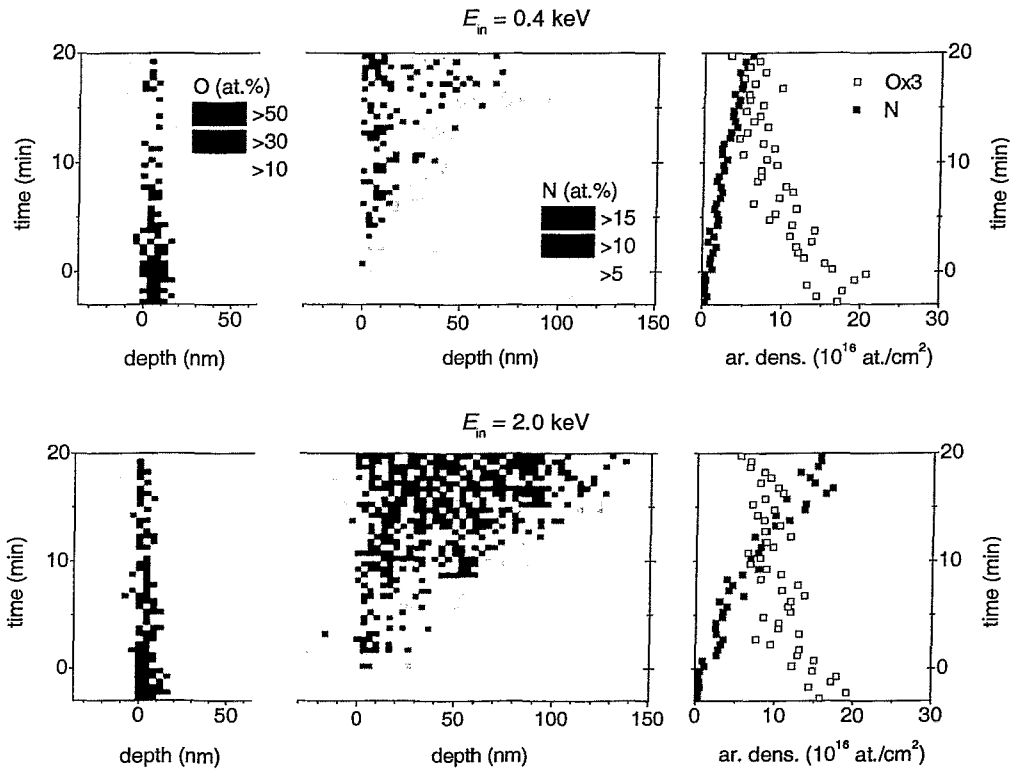


**Figure 4.19:** Time resolved depth profiles of oxygen (left) and nitrogen (center) and corresponding evolution of oxygen and nitrogen areal densities (right) obtained from real-time ERDA. Ion nitriding at a temperature  $T = 320^\circ\text{C}$ , a current density  $\rho = 0.1 \text{ mA/cm}^2$ , and different ion energies  $E_{\text{in}} = 0.4 \text{ keV}$  (top) and  $E_{\text{in}} = 2.0 \text{ keV}$  (bottom) starts at time  $t = 0 \text{ min}$  and stops at time  $t = 20 \text{ min}$ . The oxygen partial pressure  $p(O_2)$  has been adjusted such that an almost constant areal density of oxygen established after about 10 min.

( $2.3 \times 10^{16} \text{ at./cm}^2$  compared to  $2.6 \times 10^{16} \text{ at./cm}^2$  at  $E = 2.0 \text{ keV}$ ) the mean nitrogen retention rate during this time interval is about three times larger at the higher energy ( $1.6 \times 10^{14} \text{ at./cm}^2\text{s}$  at  $E_{\text{in}} = 2.0 \text{ keV}$  compared to  $5 \times 10^{13} \text{ at./cm}^2\text{s}$  at  $E_{\text{in}} = 0.4 \text{ keV}$ ). According to SRIM simulations, the amount of nitrogen being implanted behind the surface oxide amounts to 15% of the incoming nitrogen flux ( $\rho = 0.1 \text{ mA/cm}^2$  correspond to  $9.4 \times 10^{14} \text{ N/cm}^2\text{s}$ ) at the higher energy and to 5% at the lower energy. Comparison of the experimental results with these prediction of SRIM simulations yields good agreement with respect to the ratio of retained nitrogen at the higher and the lower energy as well as with respect to the absolute values of the nitrogen retention rate. Thus, the applicability of our picture is supported.

#### 4.5.4 Modeling results

Now let us consider the evolution of the surface oxide during ion nitriding more closely. Figure 4.20 shows the measured evolution of the oxygen areal densities, respectively of the oxide layer thickness, for the complete set of samples ion nitrided at different oxygen partial pressure (refer to Figure 4.18). The oxide layer thickness being present before starting the

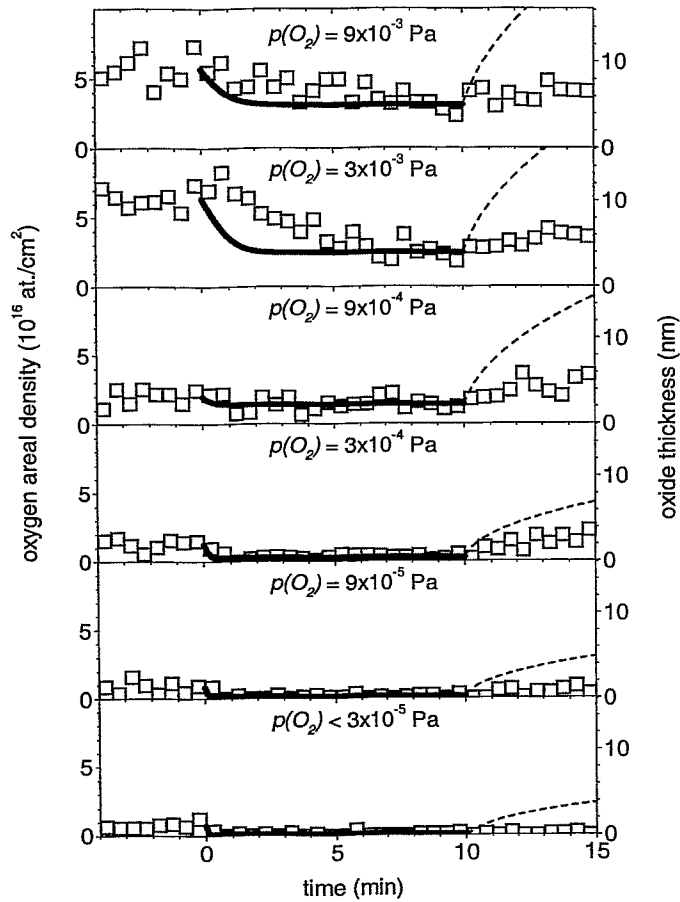


**Figure 4.20:** Evolution of oxygen areal densities, respectively oxide layer thicknesses, obtained experimentally from real-time ERDA before, during and after ion nitriding at different oxygen partial pressures (squares) and as calculated according to Equation 4.13 and Equation 4.14 with the values given in Table 4.5 (solid line). Additionally shown is the increase of the oxide layer thickness that would be expected after stopping the nitriding assuming the same  $k_O$  (dashed line). For the ion nitriding parameters refer to the caption of Figure 4.18.



$p(O_2)$ (Pa)	$j_{IG}$ (nm/s)	$j_{OR}$ (nm/s)	$X_{ini}$ (nm)	$X_{stat}$ (nm)	$k_O$ (nm <sup>2</sup> /s)	$X_{d2s}$ (nm)
$9 \times 10^{-3}$	7.8	0.16	9.2	5.1	1.60	0.10
$3 \times 10^{-3}$	2.6	0.16	10.3	4.1	1.27	0.24
$9 \times 10^{-4}$	0.78	0.16	3.2	2.3	0.73	0.47
$3 \times 10^{-4}$	0.26	0.16	2.1	0.5	(0.16)	(0.31)
$9 \times 10^{-5}$	0.078	0.16	1.3	0.2	-	-
$< 3 \times 10^{-5}$	$< 0.026$	0.16	1.2	0.1	-	-

**Table 4.5:** Measured values and values resulting from the modeling approach for the evolution of the surface oxide layer thickness.  $j_{IG}$  and  $j_{OR}$  were calculated according to Equation 4.15, respectively Equation 4.16.  $X_{ini}$  and  $X_{stat}$  were taken from the real-time ERDA measurements by averaging over time intervals between  $t = -5$  min and  $t = 0$  min, respectively between  $t = 7$  min and  $t = 10$  min.  $k_O$  and  $X_{d2s}$  were calculated according to Equation 4.13 and Equation 4.14 using the earlier values.

nitrogen ion bombardment varies from about 10 nm at the highest oxygen partial pressure down to about 1 nm at the lowest oxygen partial pressure. About 7 min after starting the ion nitriding all samples exhibit an almost stationary oxide layer thickness, varying from about 5 nm at the highest oxygen partial pressure down to less than 0.5 nm at the lowest oxygen partial pressure. With decreasing oxygen partial pressure the stationary thickness appears to be reached after shorter times and at lower values. Besides at the lowest oxygen partial pressure, the oxide layer thickness starts to increase significantly after stopping the nitrogen ion bombardment at  $t = 10$  min.

For a quantitative modeling of the evolution of the oxide thickness during ion nitriding we recall Equation 4.13 and Equation 4.14. Table 4.5 lists the initial growth rates  $j_{IG}$  and the oxide removal rates due to sputtering  $j_{OR}$  that are estimated according to Equation 4.15 and Equation 4.16 from the different oxygen partial pressures, respectively from the ion energies and the current densities. Additionally listed are the initial and stationary oxide thickness  $X_{ini}$ , respectively  $X_{stat}$ , that have been measured by means of real-time ERDA, the rate constant  $k_O$  and the thickness  $X_{d2s}$ , that is, the oxide thickness at which the oxide growth is expected to change from diffusion limited growth to rate of supply limited growth (at decreasing oxide thickness). The latter values were calculated according Equation 4.13 and Equation 4.14 using  $k_O = 2 j_{OR} X_{stat}$  and  $X_{d2s} = k_O / 2 j_{IG}$ .

For the two lowest oxygen partial pressures  $j_{IG}$  is much smaller than  $j_{OR}$ . Thus, the surface oxide layer is expected to be removed completely and neither  $k_O$  nor  $X_{d2s}$  can be calculated. For the three highest oxygen partial pressures,  $j_{IG}$  is much bigger than  $j_{OR}$ . Thus, a non-zero stationary oxide thickness is expected. From the measured stationary thickness  $X_{stat}$ , the rate constant  $k_O$  can be calculated assuming  $j_{OR}$  to be correct. From the rate constant  $k_O$ , in turn, the thickness  $X_{d2s}$  can be calculated assuming  $X_{ini}$  to be

correct, and for the intermediate oxygen partial pressure of  $3 \times 10^{-4}$  Pa,  $j_{IG}$  is only slightly higher than  $j_{OR}$ . Deviations of the physical reality from the assumed values (for example due to a sticking coefficient of 0.5 instead of 1) could easily lead to the case where a zero stationary thickness would be expected. Thus, the calculated values of  $k_O$  and  $X_{d2s}$  are given in parentheses for this oxygen partial pressure.

#### 4.5.5 Discussion

The above data demonstrate that the surface oxide layer actually acts as a barrier for diffusional nitrogen transport and provide evidence that the thickness of the surface oxide layer is completely controlled by the interplay of sputtering and oxidation. The data also suggest that the surface oxide layer may be used beneficially in order to improve the ion nitriding kinetics.

As for the two highest oxygen partial pressures the measured reduction of the thickness immediately after starting the nitriding is slower than expected from the calculation it is likely that the oxide removal rate  $j_{OR}$  as it has been taken from the SRIM simulation is overestimated (which, in turn, would lead to a smaller  $k_O$ ). This might be due to the formation of an oxynitride layer and thus to a depletion of oxygen in the depth region from where the sputtered atoms originate.

Apparently, the measured increase of the layer thickness after stopping the nitriding is slower than it would be expected assuming the same  $k_O$ . Besides the potential error in the calculation of  $k_O$  due to an overestimated oxide removal rate, possible reasons for the deviation may occur from simplified assumptions on the oxidation kinetics (refer to Section 4.5.2). One reason that should be mentioned explicitly in this context, is the fact that the net electric current, which is often assumed to play an important role for oxidation kinetics [108], is zero before and after ion nitriding but non-zero during ion nitriding.

A third thing to be discussed is the measured stationary thickness  $X_{stat}$  at the lower oxygen partial pressures. Though it is small, it is not zero. While at the two lowest oxygen partial pressures the reason can be due to background produced by pile up (refer to Section 3.3.3), the thickness measured at the intermediate oxygen partial pressure  $p(O_2) = 3 \times 10^{-4}$  Pa exceeds the possible background. Nevertheless, at this stationary thickness the layer growth is not necessarily limited by diffusional growth, since the assumption of a constant oxide removal rate is probably not fulfilled at layer thicknesses of less than 3 ML. At such small layer thicknesses  $j_{OR}$  will decrease with decreasing layer thickness, since the sputtered atoms originate from this depth interval [90]. A rigorous consideration of this feature leads to a depth depending oxide removal rate in Equation 4.13 such that a non-zero stationary thickness controlled by the interplay of initial oxide growth and oxide removal due to sputtering would be expected at  $j_{OR}(X) = j_{IG}$ .

#### 4.5.6 Summary

A modeling approach for the evolution of the thickness of the surface oxide layer is presented. The approach bases on the assumption that during ion nitriding the surface oxide layer thickness is completely controlled by the interplay of sputtering and oxidation and

differentiates between oxide layer growth limited by diffusion and oxide layer growth limited by the rate of oxygen supply. This modeling approach allows for predictions on how the processing parameters affect the thickness of the surface oxide layer. Data obtained by real-time ERDA during ion nitriding at different combinations of ion energy and oxygen partial pressure, respectively at different oxygen partial pressure, support the applicability of the modeling approach. For example, a surface oxide layer with stationary non-zero thickness establishes if the expected initial oxide growth rate is larger than the expected oxide removal rate due to sputtering while the surface oxide layer is essentially removed in the opposed case. The data also provide strong evidence that the surface oxide layer acts as a barrier for diffusional nitrogen transport and that the oxygen partial pressure is a key parameter for successful nitriding. Additionally, the data suggest that a thin surface may improve the ion nitriding kinetics. Such a feature is consistent with a surface oxide layer that acts as a barrier for diffusional nitrogen transport and with the picture and that only nitrogen which gets implanted behind the layer is retained in the sample. This picture is corroborated by comparing real-time ERDA data obtained at different ion energies and similar stationary oxide layer thicknesses with predictions of SRIM simulations.

# Chapter 5

## Summary

The purpose of this work is to improve the understanding of nitrogen transport during ion nitriding of austenitic stainless steel and of transport during surface modification of metals by ion implantation and deep diffusion in general.

An experiment that allows to describe the ion nitriding process in terms of a reasonable number of relevant processing parameters has been set up. These processing parameters can be varied independently and are closely coupled to physical parameters. With these features the premise for a feasible description of the nitrogen transport in terms of physics is fulfilled. The results are not limited to the specific process or setup, but they can be compared or transferred to an arbitrary surface modification process the physical parameters of which are known.

In order to gain experimental data, ion beam analysis has been employed extensively. An experiment that combines ion nitriding with the ion beam analytic method elastic recoil detection analysis deserves particular emphasize. This combined experiment allows for simultaneous, time resolved measurements of absolute concentration depth profiles of nitrogen and oxygen during ion nitriding.

Furthermore, transport models that allow for quantitative predictions have been resumed and refined. Modeling results have been compared to experimental data in order to check the applicability of the models and in order to characterize relevant transport mechanisms.

The issues that are directly addressed include:

**The structural nature of the nitrogen enriched layer** produced during successful ion nitriding of austenitic stainless steel is investigated by means of glancing angle x-ray diffraction spectroscopy. The diffraction data are consistent with a single phase layer with nitrogen in interstitial solid solution. As it is expected on the basis of Hägg's rule and Vegard's law, an expansion of the host lattice volume is observed, that is in first order linear with the ratio of nitrogen to host atoms. Comparison with lattice expansions and structural data measured elsewhere suggests that the lattice expansion is not only affected by the nitrogen content, but also by the thickness of the altered layer.

**The diffusion mechanism of nitrogen** is investigated by means of nuclear reaction analysis and slow positron implantation spectroscopy. A defect-mediated diffusion mechanism can not be substantiated. A qualitative trapping mechanism, that has been proposed elsewhere, can not be supported as well. However, depth profiles of  $^{14}\text{N}$  and  $^{15}\text{N}$ , measured by means of nuclear reaction analysis on samples that were subsequently ion nitrided with the two nitrogen isotopes, exhibit intriguing similarities to what would be expected from trapping if the traps are shallow enough to allow for detrapping. Therefore, a model for the diffusion of nitrogen in austenitic stainless steel at temperatures around  $400^\circ\text{C}$  is presented and discussed. The model considers the diffusion of nitrogen under the influence of trapping and detrapping at trap sites formed by local chromium. This assumption is consistent with our interpretation of the structural nature of the nitrogen enriched layer and plausible both from a thermodynamical and from a phenomenological point of view. Nitrogen depth profiles calculated on the basis of the model, assuming a pre-exponential factor of  $10^{-3}\text{ cm}^2/\text{s}$ , a diffusion activation energy of 1.1 eV, and a detrapping activation energy of 1.45 eV, are in good agreement with the experimental  $^{14}\text{N}$  and  $^{15}\text{N}$  depth profiles.

**The role of potential incorporation and release mechanisms** is investigated by means of real-time elastic recoil detection analysis and nuclear reaction analysis. The experiments provide evidence that absorption and desorption do not significantly contribute to nitrogen incorporation and release, respectively. An approach to model the nitrogen retention during ion nitriding in terms of purely ballistic mechanisms is presented and compared to experimental data. Modeling results and experimental results show reasonable agreement indicating that nitrogen incorporation and release are dominated by ion implantation and sputtering, respectively. Moreover, the role of a nitrogen (super)saturation limit and a possible additional release mechanism related to it is discussed.

**The evolution of the thickness of the nitrogen enriched layer** is investigated by means of glow discharge optical emission spectroscopy. Nitrogen and chromium depth profiles measured on samples that have been ion nitrided at  $400^\circ\text{C}$  for different relatively long times are presented and discussed. The depth profiles reveal that a stationary nitrogen near surface concentration of about 30 at.% establishes. A definition of the layer thickness appropriate to trapping and detrapping is given and a modeling approach is applied to fit the evolution of the layer thickness. The fit results in a diffusion coefficient of nitrogen on diffusion sites of  $5.8 \times 10^{-12}\text{ cm}^2/\text{s}$  and a surface recession rate of  $1 \times 10^{-8}\text{ cm/s}$ . Both values are in reasonable agreement with nitrogen diffusion data used to model  $^{14}\text{N}$  and  $^{15}\text{N}$  depth profiles and a surface recession rate predicted by TRIDYN simulations, respectively.

**The role of the surface oxide layer** is investigated by means of real-time elastic recoil detection analysis. A modeling approach for the evolution of the thickness of the surface oxide layer is presented. The approach is based on the assumption that during ion nitriding the surface oxide layer thickness is completely controlled by the interplay of sputtering and oxidation and differentiates between oxide layer growth limited by diffusion and oxide layer growth limited by the rate of oxygen supply. In combination with basic considerations on the oxide growth and SRIM simulations this approach allows for predictions on how the processing parameters affect the thickness of the surface oxide layer. Data obtained from real-time ERDA during ion nitriding at different combinations of ion energy and oxygen

partial pressure, respectively at different oxygen partial pressure, sustain the applicability of the modeling approach. For example, a surface oxide layer with stationary non-zero thickness establishes if the expected initial oxide growth rate is larger than the expected oxide removal rate while the surface oxide layer is essentially removed in the opposed case. The data also provide strong evidence that the surface oxide layer acts as a barrier for diffusional nitrogen transport and that the oxygen partial pressure is a key parameter for successful nitriding. Additionally, the data suggest that a thin surface oxide layer may improve the ion nitriding kinetics. Such a feature is consistent with a surface oxide layer that acts as a barrier for diffusional nitrogen transport and with the picture and that only nitrogen which gets implanted behind the layer is retained in the sample. This picture is corroborated by comparing real-time ERDA data obtained at different ion energies and similar stationary oxide layer thicknesses with predictions of SRIM simulations.

What are the technological consequences of the investigations presented in this work? The most important findings related to this question are strong evidence that (i) the surface oxide layer acts as a barrier for diffusional nitrogen transport, (ii) incorporation and release of nitrogen are dominated by ion implantation and sputtering, respectively, and (iii) the evolution of both nitrogen enriched layer thicknesses and surface oxide layer thicknesses can be described by a relatively simple differential equation. Assuming that these findings also apply for plasma nitriding and remote plasma nitriding techniques, for which Ref. [185, 88] provide some evidence, it seems that features of ion-solid interaction deserve more attention in modeling the results of plasma diffusion treatments in general. With this assumption the technological key question [73]: Is there a clear advantage of a particular technique or set of processing conditions? can be answered quantitatively on the basis of the presented modeling approaches and qualitatively as follows. For an efficient nitriding of austenitic stainless steel the surface oxide layer has to be removed or the ion energy has to be sufficiently high to implant nitrogen behind the surface oxide layer. In plasma nitriding the ion energy will not be sufficient to implant large amount of nitrogen behind the surface oxide layer. Thus, good vacuum conditions, in particular low partial pressures of oxygen containing molecules, are essential for successful nitriding. If this pre-condition is complied, relatively thick nitrogen enriched layers may be produced, since the relatively low ion energies are linked to relatively low surface erosion rates. In plasma immersion ion implantation and other remote plasma nitriding techniques that use relatively high ion energies, large amounts of nitrogen can be implanted behind the surface oxide layer. Vacuum conditions do not have to be as good as during plasma nitriding. In fact, properly adjusted oxygen partial pressures may be introduced intentionally, since a surface oxide with a relatively small stationary thickness will improve the nitrogen retention rate.

## Appendix A

# Consequences of an oscillating ion energy

After finishing this work, the nitrogen ion beam extracted from the ion source has been analyzed using a commercial mass spectrometer<sup>1</sup>. As a result of these investigations, the assumptions made on the ion energy distribution  $f(E)$  and on the ratio of molecular to atomic nitrogen ions  $N_2^+ : N^+$  are questionable (refer to Section 3.2). Most likely, the ion energy distribution was not relatively sharp, but subject to a strong oscillation around  $E_{in}$ . This oscillation appears to be reasonably described by

$$E(t) = E_{in} + E_{in} \sin(2\pi\nu t), \quad (\text{A.1})$$

where  $E(t)$  denotes the time dependent ion energy and  $\nu$  the frequency of the oscillation (100 Hz). Additionally, it appears more reasonable to assume a ratio  $N_2^+ : N^+ = 80 : 20$  instead of  $50 : 50$ . In this Appendix, consequences of these findings are briefly discussed.

Solving Equation A.1 for time and deriving with respect to energy results in the ion energy distribution

$$f(E) = \left| \frac{E_{in}}{\sqrt{1 - \left(\frac{E(t) - E_{in}}{E_{in}}\right)^2}} \right|, \quad (\text{A.2})$$

which is shown for  $E_{in} = 1$  keV and  $E_{in} = 2$  keV in Figure A.1.

Now, let us recall how the ion energy distribution  $f(E)$  and the ratio  $N_2^+ : N^+$  have been used in this work. In general, they appear in the frame of modeling approaches. For example, they enter into equations that have been used to estimate the amount of retained nitrogen  $N_{ret}$  (refer to Section 4.3) or the oxide removal rate  $j_{OR}$  (refer to Section 4.5). In both cases, products of the flux of incoming energetic nitrogen atoms  $j_{in}$ , and the partial sputtering yield of nitrogen  $SY_N$ , respectively of oxygen  $SY_O$ , appear in the equations. As a consequence of the different ratio  $N_2^+ : N^+$ ,  $j_{in}$  increases by 20% from  $j_{in} = 1.5 \times \rho/e$  to  $j_{in} = 1.8 \times \rho/e$ , where  $\rho$  denotes the current density and  $e$  the elementary charge (refer to Section 3.2). On the other hand, the partial sputtering yields decrease. Both the higher amount of molecular ions and the symmetric energy distribution around

<sup>1</sup>These investigations have been performed by Dr. T. Chevolleau and Miss T. Telbizova.

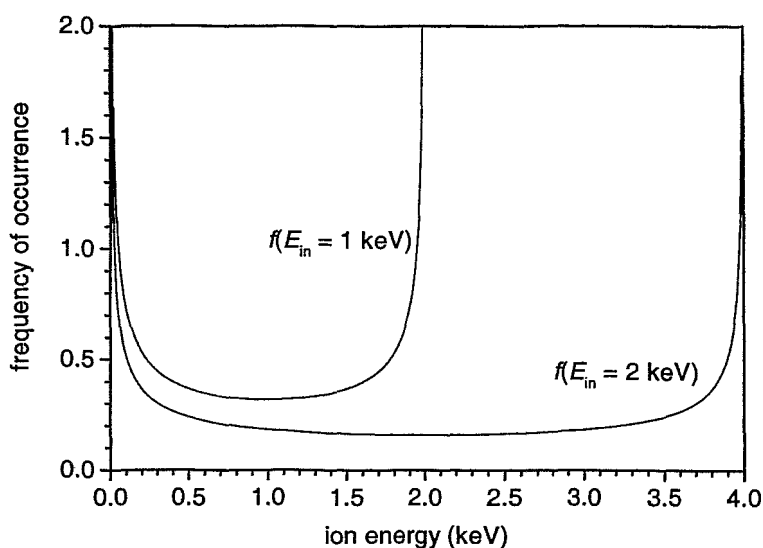


Figure A.1: Ion energy distributions according to Equation A.1 resulting for an ion energy oscillating around  $E_{in} = 1$  keV, respectively around  $E_{in} = 2$  keV.

$E_{in}$  contribute to this decrease<sup>2</sup>. Thus, the higher value of  $j_{in}$  will be partly compensated or even overcompensated by lower values of the partial sputtering yields.

For example, let us consider the expected oxide removal rate  $j_{OR}$ , which is given in Section 4.5 by Equation 4.16

$$j_{OR} = j_{in} \times \int f(E) SY_0(E) dE. \quad (A.3)$$

Figure A.2 shows the energy dependence of  $SY_0(E)$  as simulated by SRIM for  $N^+$  into  $Cr_2O_3$ . Additionally shown are the results for the integral  $\int f(E) SY_0(E) dE$ , once for  $N_2^+ : N^+ = 50 : 50$  and sharp energy distribution, and once for  $N_2^+ : N^+ = 80 : 20$  and energy distributions given by Equation A.2. The latter have been evaluated numerically<sup>3</sup>.

For example, at a kinetic energy  $E_{in} = 2$  keV, a current density  $\rho = 0.2$  mA/cm<sup>2</sup>, a ratio of molecular to atomic nitrogen ions  $N_2^+ : N^+ = 50 : 50$ , and sharp energy distribution around  $E_{in}$ , the expected oxide removal rate results as  $j_{OR} = 1.872 \times 10^{15} \times 0.51 = 9.55 \times 10^{14}$  O/cm<sup>2</sup>s, while at the same  $E_{in}$  and  $\rho$ , but  $N_2^+ : N^+ = 80 : 20$  and energy distributions given by Equation A.2 the expected oxide removal rate results as  $j_{OR} = 2.247 \times 10^{15} \times 0.415 = 9.32 \times 10^{14}$  O/cm<sup>2</sup>s.

In the energy range of interest the resulting deviations are smaller than 25%. Such changes do not substantially deteriorate the quality of the results, since the above formulas

<sup>2</sup>Recall that (i) the sputtering yield has been defined as a mean number per incident particle, (ii)  $N_2^+$  with a kinetic energy  $E_{in}$  can be considered as two  $N^+$ , each with a kinetic energy  $E_{in}/2$ , and (iii) in the energy range of interest the sputtering yield normally increases convex upwards with increasing ion energy.

<sup>3</sup>Many thanks to Mr. Ch. Klein for stimulating discussions and an introduction to the program MAPLE.



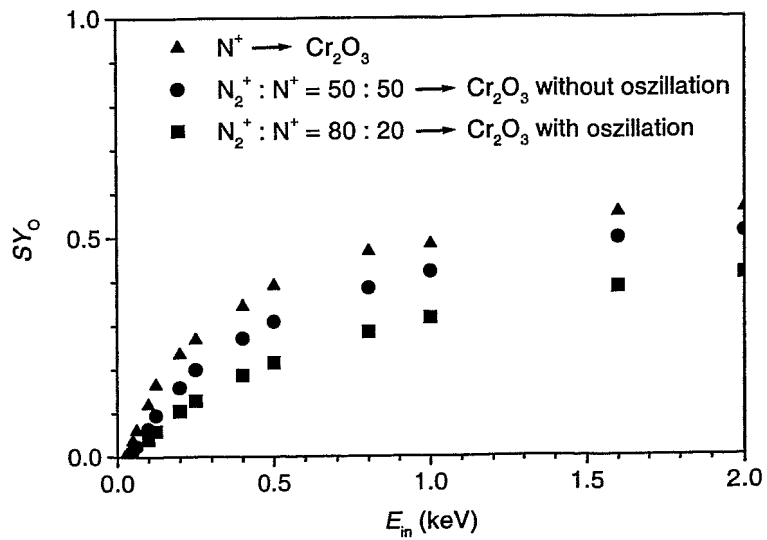


**Figure A.2:** Energy dependence of the partial sputtering yield of oxygen (i) as simulated for N<sup>+</sup> into Cr<sub>2</sub>O<sub>3</sub>, density 5.21 g/cm<sup>3</sup>, angle of incidence with respect to the surface normal 17.5°, E<sub>b</sub> = 3 eV, E<sub>s</sub> = 6.52 eV, and E<sub>d</sub> = 25 eV; (ii) for N<sub>2</sub><sup>+</sup> : N<sup>+</sup> = 50 : 50 and sharp energy distributions; (iii) for N<sub>2</sub><sup>+</sup> : N<sup>+</sup> = 80 : 20 and energy distributions given by Equation A.2.

– and the modeling approaches in general – are employed to *estimate* transport measures.

# List of Figures

2.1	Media and fields of physics involved in plasma nitriding . . . . .	6
2.2	Selected results of SRIM simulations . . . . .	9
2.3	Selected results of TRIDYN simulations . . . . .	11
2.4	A schematic example of depth profiles at constant surface concentration . .	13
2.5	A schematic diagram showing characteristic energy levels related to trapping	14
2.6	A schematic example for a depth profile under the influence of traps . . . .	15
2.7	A scheme showing mechanisms with potential relevance for incorporation and release of nitrogen . . . . .	17
2.8	Layer thickness versus time – a schematic example. . . . .	19
3.1	A sketch of the ion nitriding system . . . . .	23
3.2	A schematic view of the ion source . . . . .	24
3.3	A sketch visualizing the principle of ERDA . . . . .	28
3.4	A schematic view of the layout of the ionization chamber . . . . .	29
3.5	An example of an ERDA spectrum. . . . .	29
3.6	An example of oxygen and nitrogen depth profiles obtained from ERDA spectra . . . . .	30
3.7	A photograph and sketch of the experimental setup combining ERDA and low energy ion implantation . . . . .	32
3.8	Examples of time-resolved depth profiles obtained by real-time ERDA . . .	33
3.9	Examples of time-resolved areal densities and near surface concentrations obtained by real-time ERDA . . . . .	33
3.10	A sketch visualizing the principle of NRA . . . . .	34
3.11	An example of a NRA spectrum . . . . .	35
4.1	X-ray diffraction pattern of a virgin sample . . . . .	38
4.2	X-ray diffraction patterns and nitrogen depth profiles of samples ion nitrided at different temperatures . . . . .	40
4.3	X-ray diffraction patterns and nitrogen depth profiles of samples ion nitrided at different oxygen partial pressures . . . . .	41
4.4	The relative expansion of the mean volume per host atom vs. the ratio of nitrogen and host atoms . . . . .	43
4.5	Nitrogen depth profiles and the <i>S</i> -parameter versus the mean positron pen- etration depth of samples ion nitrided for different times . . . . .	48

4.6	The evolution of the thicknesses of the nitrogen enriched layer and the damaged layer. . . . .	49
4.7	$^{14}\text{N}$ and $^{15}\text{N}$ depth profiles after subsequent ion nitriding with $^{14}\text{N}$ and $^{15}\text{N}$	49
4.8	$^{14}\text{N}$ , $^{15}\text{N}$ , and total N depth profiles as measured and as simulated assuming trapping and detrapping . . . . .	51
4.9	Real-time ERDA data obtained during testing for absorption . . . . .	55
4.10	Real-time ERDA data obtained during testing for desorption . . . . .	56
4.11	Real-time ERDA data obtained at different current densities . . . . .	58
4.12	Evolution of the nitrogen near surface concentrations and the nitrogen areal densities at different current densities . . . . .	59
4.13	Nitrogen and chromium depth profiles after ion nitriding for different times	64
4.14	The evolution of the thickness of the nitrogen enriched layer . . . . .	65
4.15	Real-time ERDA data obtained at a low ion energy and a high oxygen partial pressure . . . . .	70
4.16	Real-time ERDA data obtained at a high ion energy and a high oxygen partial pressure . . . . .	71
4.17	Real-time ERDA data obtained at a high ion energy and a low oxygen partial pressure . . . . .	72
4.18	Real-time ERDA data obtained at different oxygen partial pressures; I . . .	73
4.19	Real time ERDA data obtained at different ion energies . . . . .	75
4.20	Real-time ERDA data obtained at different oxygen partial pressures; II . .	76
A.1	Oszillating ion energy – ion energy distributions . . . . .	86
A.2	Energy dependence of the partial sputtering yield of oxygen . . . . .	87

# List of Tables

3.1	Required and certified composition of AISI 316 . . . . .	21
3.2	Processing parameters of ion nitriding . . . . .	26
3.3	Standard experimental parameters of ERDA . . . . .	30
4.1	Peak positions and lattice constants for the virgin sample. . . . .	39
4.2	Peak positions and lattice constants for samples ion nitrided at different temperatures or different oxygen partial pressures. . . . .	42
4.3	Values related to the modeling approach for incorporation and release . . .	60
4.4	Estimated growth and removal rates for different combinations of ion energy and oxygen partial pressure . . . . .	69
4.5	Values related to modeling approach for the surface oxide layer . . . . .	77

# Bibliography

- [1] ASM Committee on Gas Carburizing, Carbonitriding and Nitriding, *Gas Nitriding, Heat treatment*, Vol. 4 of *ASM Handbook* (American Society for Metals, Materials Park, OH, 1991), p. 191–221.
- [2] Normenausschuss Werkstofftechnologie (NWT) - Wärmebehandlungstechnik - im DIN Deutsches Institut für Normung e.V., *Wärmebehandlung von Eisenwerkstoffen, Verfahren der Wärmebehandlung, Teil 4: Nitrieren und Nitrocarburieren*, Beuth, Berlin, Germany, 1998.
- [3] ASM Committee on Liquid Carburizing, *Liquid Nitriding, Heat treatment*, Vol. 4 of *ASM Handbook* (American Society for Metals, Materials Park, OH, 1991), p. 250–263.
- [4] Ruth Chatterjee-Fischer, *Wärmebehandlung von Eisenwerkstoffen: – Nitrieren und Nitrocarburieren*, 2. Ed. (expert, Renningen-Malmsheim, Germany, 1995).
- [5] *VDI-Lexikon Werkstofftechnik*, edited by H. Gräfen (VDI, Düsseldorf, Germany, 1993).
- [6] D. Lietdke and R. Jönsson, *Wärmebehandlung: Grundlagen für die Anwendungen für Eisenwerkstoffe* (expert, Renningen-Malmsheim, Germany, 1998).
- [7] B. Edenhofer, *Physical and Metallurgical Aspects of Ionitriding — Part 1*, Heat treatment of metals **1**, 23 (1974).
- [8] B. Edenhofer, *Physical and Metallurgical Aspects of Ionitriding — Part 2*, Heat treatment of metals **1**, 59 (1974).
- [9] A. Brokman and F.R. Tuler, *A study of the mechanisms of ion nitriding by the application of a magnetic field*, J. Appl. Phys. **52**, 468 (1981).
- [10] M. Hudis, *Study of ion-nitriding*, J. Appl. Phys. **44**, 1489 (1973).
- [11] in *Proceedings of the ASM's 2nd International Conference on Ion Nitriding/Carburizing*, edited by T. Spalvins and W.L. Kovacs (ASM International, Materials Park, OH, 1990).
- [12] G.G. Tibbetts, *Role of nitrogen atoms in "ion nitriding"*, J. Appl. Phys. **45**, 5072 (1974).

- [13] J.G. Parr and A. Hanson, *An introduction to stainless steel* (American Society for Metals, Metals Park, OH, 1965).
- [14] H. Schumann, *Metallographie* (VEB Deutscher Verlag für Grundstoffindustrie, Leipzig, Germany, 1975).
- [15] *Werkstoffkunde Stahl*, edited by Verein Deutscher Eisenhüttenleute (Springer, Berlin, Germany, 1984), Vol. 1.
- [16] *Stahlschlüssel-Taschenbuch*, Verlag Stahlschlüssel Wegst GmbH, Marbach, Germany, 1995.
- [17] AB Sandvik Steel, *Corrosion Handbook for stainless steels*, Sandviken, Schweden (1999).
- [18] A.H. Cottrell, *Theoretical structural metallurgy*, 2. Ed. (Edward Arnold Ltd., London, Great Britain, 1955).
- [19] N.E.W. Hartley, *Friction and wear of ion-implanted metals — A review*, Thin Solid Films **64**, 177 (1979).
- [20] *Ion implantation*, Vol. 10 of *Treatise on materials science and technology*, edited by J.K. Hirvonen (Academic Press Inc., New York, NY, 1980).
- [21] *Ion implantation 1988*, Vol. 57/58 of *Diffusion and defect data / A*, edited by F.H. Wöhlbier (Trans Tech Publ., Aedermannsdorf, Germany, 1988).
- [22] H. Dimigen, K. Kobs, R. Leutenecker, H. Ryssel and P. Eichinger, *Wear resistance of nitrogen-implanted steels*, Mat. Sci. Eng. **69**, 181 (1985).
- [23] D.L. Williamson, L. Wang, R. Wei and P.J. Wilbur, *Solid solution strengthening of stainless steel surface layers by rapid, high-dose, elevated temperature nitrogen ion implantation*, Mat. Let. **9**, 302 (1990).
- [24] G. Dearnaley, *Historical perspective of metal implantation*, Surf. Coat. Technol. **65**, 1 (1994).
- [25] A. Freißmuth, *Das Ausscheidungsverhalten stickstofflegierter austenitischer Chrom-Nickel-Stähle*, Berg- u. Hüttenm. Mh. **112**, 197 (1967).
- [26] in *High nitrogen steels*, edited by J. Foct and A. Hendry (Institute of Metals, London, Great Britain, 1989).
- [27] R.P. Reed, *Nitrogen in austenitic stainless steels*, J. Met. **45**, 16 (1989).
- [28] *Stickstofflegierte Stähle*, Vol. 4 of *Ergebnisse der Werkstoff - Forschung*, edited by M.O. Speidel and P.J. Uggowitzer (Thubal-Kain, Zürich, Switzerland, 1991).
- [29] V.G. Graviljuk and H. Berns, *High Nitrogen Steels* (Springer, Berlin, Germany, 1999).

- [30] in *High nitrogen steels '98: Proceedings of the 5th International Conference on High Nitrogen Steels*, Vol. 318 - 320 of *Materials Science Forum*, edited by H. Hänninen, S. Hertzman and J. Romu (Trans Tech Publications, Uetikon-Zürich, Switzerland, 1999).
- [31] Z.L. Zhang and T. Bell, *Structure and corrosion resistance of plasma nitrided stainless steel*, Surf. Eng. **1**, 131 (1985).
- [32] K. Ichii, K. Fujimura and T. Takase, *Structure of the ion-nitrided alayer of 18-8 stainless steel*, Technical Report No. 27, Kansai University, Osaka, Japan.
- [33] K. Ozbaysal and O.T. Inal, *Structure and properties of ion-nitrided stainless steel*, J. Mat. Sci. **21**, 4318 (1986).
- [34] M. Nunogaki, H. Suezawa, K. Hayasi and M. Miyazaki, *Plasma source nitriding*, Appl. Surf. Sci. **33/34**, 1135 (1988).
- [35] S.P. Hannula, P. Nenonen and J.P. Hirvonen, *Surface structure and properties of ion-nitrided austenitic stainless steels*, Thin Solid Films **181**, 343 (1989).
- [36] A. Szasz, D.J. Fabian, A. Hendry and Z. Szaszne-Csih, *Nitriding of stainless steel in an rf plasma*, J. Appl. Phys. **66**, 5598 (1989).
- [37] R. Wei, P.J. Wilbur, W.S. Sampath, D.L. Williamson, Y. Qu and L. Wang, *Tribological studies of ion-implanted steel constituents using an oscillating pin-on-disk wear tester*, J. Tribol. **112**, 27 (1990).
- [38] D.L. Williamson, O. Ozturk, S. Glick, R. Wei and P.J. Wilbur, *Microstructure of ultrahigh dose nitrogen-implanted iron and stainless steel*, Nucl. Instrum. Meth. B **59/60**, 737 (1991).
- [39] R. Wei, P.J. Wilbur, W.S. Sampath, D.L. Williamson and L. Wang, *Effects of ion implantation conditions on the tribology of ferrous surfaces*, J. Tribol. **113**, 166 (1991).
- [40] A. Saker, C. Leroy, H. Michel and C. Frantz, *Properties of sputtered stainless steel-nitrogen coatings and structural analogy with low temperature plasma nitrided layers of austenitic steel*, Mat. Sci. Eng. A **1991**, 702 (140).
- [41] M.E. Chabica, D.L. Williamson, R. Wei and P.J. Wilbur, *Microstructure and corrosion of nitrogen implanted AISI 304 stainless steel*, Surf. Coat. Technol. **51**, 24 (1992).
- [42] G.A. Collins, R. Hutchings and J. Tendys, *Plasma immersion ion implantation - the role of diffusion*, Surf. Coat. Technol. **59**, 267 (1993).
- [43] D.L. Williamson, *Microstructure and tribology of carbon, nitrogen, and oxygen implanted ferrous materials*, Nucl. Instrum. Meth. B **76**, 262 (1993).

- [44] M. Samandi, B.A. Shedden, D.I. Smith, G.A. Collins, R. Hutchings and J. Tendys, *Microstructure, corrosion and tribological behaviour of plasma immersion ion-implanted austenitic stainless steel*, Surf. Coat. Technol. **59**, 261 (1993).
- [45] A. Matthews and A. Leyland, in *Proceedings of the 2nd ASM Conference on Heat Treatment and Surface Engineering in Europe*, Vol. 163-165 of *Materials Science Forum*, edited by E.J. Mittemeijer (Trans Tech Publications, Uetikon-Zürich, Switzerland, 1994), p. 497 - 508.
- [46] O. Öztürk, *Surface modification of austenitic stainless steels by high-flux, elevated-temperature nitrogen-ion implantation*, Ph.D. thesis, Colorado School of Mines, 1994.
- [47] R. Wei, B. Shogrin, P.J. Wilbur, O. Ozturk, D.L. Williamson, I. Ivanov and E. Metin, *The effects of low-energy-nitrogen-ion implantation on the tribological and microstructural characteristics of AISI 304 stainless steel*, J. Tribol. **116**, 870 (1994).
- [48] M.K. Lei and Z.L. Zhang, *Plasma source ion nitriding : A new low temperature, low-pressure nitriding approach*, J. Vac. Sci. Technol. A **13**, 2986 (1995).
- [49] K.T. Rie and E. Broszeit, *PLasma diffusion treatment and duplex treatment - recent development and new applications*, Surf. Coat. Technol. **76-77**, 425 (1995).
- [50] E. Menthe, K.T. Rie, J.W. Schultze and S. Simson, *Structure and properties of plasma-nitrided stainless steel*, Surf. Coat. Technol. **74 - 75**, 412 (1995).
- [51] K.T. Rie, E. Menthe, A. Matthews, K. Legg and J. Chin, *Plasma surface engineering of metals*, MRS Bulletin **21**, 46 (1996).
- [52] S.J. Bull, A.M. Jones and A.R. McCabe, *Improving the mechanical properties of steel using low energy, high temperature nitrogen ion implantation*, Surf. Coat. Technol. **83**, 257 (1996).
- [53] A.M. Jones and S.J. Bull, *Changing the tribological performance of steel using low energy, high temperature nitrogen ion implantation*, Surf. Coat. Technol. **83**, 269 (1996).
- [54] P.J. Wilbur and B. W. Buchholtz, *Engineering tribological surfaces by ion implantation*, Surf. Coat. Technol. **79**, 1 (1996).
- [55] C. Blawert, A. Weisheit, B.L. Mordike and F.M. Knoop, *Plasma immersion ion implantation of stainless steel: austenitic stainless steel in comparison to austenitic-ferritic stainless steel*, Surf. Coat. Technol. **85**, 15 (1996).
- [56] R. Wei, *Low energy, high current density ion implantation of materials at elevated temperatures for tribological applications*, Surf. Coat. Technol. **83**, 218 (1996).
- [57] R. Wei, J.J. Vajo, J.N. Matossian, P.J. Wilbur, J.A. Davis, D.L. Williamson and G.A. Collins, *A comparative study of beam ion implantation, plasma ion implantation and nitriding of AISI 304 stainless steel*, Surf. Coat. Technol. **83**, 235 (1996).



- [58] R. Hutchings, K.T. Short and J. Tendys, *Investigation of plasma immersion ion implanted surfaces by instrumented indentation*, Surf. Coat. Technol. **83**, 243 (1996).
- [59] D.J. Rej, N.V. Gavrilov, D. Emlin, I. Henins, K. Kern, T. Kurennykh, V.N. Mizgulin, C.P. Munson, M. Nastasi, J.T. Scheuer, V. Vykhodets and K.C. Walters, *Carbon, Nitrogen, and Oxygen ion implantation of stainless steel*, Mat. Res. Soc. Symp. Proc. **396**, 661 (1996).
- [60] R. Günzel, J. Brutscher, S. Mändl and W. Möller, *Utilization of plasma source ion implantation for tribological applications*, Surf. Coat. Technol. **96**, 16 (1997).
- [61] S. Mändl, R. Günzel, E. Richter and W. Möller, *Nitriding of austenitic stainless steels using plasma immersion ion implantation*, Surf. Coat. Technol. **100 - 101**, 372 (1998).
- [62] D.L. Williamson, J.A. Davis, P.J. Wilbur, J.J. Vajo, R. Wei and J.N. Matossian, *Relative roles of ion energy, ion flux, and sample temperature in low-energy nitrogen ion implantation of Fe-Cr-Ni stainless steel*, Nucl. Instrum. Meth. B **127/128**, 930 (1997).
- [63] S. Schell, *Ionenstrahl nitrierung von austenitischen Edeltählen bei erhöhter Temperatur zur Verbesserung der tribologischen Eigenschaften bei gleichzeitig hoher Korrosionsbeständigkeit im Vergleich mit der Plasmanitrierung von austenitischen Edeltählen und deren Tribologischen- und Korrosionseigenschaften*, Ph.D. thesis, Ruprecht-Karls-Universität Heidelberg, 1998.
- [64] E. Camps, S. Muhl and S. Romero, *Influence of microwave plasma parameters on the nitriding of T-304 stainless steel*, Vacuum **51**, 385 (1998).
- [65] W. Möller, S. Parascandola, O. Kruse, R. Günzel and E. Richter, *Plasma-immersion ion implantation for diffusive treatment*, Surf. Coat. Technol. **116-119**, 1 (1999).
- [66] T. Bell, X.Y. Li and Y. Sun, in *Proceedings of the Asian Conference on Heat Treatment of Materials* (Institute of Metals, London, Great Britain, 1998), p. 1-11.
- [67] E. Menthe and K.T. Rie, *Further investigation of the structure and properties of austenitic stainless steel after plasma nitriding*, Surf. Coat. Technol. **116 - 119**, 199 (1999).
- [68] E. Menthe, *Bildung, Struktur und Eigenschaften der Randschicht von austenitischen Staehlen nach dem Plasmanitrieren*, Ph.D. thesis, Technische Universität Carolo-Wilhelmina, Braunschweig, Germany, 1999.
- [69] B. Larisch, U. Brusky and H.J. Spies, *Plasma nitriding of stainless steel at low temperatures*, Surf. Coat. Technol. **116 - 119**, 205 (1999).

- [70] X.B. Tian, Z.M. Zeng, T. Zhang, B.Y. Tang and P.K. Chu, *Medium-temperature plasma immersion-ion implantation of austenitic stainless steel*, Thin Solid Films **366**, 150 (2000).
- [71] E. Richter, R. Günzel, S. Parascandola, T. Telbizova, O. Kruse and W. Möller, *Nitriding of stainless steel and aluminium alloys by plasma immersion ion implantation*, Surf. Coat. Technol. **128 - 129**, 21 (2000).
- [72] W. Liang, X. Bin, Y. Zhiwei and S. Yaqin, *The wear and corrosion properties of stainless steel nitrided by low-pressure plasma-arc source ion nitriding at low temperatures*, Surf. Coat. Technol. **130**, 304 (2000).
- [73] D.L. Williamson, O. Öztürk, R. Wei and P.J. Wilbur, *Metastable phase formation and enhanced diffusion in f.c.c. alloys under high-dose high-flux nitrogen implantation at high and low ion energies*, Surf. Coat. Technol. **65**, 15 (1994).
- [74] Heat Treating Society ASM International, *ASM Heat Treating Society's 1999 Research & Development Plan*, 1999.
- [75] O. Öztürk and D.L. Williamson, *Phase and composition depth distribution analyses of low energy, high flux N implanted stainless steel*, J. Appl. Phys. **77**, 3839 (1995).
- [76] B.J. Lightfoot and D.H. Jack, in *Proceedings of the International Congress on Heat Treatment of Materials 1973* (The Metals Society, London, Great Britain, 1975), p. 59 - 66.
- [77] H.J. Grabke, *The kinetics of nitriding iron as a function of the oxygen activity of the gas*, Arch. Eisenhüttenwesen **44**, 603 (1973).
- [78] E. Fromm and G. Hörz, *Hydrogen, nitrogen, oxygen and carbon in metals*, International Metals Review **5/6**, 269 (1980).
- [79] D. Kumar, A.D. King and T. Bell, *Mass transfer of nitrogen from N<sub>2</sub> - H<sub>2</sub> atmospheres into Fe-18Cr-Ni-Mn alloys*, Metall Science **17**, 32 (1983).
- [80] H.J. Engell and H.J. Grabke, *Chemische Eigenschaften*, in *Werkstoffkunde Stahl*, edited by Verein Deutscher Eisenhüttenleute (Springer, Berlin, Germany, 1984), Vol. 1, p. 434 - 482.
- [81] H.J. Spies and S. Böhmer, *Beitrag zum kontrollierten Gasnitrieren von Eisenwerkstoffen*, Härterei Technische Mitteilungen **39**, 1 (1984).
- [82] H.A. Wriedt, N.A. Gokcen and R.H. Nafziger, *The Fe-N (Iron-Nitrogen) System*, Bulletin of Alloy Phase Diagrams **8**, 355 (1987).
- [83] M. Somers, *Internal and external nitriding and nitrocarburizing of iron and iron-based alloys*, Ph.D. thesis, Technische Universiteit Delft, Delft, The Netherlands, 1989.

- [84] A. Leyland, K.S. Fancey, A. S. James and A. Matthews, *Enhanced plasma nitriding at low pressures: a comparative study of d.c. and r.f. techniques*, Surf. Coat. Technol. **41**, 295 (1990).
- [85] D.A. Porter and K.E. Easterling, *Phase Transformations in Metals and Alloys*, 2 Ed. (Chapman & Hall, London, Great Britain, 1992).
- [86] H.J. Grabke, in *Proc. 150th Anniversary Symp. Surface Layers TU Delft*, Vol. 154 of *Material Science Forums* (Trans Tech Publications, Zürich, Switzerland, 1994), p. 69 - 86.
- [87] in *ASM Heat treatment and surface engineering conference II*, Vol. 163 - 165 of *Materials Science Forum*, edited by E.J. Mittemeijer (Trans Tech Publ., Uetikon-Zürich, Switzerland, 1994).
- [88] T. Czerwiec, H. Michel and E. Bergmann, *Low-pressure, high-density plasma nitriding: mechanisms, technology and results*, Surf. Coat. Technol. **108 - 109**, 182 (1998).
- [89] D.K. Inia, A.M. Vredenberg, F.H.P.M. Habraken and D.O. Boerma, *Nitrogen uptake and rate-limiting step in low-temperature nitriding of iron*, J. Appl. Phys. **86**, 810 (1999).
- [90] *Sputtering by Particle Bombardment I-III*, edited by R. Behrisch (Springer, Berlin, Germany, 1981 - 1991).
- [91] J.F. Ziegler, J.P. Biersack and U. Littmark, *The Stopping and Range of Ions in Matter* (Pergamon Press, New York, NY, 1985).
- [92] J. Lindhard, M. Scharff and H.E. Schiøtt, *Range concepts and heavy ion ranges*, Mat. Fys. Medd. Dan. Vid. Selsk. **33**, 1 (1963).
- [93] J.P. Biersack and D. Fink, *Implantation of boron and lithium in semiconductors and metals*, in *Ion implantation in semiconductors*, edited by S. Namba (Plenum Press, New York, NY, 1975), p. 211-218.
- [94] F. Bloch, *Zur Bremsung rasch bewegter Teilchen beim Durchgang durch Materie*, Annalen der Physik **16**, 285 (1933).
- [95] P. Sigmund, *Theory of Sputtering. I. Sputtering Yield of Amorphous and Polycrystalline Targets*, Phys. Rev. **184**, 383 (1969).
- [96] J. Bohdansky, *A universal relation for the sputtering yield of monoatomic solids at normal ion incidence*, Nucl. Instrum. Meth. B **2**, 587 (1984).
- [97] H.E. Schiøtt, *Range-energy relations for low-energy ions*, Mat. Fys. Medd. Dan. Vid. Selsk. **35**, 1 (1966).

- [98] G.H. Kinchin and R.S. Pease, *The displacement of atoms in solids by radiation*, Rep. Progr. Phys. **18**, 1 (1955).
- [99] J.F. Ziegler, *SRIM, The Stopping and Range of Ions in Matter*, Yorktown, NY, the program TRIM is continuously being updated with the respective newest version downloadable from <http://www.research.ibm.com/ionbeams/home.htm#SRIM>.
- [100] S.N. Bunker and A.J. Armani, *Modeling of concentration profiles from very high dose ion implantation*, Nucl. Instrum. Meth. B **39**, 7 (1989).
- [101] O.P.J. Vancauwenberghe, *On the growth of semiconductor-based epitaxial and oxide films from low-energy ion beams*, Ph.D. thesis, Massachusetts Institute of Technology, Cambridge, MASS, 1992.
- [102] N. Herbots, O.C. Hellman and O. Vancauwenberghe, in *Phase Formation and Modification by Beam-Solid Interactions*, Vol. 235 of *Mat. Res. Soc. Symp. Proc.*, edited by G.S. Was, L.E. Rehn and D. Follstaedt (Materials Research Society, Pittsburgh, PA, 1992), p. 769.
- [103] W. Möller and W. Eckstein, *TRIDYN - a TRIM simulation code including dynamic composition changes*, Nucl. Instrum. Meth. B **2**, 814 (1984).
- [104] W. Möller and W. Eckstein, *TRIDYN - Binary Collision Simulation of Atomic Collisions Dynamic Composition Changes in Solids*, Technical Report No. IPP 9/64, Max-Planck-Institut für Plasmaphysik, Garching, Germany.
- [105] V. Kharlamov, T. Schwieger, M. Posselt and W. Möller, *TRIDYN 4.0, Modifications for PC implementation, input dialog, and user manual*.
- [106] H.H. Andersen, *Abstract: Sputtering of multicomponent metal and semiconductor targets*, J. Vac. Sci. Technol. **16**, 770 (1979).
- [107] C.P. Flynn, *Point defects and diffusion* (Clarendon Press, Oxford, Great Britain, 1972).
- [108] J. Philibert, *Atom movements — Diffusion and mass transport in solids* (Les Editions de Physique, Les Ulis, France, 1991).
- [109] S.M. Myers, P.M. Richards, W.R. Wampler and F. Besenbacher, *Ion-beam studies of hydrogen-metal interactions*, J. Nucl. Mater. **165**, 9 (1989).
- [110] F.S. Ham, *Theory of diffusion-limited precipitation*, J. Phys. Chem. Solids **6**, 335 (1958).
- [111] W.B. Jackson and C.C. Tsai, *Hydrogen transport in amorphous silicon*, Phys. Rev. B **45**, 6564 (1992).
- [112] P. Shewmon, *Diffusion in Solids* (The Minerals, Metals & Materials Society, Warrendale, PA, 1989).

- [113] W. Möller and J. Roth, *Implantation, retention and release of hydrogen isotopes in solids*, in *Physics of plasma-wall interactions in controlled fusion*, edited by D.E. Post and R. Behrisch (Plenum Publishing Corporation, New York, NY, 1986).
- [114] J. Crank, *The Mathematics of Diffusion* (Clarendon Press, Oxford, Great Britain, 1985).
- [115] W. Möller, *PIDAT - A computer program for implantation, diffusion and trapping*, Technical Report No. IPP 9/44, Max-Planck-Institut für Plasmaphysik, Garching, Germany.
- [116] A.C. Hindmarsh, Technical Report No. UCID-30001, Lawrence Livermore Laboratory, Livermore, CA.
- [117] A.C. Hindmarsh, Technical Report No. UCID-30059, Lawrence Livermore Laboratory, Livermore, CA.
- [118] C. Wagner, *Beitrag zur Theorie des Anlaufvorganges*, Z. physikal. Ch. B **21**, 25 (1933).
- [119] V.I. Dimitrov, G. Knuyt, L.M. Stals, J.D'Haen and C. Quaeysaegens, *Generalized Wagner's diffusion model of surface modification of materials by plasma diffusion treatment*, Appl. Phys. A **67**, 183 (1998).
- [120] V.I. Dimitrov, J.D'Haen, G. Knuyt, C. Quaeysaegens and L.M. Stals, *A diffusion model of metal surface modification during plasma nitriding*, Appl. Phys. A **63**, 475 (1996).
- [121] V.I. Dimitrov, J.D'Haen, G. Knuyt, C. Quaeysaegens and L.M. Stals, *A simple diffusion model of surface modification by plasma*, Phys. Stat. Sol. **159**, 405 (1997).
- [122] V.I. Dimitrov, J.D'Haen, G. Knuyt, C. Quaeysaegens and L.M. Stals, *A method for determination of the effective diffusion coefficient and sputtering rate during plasma diffusion treatment*, Surf. Coat. Technol. **99**, 234 (1998).
- [123] American Society for Testing and Materials, *ASTM standards on iron-chromium, iron-chromium-nickel and related alloys*, 1965.
- [124] R. Leuteneker, G. Wagner, T. Louis, U. Gonser, L. Guzman and A. Molinari, *Phase transformation of a nitrogen-implanted austenitic stainless steel (X10CrNiTi18-9)*, Mat. Sci. Eng. A **115**, 229 (1989).
- [125] W. Anwand, S. Parascandola, E. Richter, G. Brauer, P.G. Coleman and W. Müller, *Slow positron implantation spectroscopy of high current ion nitrided austenitic stainless steel*, Nucl. Instrum. Meth. B **136 - 138**, 768 (1998).
- [126] M. Zeuner, J. Meichsner, H. Neumann, F. Scholze and F. Bigl, *Design of ion energy distributions by a broad beam ion source*, J. Appl. Phys. **80**, 611 (1996).

- [127] *Vacuum Vademecum*, Leybold AG, Köln, Germany.
- [128] W.H. Bragg and R. Kleeman, *On the  $\alpha$  particles of radium, and their loss of range in passing through various atoms and molecules*, Philos. Mag. **10**, 318 (1905).
- [129] E. Rutherford, *The scattering of  $\alpha$  and  $\beta$  particles by matter and the structure of the atom*, Philos. Mag. **21**, 669 (1911).
- [130] *Handbook of Modern Ion Beam Material Analysis*, edited by J.R. Tesmer and M. Nastasi (Materials Research Society, Pittsburgh, Pa, 1995).
- [131] W.-K. Chu, J.W. Mayer and M.-A. Nicolet, *Backscattering Spectroscopy* (Academic Press, New York, NY, 1978).
- [132] W. Assmann, H. Huber, C. Steinhausen, M. Dobler, H. Glückler and A. Weidinger, *Elastic recoil detection analysis with heavy ions*, Nucl. Instrum. Meth. B **89**, 131 (1994).
- [133] P. Staat, *Aufbau einer ortsempfindlichen Ionisationskammer für ERD-Messungen mit Schwerionen*, Master's thesis, Ludwig-Maximilians-Universität München, 1992.
- [134] J.C. Barbour and B.L. Doyle, *Elastic recoil detection: ERD*, in *Handbook of Modern Ion Beam Material Analysis*, edited by J.R. Tesmer and M. Nastasi (Materials Research Society, Pittsburgh, PA, 1995), Chap. 5.
- [135] C. Spaeth, F. Richter, S. Grigull and U. Kreissig, *Conversion algorithm for ERDA multielement spectra and its application to thin-film problems*, Nucl. Instrum. Meth. B **140**, 243 (1998).
- [136] N.P. Barradas, C. Jaynes, R.P. Webb, U. Kreissig and R. Grötzschel, *Unambiguous automatic evaluation of multiple Ion Beam Analysis data with Simulated Annealing*, Nucl. Instrum. Meth. B **149**, 233 (1999).
- [137] J.F. Ziegler, *STOP95, Ion Stopping Subroutine*.
- [138] C.C. Theron, J.C. Lombaard and R. Pretorius, *Real-time RBS of solid-state reaction in thin films*, Nucl. Instrum. Meth. B **161 - 163**, 48 (2000).
- [139] I.C. Vickridge, W.J. Trompeter, I.W.M. Brown and J.E. Patterson, *Nuclear reaction analysis of nitrided Ti and Ti<sub>6</sub>Al<sub>4</sub>V*, Nucl. Instrum. Meth. B **99**, 454 (1995).
- [140] K. Bethge, *Ion beam analysis of nitrogen*, Nucl. Instrum. Meth. B **66**, 146 (1992).
- [141] R.A. Jarjis, *Nuclear cross section data for surface analysis*, Technical report, University of Manchester.
- [142] V. Gomes Porto, N. Ueta, R.A. Douglas, O. Sala, D. Wilmore, B.A. Robson and P.E. Hoddgson, *Deuterium induced reactions on <sup>14</sup>N*, Nucl. Phys. A **136**, 385 (1969).

- [143] J.A. Sawicki, J.A. Davies and T.E. Jackman, *Absolute calibration of the  $^{15}\text{N}(d, \alpha_0)^{13}\text{C}$  and  $^{15}\text{N}(p, \alpha_0)^{12}\text{C}$  reaction cross sections*, Nucl. Instrum. Meth. B **15**, 530 (1986).
- [144] I.C. Vickridge, W.J. Trompeter and G.E. Coote,  *$^{15}\text{N}(d, \alpha_0)^{13}\text{C}$  cross section and angular distribution measurements for ion beam analysis*, Nucl. Instrum. Meth. B **108**, 367 (1996).
- [145] U. Kreissig, S. Grigull, K. Lange, P. Nitzsche and B. Schmidt, *In situ ERDA studies of ion drift processes during anodic bonding of alkali-borosilicate glass to metal*, Nucl. Instrum. Meth. B **136 - 138**, 674 (1998).
- [146] N.P. Barradas, S. Parascandola, B.J. Sealy, R. Grötzschel and U. Kreissig, *Simultaneous and consistent analysis of NRA, RBS, and ERDA data with the IBA Data-Furnace*, Nucl. Instrum. Meth. B **161 - 163**, 308 (2000).
- [147] M. Samandi, B.A. Shedden, T. Bell, G.A. Collins, R. Hutchings and J. Tendys, *Significance of nitrogen mass transfer mechanism on the nitriding behavior of austenitic stainless steel*, J. Vac. Sci. Technol. B **12**, 935 (1994).
- [148] D.L. Williamson, J.A. Davis and P.J. Wilbur, *Effect of austenitic stainless steel composition on low-energy, high-flux, nitrogen ion beam processing*, Surf. Coat. Technol. **103 - 104**, 178 (1998).
- [149] K. Marchev, M. Landis, R. Vallerio, C.V. Cooper and B.C. Giessen, *The m phase layer on ion nitrided austenitic stainless steel (III): an epitaxial relationship between the m phase and the  $\gamma$  parent phase and a review of structural investigations of this phase*, Surf. Coat. Technol. **116 - 119**, 184 (1999).
- [150] C. Blawert, B.L. Mordike, Y. Jiràsková and O. Schneeweiss, *Structure and composition of expanded austenite produced by nitrogen plasma immersion ion implantation of stainless steel X6CrNiTi1810 and X2CrNiMoN2253*, Surf. Coat. Technol. **116 - 119**, 189 (1999).
- [151] X.-Y. Li, Y. Sun and T. Bell, *The Stability of the Nitrogen S-Phase in Austenitic Stainless Steel*, Z. Metallkd. **90**, 901 (1999).
- [152] Y. Sun, X.Y. Li and T. Bell, *X-ray diffraction characterization of low temperature plasma nitrided austenitic stainless steels*, J. Mater. Sci. **34**, 4793 (1999).
- [153] X.L. Xu, L. Wang, Z.W. Yu and Z.K. Hei, *Microstructural characterization of plasma nitrided austenitic stainless steel*, Surf. Coat. Technol. **132**, 270 (2000).
- [154] S. Mändl and B. Rauschenbach, *Anisotropic strain in nitrided austenitic stainless steels*, J. Appl. Phys. **88**, 3323 (2000).
- [155] J.C. Jiang and E.I. Melitis, *Microstructure of the nitride layer of AISI 316 stainless steel produced by intensified plasma assisted processing*, J. Appl. Phys. **88**, 4026 (2000).

- [156] S. Grigull and S. Parascandola, *Ion-nitriding induced plastic deformation in austenitic stainless steel*, 2000.
- [157] T. Heumann, *Diffusion in Metallen* (Springer, Berlin, 1992).
- [158] L. Cheng, A. Böttger, Th.H. de Keijser and E.J. Mittemeijer, *Lattice parameters of iron-carbon and iron-nitrogen martensites and austenites*, Scr. Metall. **24**, 509 (1990).
- [159] A. Köhl and D. Bergner, *Chemische Diffusion von Stickstoff in hochlegierten austenitischen CrNi(Mo)-Stählen*, Mat.-wiss. u. Werkstofftech. **22**, 462 (1991).
- [160] M. Kikuchi, T. Tanaka, K. Hamagami, Y. Ogura and R. Tanaka, *Lattice Dilation of 25Cr-28Ni and 25Cr-28Ni-2Mo Austenitic Steels by Dissolved Nitrogen*, Met. Trans. A **7A**, 906 (1976).
- [161] K. Marchev, C.V. Cooper, J.T. Blucher and B.C. Giessen, *Conditions for the formation of a martensitic single-phase compound layer in ion-nitrided 316L austenitic stainless steel*, Surf. Coat. Technol. **99**, 225 (1998).
- [162] K. Marchev, R. Hidalgo, M. Landis, R. Vallerio, C.V. Cooper and B.C. Giessen, *The metastable m phase layer on ion nitrided austenitic stainless steel Part 2: crystal structure and observation of its two-directional orientational anisotropy*, Surf. Coat. Technol. **112**, 67 (1999).
- [163] H.P. Klug and L.E. Alexander, *X-ray diffraction procedures for polycrystalline and amorphous materials* (Wiley, New York, 1984).
- [164] G.A. Collins, R. Hutchings, K.T. Short, J. Tendys, X. Li and M. Samandi, *Nitriding of austenitic stainless steel by plasma immersion ion implantation*, Surf. Coat. Technol. **74 - 75**, 417 (1995).
- [165] N. Renevier, P. Collignon, H. Michel and T. Czerwicz, *Low temperature nitriding of AISI 316L stainless steel and titanium in a low pressure arc discharge*, Surf. Coat. Technol. **111**, 128 (1999).
- [166] J. Kučera and K. Stránský, *Diffusion, in iron, iron solid solutions and steels*, Mater. Sci. Eng. **52**, 1 (1982).
- [167] G. Hägg, *Gesetzmässigkeiten im Kristallbau bei Hybriden, Boriden, Carbiden und Nitriden der Übergangselemente*, Z. Phys. Chem. B **9**, 33 (1931).
- [168] J.L. Whitton, M.M. Ferguson, G.T. Ewan, I.V. Mitchell and H.H. Plattner, *Rutherford backscattering, nuclear reaction, and channeling studies of nitrogen implanted single-crystal stainless steel*, Appl. Phys. Lett **41**, 150 (1982).
- [169] K. Oda, K. Umezu and H. Ino, *Interaction and arrangement of nitrogen atoms in FCC  $\gamma$ -iron*, J. Phys.: Condens. Matter **2**, 10147 (1990).



- [170] X. Zheng, *Nitrogen solubility in iron-base alloys and powder metallurgy of high nitrogen stainless steels*, Ph.D. thesis, Eidgenössische Technische Hochschule Zürich, Schweiz, 1991.
- [171] J. Tervo, A. Tarasenko and H. Hänninen, in *High Nitrogen Steels, Proceedings of the 5th International Conference on High Nitrogen Steels*, Vol. 318-320 of *Materials Science Forum*, edited by H. Hänninen, S. Hertzman and J. Romu (Trans Tech Publications, Uetikon-Zürich, Switzerland, 1999), p. 41 - 46.
- [172] P. Kizler, G. Frommeyer and R. Rosenkranz, *Localization of nitrogen atoms in nitrogen alloyed austenitic and ferritic stainless steel by EXAFS studies*, *Z. Metallkd.* **85**, 705 (1994).
- [173] V.V. Sumin, G. Chimid, Ts. Rashev and L. Saryivanov, in *High Nitrogen Steels, Proceedings of the 5th International Conference on High Nitrogen Steels*, Vol. 318 - 320 of *Materials Science Forum*, edited by H. Hänninen, S. Hertzman and J. Romu (Trans Tech Publications, Uetikon-Zürich, Switzerland, 1999), p. 31 - 40.
- [174] H. Numakura, M. Miura, H. Matsumoto and M. Koiwa, *Nitrogen trapping to chromium in  $\alpha$  iron studied by internal friction and magnetic after-effect techniques*, *ISIJ international / Iron and Steel Institute of Japan* **36**, 290 (1996).
- [175] P. Müllner, C. Solenthaler, P. Uggowitzer and M.O. Speidel, *On the effect of nitrogen on the dislocation structure of austenitic stainless steel*, *Mat. Sci. Eng. A* **164**, 164 (1993).
- [176] P. Müllner, C. Solenthaler and M.O. Speidel, *Second order twinning in austenitic steel*, *Acta metall. mater.* **42**, 1727 (1994).
- [177] J. Hirvonen and A. Anttila, *Annealing behavior of implanted nitrogen in AISI 316 stainless steel*, *Appl. Phys. Lett.* **46**, 835 (1985).
- [178] A. Kühnl, D. Bergner, H.J. Ullrich, M. Schlaubitz and P. Karduck, *Investigations of nitrogen diffusion in austenitic CrNi Steels*, *Mikrochim. Acta* **107**, 295 (1992).
- [179] D.L. Williamson, I. Ivanov, R. Wei and P.J. Wilbur, *Role of chromium in high-dose, high-rate, elevated temperature nitrogen implantation of austenitic stainless steels*, *Mat. Res. Soc. Symp. Proc.* **235**, 473 (1992).
- [180] E.I. Melitis and S. Yan, *Low-pressure ion nitriding of AISI 304 austenitic stainless steel with an intensified glow discharge*, *J. of Vac. Sci. Technol. A* **11**, 25 (1993).
- [181] A. van Veen, H. Schut, J. de Vries, R.A. Hakvoort and M.R. Ijpma, in *Positron beams for solids and surfaces, AIP Conference Proceedings No. 218*, edited by P.J. Schultz, G.R. Massoumi and P.J. Simpson (American Institute of Physics, New York, NY, 1990), p. 171.

- [182] O. Öztürk and D.L. Williamson, *The annealing behavior of implanted nitrogen in fcc stainless steel*, Hyperfine Interactions **92**, 1329 (1994).
- [183] M.J. Baldwin, S. Kumar, J.M. Priest, M.P. Fewell, K.E. Prince and K.T. Short, *Plasma-nitrided AISI-316 stainless steel examined by scanning electron microscopy and secondary ion mass spectrometry*, Thin Solid Films **345**, 108 (1999).
- [184] M. Kemp and H.M. Branz, *Hydrogen diffusion in  $\alpha$ -Si:H: Solution on the tracer equation including capture by exchange*, Phys. Rev. B **52**, 13946 (1995).
- [185] M. Berg, C.V. Budtz-Jørgensen, H. Reitz, K.O. Schweitz, J. Chevallier, P. Kringhøj and J. Böttiger, *On plasma nitriding of steels*, Surf. Coat. Technol. **124**, 25 (2000).
- [186] J.M. Priest, M.J. Baldwin, M.P. Fewell, S.C. Haydon, G.A. Collins, K.T. Short and J. Tendys, *Low pressure r.f. nitriding of austenitic stainless steel in an industrial-style heat-treatment furnace*, Thin Solid Films **345**, 113 (1999).
- [187] T. Barnavon, J. Tousset, S. Fayeulle, P. Guiraldenq, D. Treheux and M. Robelet, *Distribution of nitrogen implanted in iron as a function of fluence*, Rad. Eff. **77**, 249 (1983).
- [188] T. Asam, *Glow discharge optical spectroscopy depth profile analysis of conductive and nonconductive samples in a commercial service laboratory*, Surf. Coat. Technol. **116** - **119**, 310 (1999).
- [189] S. Parascandola, O. Kruse and W. Möller, *The interplay of sputtering and oxidation during plasma diffusion treatment*, Appl. Phys. Lett **75**, 1851 (1999).
- [190] S. Parascandola, T. Telbizove, O. Kruse and W. Möller, *The influence of the oxygen partial pressure on the ion nitriding of aluminium - An investigation by means of real time elastic recoil detection analysis*, Nucl. Instrum. Meth. B **161** - **163**, 406 (2000).
- [191] I. Olefjord, *ESCA studies on films formed on stainless steels during oxidation and during electropolishing*, Scand. J. Metall. **3**, 129 (1974).
- [192] A. Atkinson, *Transport processes during the growth of oxide films at elevated temperatures*, Review of Modern Physics **57**, 437 (1985).
- [193] D. Kim, *A study of the effect on nitrogen and molybdenum in the corrosion inhibition of austenitic stainless steel*, Ph.D. thesis, State University of New York at Stony Brook, 1992.
- [194] C.R. Clayton and I. Olefjord, *Passivity of austenitic stainless steels*, in *Corrosion mechanisms in theory and practice*, edited by P. Marcus and J. Oudar (Dekker, New York, NY, 1995), p. 175 - 198.
- [195] S. Shibagaki, A. Koga, Y. Shirakawa, H. Onishi, H. Yokokawa and J. Tanaka, *Chemical reaction path for thin film oxidation of stainless steel*, Thin Solid Films **303**, 101 (1997).

[196] *CRC Handbook of Chemistry and Physics*, edited by D.R. Lide (CRC Press, Florida, USA, 1994).

# Acknowledgements / Danksagung

Dank sagen möchte ich:

- **Prof. Dr. W. Möller** für die optimale Begleitung, die er meiner Arbeit als Doktorvater entgegen gebracht hat, sowie für seine Ermunterung und Unterstützung in Sachen Auslandsaufenthalte und Konferenzbesuche.
- **Prof. Dr. D. L. Williamson** für seine Arbeiten und Anregungen zum Thema, die sowohl initialisierend als auch lenkend auf die vorliegende Arbeit gewirkt haben, für die freundliche Aufnahme während zweier Aufenthalte an der Colorado School of Mines, für sein Interesse an offenen detaillierten Diskussionen auch in strittigen Fragen, sowie für die Übernahme des zweiten Gutachtens.
- **Prof. Dr. G. K. Wolf** für die freundliche Übernahme des dritten Gutachtens.
- **Dr. O. Kruse** für seine Arbeit zur real-time ERDA, die die Aufnahme von zeitaufgelösten Tiefenprofilen mit ermöglicht hat.
- **allen Mitarbeitern des Institutes** für die freundliche Aufnahme sowie ihre mittelbare und des öfteren auch unmittelbare Unterstützung, insbesondere den Mitarbeitern der Abteilung Ionenimplantation um **Dr. E. Richter**, der Abteilung Ionenstrahlanalytik um **Dr. R. Grötzschel** sowie der Abteilung Beschleuniger um **Dr. M. Friedrich**.
- **meinen Mitstreitern und Leidensgenossen** in der Doktorandenschaft, insbesondere **Dr. Stephan Hausmann, Dr. Mathias Strobel, Christoph Klein** sowie **Irina Mrotschek**.
- **meinem Freund und Studienkollegen Edo von Glan**.
- **meinen Eltern**  
und
- **zum Schluss aber nicht zuletzt meiner Frau Birte**.